Spectroscopic investigation of zeolite supported PdAg and PtAg bimetallic clusters

Von der Fakultät Chemie der Universität Stuttgart zur Erlangung der Würde eines Doktors der Naturwissenschaften (Dr. rer. nat.)

genehmigte Abhandlung

vorgelegt von

Olga Lechner

geb. Terekhina

aus Tikhvin, Russland

- *Hauptberichter:* *Prof. Dr. E. Roduner*
- *Mitberichter:* *Apl. Prof. Dr. M. Hunger*
- *Tag der mündlichen Prüfung* *28.06.2012*

Institut für Physikalische Chemie

der Universität Stuttgart

Juni 2012

Eidesstattliche Erklärung

Ich versichere, dass ich diese Dissertation selbständig verfasst und nur die angegebenen Quellen und Hilfsmittel verwendet habe.

Stuttgart, 07. Mai 2012

Olga Lechner

To my family

Acknowledgment

First of all I would like to thank my supervisor **Prof. Dr. Emil Roduner** for giving me an opportunity to work on my PhD thesis in his research group at the University of Stuttgart. It was a great time for me and I am deeply grateful for his thoughtful guidance, support not only in the scientific field, our fruitful discussions on different topics and his always helpful advices. I am very thankful for the possibility to learn a lot of new things on numerous seminars, workshops and conferences. I also owe him special thanks for the patient correction of my thesis.

I also would like to thank **Prof. Dr. Michael Hunger** for writing the second advisory opinion and **Prof. Dr. Joris van Slageren** for taking the chair in the examination board.

I thank **Dr. Herbert Dilger** for helping me with the software, hardware and practically with the every experimental problem.

Mrs. Gabriele Bräuning and **Ms. H. Fingerle** (from the Institute of Technical Chemistry) are acknowledged for their help with the AAS measurements; Mrs. Bräuning also for getting the chemical reactants and other laboratory items.

I sincerely thank the members of the mechanical, the electrical and the glass workshops for their help and support of my experimental work.

Dr. Sankaran Anantharaman is acknowledged for the EXAFS measurements and data evaluation.

My special thanks are for **Mrs. Inge Blankenship** for her secretarial assistance and support in formalities, especially during my first time in Germany. I also thank **Dr. Dieter Leicht** for his help in administrative procedures and the warm climate during the practice time.

I am grateful to all my group fellows for the excellent working atmosphere, in particular to **Göki Kuseci, Steffen Hink and Anette Häusser**.

Acknowledgment

I greatly thank my friend **Dr. Tanja Archipov** for our fruitful discussions, her help and support. I wish to thank **Alexander Kromer** for his friendship and for all our discussions concerning EPR over a lunch.

I like to thank all my friends in Russia and Germany for their all time support und understanding.

I could not thank enough my family, especially my dearest mom **Liudmila** and my sister **Elizaveta**, for their support and encouragement during all the time of my life. I would not be who I am today without them.

My very special thank goes to my beloved husband **Roman**, who was always there for me.

Stuttgart, 07. Mai 2012 Olga Lechner

Contents

Abbreviation List

4R	four-membered ring in a zeolite structure
6R	six-membered ring in a zeolite structure
12R	twelve-membered ring in a zeolite structure
AAS	Atomic Absorption Spectroscopy
BET	Stephen Brunauer, Paul Emmett and Edward Teller
CN	coordination number
CW	continuous wave
D6R	double-six rings (hexagonal prisms) in a zeolite structure
DTG	Differential Thermal Gravimetry
ENDOR	Electron Nuclear Double Resonance
EPR/ ESR	Electron Paramagnetic / Spin Resonance
ESEEM	Electron Spin Echo Envelope Modulation
EXAFS	Extended X-ray Absorption Fine Structure
FAU	faujasite structure of a zeolite
FTIR	Fourier Transform Infrared
HF	hyperfine
HK	Horvath and Kawazoe
HREM	High Resolution Electron Microscopy
ICP	Induced Coupled Plasma
IR	Infrared
IUPAC	International Union of Pure and Applied Chemistry
L/B	linear/ bridge
NMR	Nuclear Magnetic Resonance
PSD	pore-size distribution
rot	rotational
TMI	transition metal ions
u.c.	unit cell
vib	vibrational
vol.	volume
wt.	weight
XAS	X-ray Absorption Spectroscopy
XRD	X-Ray powder/single crystal Diffraction
Z	zeolite framework
ZI	Zeeman interaction

1 Introduction

1.1 Motivation

Highly dispersed, oxide- or zeolite-supported bimetallic catalysts are widely used in the catalytic industry, such as in petrochemistry, catalytic reforming, nitrogen industry and gas-to-liquid technology.[1] In particular, *platinum* heterogeneous catalysts have many applications, an important one is the enhancing the CO-tolerance of the electrocatalysts used in fuel cells. The poisoning effect of chemisorbed CO considerably deteriorates the catalytic performance of Pt surfaces in direct methanol oxidation fuel cells, as well as in fuel cells using H_2 obtained by reformation. Alloying Pt with other transition metals is one of the best-known remedies for this poisoning effect.[2]

Another direction in the "fuel chemistry" – the use of Pt catalysts for the hydrogenation of aromatics and hydrodesulfurization reactions. Such studies indicate that particular emissions in diesel exhaust gases can be reduced by decreasing the fuel's sulfur content. Highly active catalysts are, however, very susceptible to sulfur poisoning. One of the approaches to improve sulfur resistance of noble metal-based catalysts is to alloy the active component with another metal. The presence of the second metal atoms around Pt active sites may block sulfur adsorption on Pt. Bimetallic systems also enable the tailoring of catalytic activity and selectivity, which is referred to in the literature as occurring through a "cooperative effect".[3]

A further approach is to modify the metal atom's electronic properties by using acidic supports such as zeolites. In the case of Pt-based catalysts, the chemical interaction between the strong acid support and the Pt atoms induces an electron-deficient character at the metal. The partial positive charge on Pt decreases the bond strength between the electron acceptor (S) and the electron-deficient metal (Pt), which improves the sulfur resistance of the catalyst.[3]

Selective hydrogenation of acetylene to ethylene is also a very important industrial purification process for removing trace amounts of acetylene from ethylene. A supported *palladium* catalyst is the commercial catalyst for this purification process. It has, however, poor selectivity at high conversion. The addition of a second metal has been attracting considerable attention to enhance the selective hydrogenation of acetylene. *Silver* has been reported as a selectivity promoter for this reaction.[4]

Due to their unique properties, bimetallic nanoparticles received an enhanced attention in the last decade, both technologically and scientifically. The selectivity of catalytic reactions can

be controlled by changing the catalyst composition. The knowledge of structural and/or electronics effects of alloying is essential to catalyst optimization as both segregation and different adsorption properties may be explained by them.[5]

The concepts of "ensemble" (or geometric) and "ligand" (or electronic) effects of alloying are commonly used to rationalize this superior activity of bimetallic systems in electrochemistry and heterogeneous catalysis. The former concept refers to the fact, that the addition of a second metal may block certain sites, reducing or eliminating the formation of an inhibiting species or an important intermediate. Thus, specific grouping of surface atoms are required to serve as active sites. The latter effect refers to the formation of heteronuclear metal-metal bonds in binary alloys that involves a modification of the electronic structure, leading to the different (and, it is hoped, better) overall catalytic activity with respect to that of either of the constituent metals. Orbital rehybridization of one or both of the metals and/or charge transfer between the metals can substantially modify the catalytic performance by means of ligand effect.[6] It should also be mentioned, that two main groups of bimetallic colloids exist, alloyed and layered (core–shell) colloids.[7] The effects of alloying in both systems are different. These effects are also unpredictable, especially in nanoalloys. Physical and chemical properties of clusters are size-dependent and thus tunable.

Opposite to the bulk alloys, nanosized bimetallic catalysts are also extremely sensitive to the structure and morphology of the supporting material in which the nanoparticles are embedded.[1]

Earlier studies have mostly been done on inorganic oxide-supported bimetallic nanoparticles. Recently, novel techniques like microemulsion, decomposition of organometallic precursors, radiolysis, etc., have been developed for the synthesis of colloidal suspensions of these nanoparticle systems.[8] Low-silica zeolites, ion-exchanged with transition metals, are used as selective oxidation catalysts since the late 1960's.[9] The combination of the catalytic properties of transition metals with the steric constraints imposed by the zeolite structure carries great potential for active and selective catalysts.[10] Both the size and the size-distribution of particles are major parameters for supported metal catalysts. With the "ship-in-a-bottle" approach and using molecular sieve as a "template", the size of metal particles formed in the "template" can possibly be controlled, and a sharp distribution in a narrow size region can be achieved. And the structure of catalysts have a significant influence on their properties.[11]

Palladium and platinum nanoclusters were chosen as the objects under investigation due to their importance in the catalytic industry, mentioned above. Silver was chosen as an alloying metal due to its relatively low reactivity. The addition of Ag was found to improve the catalyst stability and modify the product selectivity.[12] Bimetallic colloids containing Ag also have not been extensively studied except for the Ag-Au system.[13]

Fourier transform infrared (FTIR) spectroscopy was used as easy and powerful technique which allows to confirm the formation of a bimetallic alloy,[14] and CO was chosen as a probe molecule since a large database exists in the literature regarding its adsorption on transition metal surfaces.

Electron paramagnetic resonance (EPR) spectroscopy is one of the important characterization techniques which allows indentifying the location and the specific oxidation states of transition metal ions in zeolites.

Inspite of the fact that bimetallic nanoalloys became a “hot topic” in the last years, not so many studies dedicated to PdAg and PtAg nanoclusters, in particular, supported on zeolites exist.

One of the popular research directions now relates to metal nanoparticles covered by organic materials, because they can be well dispersed in organic media.[14] Most of the reported literature on bimetallic nanoparticles concerns the stabilization of metallic particles in aqueous media in the presence of surfactants or water-soluble polymers as stabilizers. For the PdAg/ PtAg case there exist the reports dedicated to liquid crystal nanoparticles in form of gelling agents,[15] colloidal particles,[13,16,17] nanoparticles immobilized on imogolite fibers,[18] liquid crystal molecule-cappes nanoparticles,[14] water-in-oil microemulsions,[19] nanorods in a solution[8] and others. Such systems are of interest especially due to their unique electro-optic properties and are widely used in liquid crystal devices technology.[14]

The stabilization in a solid matrix avoids coagulation and precipitation of particles. Additionally, the bimetallic catalysts can be recovered easily after the reaction and hence elaborate separation procedures can be avoided.[20] There are several studies of PdAg/ PtAg nanoparticles supported on a solid, for example on alumina[21] or carbon.[22]

The most popular support for Pt and Pd catalysts are, however, the zeolites. Pd and Pt supported faujasites are important catalysts in petroleum and petrochemical industries due to their higher catalytic activity towards hydrogenation and hydrogenolysis, a stronger resistance to sulfur poisoning and enhanced stability towards sintering.[23]

In particular, PdAg/ PtAg systems, embebbed in zeolites, were studied only by a few researchers, for example by Grass *et al.*,[24] who worked with Ag-modified Pt nanoparticles supported on mesoporous silica (SBA–15). They used Ag to control the shape of Pt nanoparticles and were able to remove Ag selectively to produce highly active Pt catalysts for hydrocarbon conversions.

Huang *et al*.[4] investigated the Pd and PdAg bimetallic catalysts in the Na^+-ß-zeolite and also used FTIR spectroscopy of adsorbed CO as a characterization technique. Their goal was to achieve a higher selectivity of PdAg catalysts for the hydrogenation of acetylene in the presence of ethylene.

Ryoo *et al.*[25] synthesized AgPt bimetallic clusters in NaY zeolite and confirmed it with EXAFS results.

The goal of this study is to understand the alloying process in two similar and at the same time different systems: PdAg and PtAg, supported on NaY zeolite. There are several important points: to determine, if the metals are alloying and to confirm it in the case they are; to understand how exactly they are alloying and to indicate the effects of alloying. It is also important to follow the changes varying the metal ratio in bimetallic alloys and to discover the differences between PdAg and PtAg systems.

1.2 Organization of the Dissertation

The dissertation has five main parts. In the *Introduction* a motivation is given, a short overview of studies in the research field and the aims of the work. It is followed by the chapter *Fundamentals* which contains important information about zeolites, their structure and applications; as well the techniques used for the characterization of the zeolites. A short subchapter is dedicated to the nanoclusters and their particular properties. The novel properties of small bimetallic clusters and clusters supported in zeolites are also given.

The chapter *Experimental methods* introduces the principles of the techniques in use: Infrared spectroscopy in detail; Electron Paramagnetic Resonance spectroscopy, nitrogen sorption analysis and Extended X-ray Absorption Fine Structure methodic, briefly.

In the chapter *Experimental details and sample characterization* one can read about the particular samples, how they were synthesized and prepared for the measurements. The instrumentation details and the results of atomic absorption spectroscopy and nitrogen sorption analysis measurements are also given.

The two chapters *Experimental Results and Discussion* for AgPd and AgPt systems present the experimental data obtained by measurements and the discussions. Then, the possible geometry and the corresponding effects of alloying are summarized in the chapter *Conclusions and comparison of PdAg and PtAg systems*. As one can see from the name, this chapter also contains a comparison of PtAg and PdAg distinct alloy structures.

The *Summary* resumes the results and ends this work.

2 Fundamentals

This chapter provides an important information about zeolites and particular properties of metal nanoclusters. Fundamentals and applications as well as synthesis and characterization of zeolitic microporous materials are fully treated in the books edited by Jens Weitkamp and Lothar Puppe;[26] Donald W. Breck;[27] edited by H. van Bekkum, E. M. Flanigen, P. A. Jacobs, J. C. Jansen;[9] and by J. B. Nagy, P. Bodart, I. Hannus, I. Kirisci.[28] These books were used when writing this overview.

2.1 Zeolites

Zeolites occur in nature and have been known for almost 250 years as aluminosilicate minerals. They are of great interest as heterogeneous catalysts, but since naturally occurring zeolites almost always contain undesired impurity phases, the synthetic porous material are preferably used for catalytic purposes.

2.1.1 General information

Structurally the zeolites are formed by combining a framework of tetrahedra TO_4 (T = Si, Al, P, Ga, Ge or B) linked to each other by sharing all of the oxygen, to form subunits, and finally infinite lattices by repeat of identical building blocks (unit cells). This structure is well-defined and has a regular array of cages, cavities and channels.

The presence of trivalent T-atoms (Al) in aluminosilicate zeolites generates negative framework charges. These charges can be compensated either by pentavalent T-atoms in the neighborhood (e.g., P in aluminophosphates or $AlPO_4$'s), or by the presence of cationic species.

The structural formula of a zeolite is best expressed for the crystallographic unit cell as: $M_{x/n}[(AlO_2)_x(SiO_2)_y]\cdot wH_2O$, where M is the cation of valence n, w is the number of water molecules.[9] The removal of water by a heating gives rise to a regular porous structure of molecular dimensions, responsible for the unique properties of zeolites. The ratio y/x (Si/Al) usually has values of 1–5 depending upon the structure. This value can also reach 100 for high silica zeolites.[9] The cations (usually alkali and/or ammonium ions) are mobile and may be exchanged by other cations. The size of a synthetic crystal is generally between a fraction of a micrometer and several hundred micrometers. The diameter of the channels and cavities varies according to the structure from 0.3 to 1.3 nm.[9]

In addition to molecular sieving and to ion exchange properties, the zeolite structure is also characterized by other interesting features that will govern their behavior towards physico-chemical treatment, adsorption and acidic strength or catalytic site geometry.

One of these properties is the non random arrangement of AlO_4 and SiO_4 (or other TO_4 units): generally, in zeolite structures Al-O-Al linkages are avoided as stated by Loewenstein's rule. An allowed Si-O-Al linkage results in a long-rage order or the three-dimensional structure.[28]

Zeolite structures are also not static systems. Parameters such as temperature, pressure, sorbed molecules, or the cation species occluded in a zeolite affect the zeolite, usually on bond angle and bond length, leading to the modification of the zeolite symmetry.

First experiments on a zeolite synthesis in the middle of the 19th century were performed to reproduce the natural zeolites. Then, the first zeolite with a structure without corresponding natural minerals, zeolite A, was synthesized. With time, numerous systematic studies of zeolite synthesis have been carried out and have resulted in the preparation of species with different structures and chemical compositions. However, a lot of work is still to be done to fully understand all the factors governing the zeolite crystallization. Indeed, not all the natural zeolite minerals have been reproduced in the laboratory.

The synthesis of a zeolite involves the preparation of an inhomogeneous gel, obtained by combining a silica source and an alumina source in water, under basic pH. Cations can be added to the gel as their oxide, hydroxide or salts; they act in the synthesis as OH^- ion source, as electrolyte, as structure directing agent, or as counter ions of the formed anionic framework.[28]

2.1.2 Ion exchange

The ion-exchange capacity of a zeolite depends on the chemical composition; that is, a higher ion-exchange capacity is observed in zeolites of low SiO_2/Al_2O_3 ratio.[26]

The ion exchange is generally carried out in aqueous systems. One advantage of zeolites for ion exchange is the availability of a great variety of structures with different pore size; a disadvantage is the frequently lower capacity and the lower stability at extreme pH values. When the zeolite crystals are immersed in an aqueous electrolyte, the zeolitic ions communicate with the zeolite-external solution resulting in an exchange of ions between the solid phase and the solution. Since the anionic charges of the framework are fixed, the number of cationic charges within the zeolite pore is constant.

The ion exchange, for example, between Na cations of a zeolite and Pt cations from a solution, may be expressed by the following equation:

$$2Na_Z^+ + Pt_S^{2+} \leftrightarrow 2Na_S^+ + Pt_Z^{2+} \qquad (2.1)$$

The rate of the ion exchange depends on the concentration of ions, and of a size capable of penetrating the pores of the zeolite. The anions associated with the cations in a solution are usually excluded from the zeolite due to the repulsion from the negative charges of the zeolite framework. The ion sieving selectivity greatly depends not only on the size of the pore apertures but also on the hydrophilic or hydrophobic character of the zeolite. Van der Waals interactions between the ions and the walls of the cavities or channels have also to be taken into account. In addition, the complication arises from the fact that the adsorbed cations do not occupy the same adsorption sites in the zeolite.[26]

The ion exchange occurs usually at moderate temperatures while the solution with the suspended zeolite is stirred. Afterwards, the zeolite should be dried and calcined to remove water and other solution or organic residues.

This process is also available for the exchange from non-aqueous solutions as well as for the solid state cationic exchange.

It is well-known that transition metal ions and metal particles are very important catalytic centers. The introduction of these ions/ particles into zeolites modify their properties: they exhibit physical and chemical properties often not found in known complexes; they often are low coordinated and bind molecules specifically; they can be moved from one stable position to another when bonded with molecules; finally, they can induce specific chemical reactions in the sorbed molecules. Active organometallic catalysts within the intracrystalline volume of the zeolite structure are widely used as cracking catalysts in treatment of crude oil.[28]

2.1.3 Structure of Y Zeolite

Zeolite Y, which was used in this work, has the same framework topology as a natural faujasite (pure cubic, $Fd\bar{3}m$, a = 24.3 Å).[29] Synthetic faujasite materials are mainly zeolite X (high Al content, Si/Al ratio close to 1) and zeolite Y (higher Si/Al ratio).

The framework structure of Y zeolite consists of truncated octahedra (β-cages or sodalite cages) connected through six-membered rings (6R) to form double-six rings (D6R, also called hexagonal prisms) in a tetrahedral arrangement (Figure 2.1, modified from[11]).

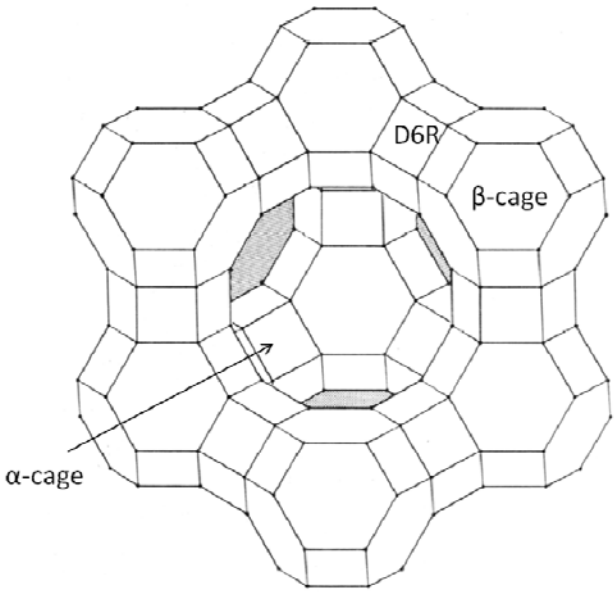

Figure 2.1: Framework structure of Y zeolite (only tetrahedral atoms are shown) with indication of the α- and β-cages and hexagonal prisms (D6R).[11]

The α-cages or supercages are accessible through four nearly planar 12-membered rings (12R) with a crystallographic aperture of 7.4 Å and an effective diameter of about 13 Å.[30] The aperture of the 6R of the sodalite cages is 2.2 Å, and the effective diameter is 2.5–2.6 Å. The unit cell contains 8 sodalite cages, 8 supercages, and 16 hexagonal prisms. The total number of tetrahedra is 192 per unit cell and the maximum number of Al is about 76 to 48 per unit cell because adjacent Al tetrahedra are not allowed. The relation between the number of Al atoms and the Si/Al ratio is $N_{Al} = 192/(1+R)$, where $R = N_{Si}/N_{Al}$. R varies from 1.5 to about 3.[27]

This remarkably stable and rigid framework structure contains the largest void space of any known zeolite (to about 50 vol.% of the dehydrated crystal). The framework density is 12.7 T-atoms/1000 $Å^3$. The combination of a large void volume, 12-ring pore openings and 3-dimensinal channel system makes the thermally stable faujasites ideal for many catalytic applications.[9]

Zeolite Y has various positions available for cations (Figure 2.2). There are sites SI in the hexagonal prism (D6R), sites SI' in the center of the 6R just outside the D6R in the sodalite cage, sites SII in the center of the 6R just outside the sodalite cage in the supercage, sites SII' similar in the center of the 6R, but displaced just inside the sodalite cage, and sites SIII with a low symmetry in the supercage on a 4R. This site is believed to be of a higher potential energy than sites I, I' and II. Usually, if SI is occupied, then SI' has no cations, and if site SII is occupied, there are no cations in SII'.

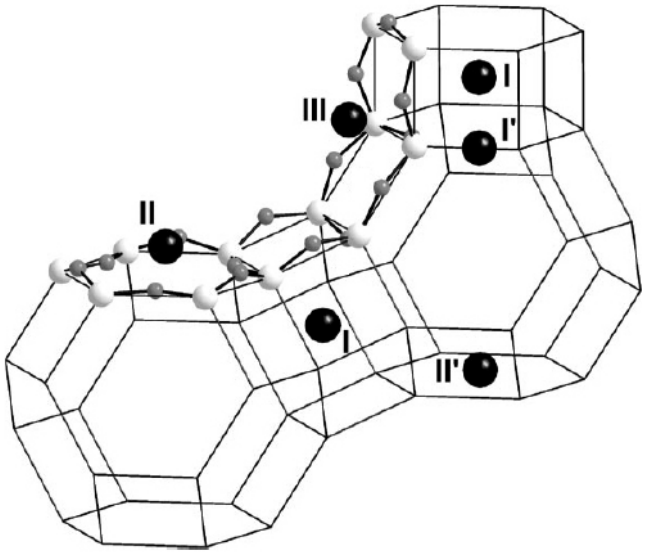

Figure 2.2: The positions of the cation sites in Y zeolite (black balls). T atoms (Si/Al) are designated in light grey and oxygen atoms in dark grey.[31]

The highest negative charge density is in the hexagonal prisms. So, if, for example, Pt^{2+} or Pd^{2+} ions are present in the NaY zeolite framework, there is a strong driving force for the exchange of monovalent Na^{+} ions in the small cages with multivalent transition/ noble metal ions in the supercage. This ion migration is an activated process: at high calcination temperatures, the migration of the transition metal ions to smaller cages competes kinetically with the ligand destruction. The ion location after the calcination is decisive, because the position of the metal ions strongly influences the particle formation and growth processes during the reduction step.[28]

2.1.4 Characterization techniques

Main physico-chemical techniques for the zeolite structure determination are: X-Ray powder/single crystal Diffraction (XRD), High Resolution Electron Microscopy (HREM),

Nuclear Magnetic Resonance (NMR) spectroscopy, adsorption techniques and Infrared (IR) spectroscopy.

XRD provides information about the crystal structure of zeolites (the TO_2 skeleton and the occluded species), HREM gives an insight on zeolite symmetries, and, at high resolution, can even see pore structures. NMR spectroscopy is suited for the study of the surroundings of T-atoms or extraframework species. Multinuclear NMR is one of the best methods to obtain the silicon-aluminum ordering in zeolites and the state of the various elements in the framework.[28]

Adsorptions techniques are used to study the pore structure. Atomic Absorption Spectroscopy (AAS) and Induced Coupled Plasma (ICP) are applied to determine the accurate chemical composition of zeolites. Thermal analysis techniques, such as, for instance, Differential Thermal Gravimetry (DTG), give information on the water content and the occluded organic molecules.[28]

For a long time, IR spectroscopy had been the mainly used spectroscopic technique to characterize the zeolites. The main areas of the application have been and still are: investigations of framework properties; studies of sites of the zeolite lattice, being relevant for the adsorption or catalysis; characterizations of zeolite/ adsorbate systems; and measurements related to the motion of guest molecules in the pores and cavities of a zeolite.[26]

Electron Paramagnetic Resonance (EPR) spectroscopy is useful to determine the environment of the exchanged paramagnetic metal ions in the zeolite supports.

2.1.5 Applications of zeolites

The properties of an ion exchange, sorption and diffusion are among the most important properties of microporous materials. Since the cages and channels are of molecular dimensions, the microporous materials show the molecular sieving effect, allowing the entrance of certain molecules and excluding the others due to their too large size. Once the molecules or ions are adsorbed in the inner pores of these materials, they have to diffuse through the channels and cavities to reach a specific adsorption site or a catalytic site where they can be transformed. In that respect, the zeolite can be compared to the active sites of enzymes. The acid-base properties of zeolites are of most importance in catalysis. Solid acid catalysts are involved in the oil and chemical industries.

The first use of a zeolite as a catalysts occurred in 1959 when researchers tested zeolite Y as an isomerisation catalyst.[28] Later, zeolite A was used as a “shape selective catalyst” and

zeolite X as a cracking catalyst. The high silica materials allowed the development of new processes based on their shape selective properties. The zeolites were modified by dealumination techniques, by the ion-exchange, etc.; Si and Al were replaced by other elements, which resulted in the discovery of numerous new structures and chemical composition ranges. Finally, the techniques, developed to introduce metals as active sites in the zeolite, have resulted in "ship-in-a-bottle" complexes in the cavities, allowing a fine control of the chemical properties.[28]

Zeolites can be also used in biochemistry, agro-industry, detergents, soil improvement, nuclear industry, energy storage and textile industry. The most important of these applications is the use of zeolites as ion-exchangers to remove Ca^{2+} and Mg^{2+} ions from washing water to prevent their precipitation by surfactants. Some zeolites – such as mordenite and clinoptilolite – are used to remove heavy metals and ammonia from waste waters.[28]

2.2 Nanoclusters

Clusters are aggregates of between a few and many millions of atoms or molecules. They may consist of identical atoms, or molecules, of two, or more different species.

2.2.1 Nanoproperties of metal clusters

A metal cluster may be defined as a group of two or more metal atoms, in which there are substantial and direct bonds between the metal atoms. The term *metal cluster* was coined by F. A. Cotton in the early 1960's concomitant with the discovery of many such units. Interest in metal cluster compounds stems from their unique structural diversity, as model compounds for studying fundamental reactions on surfaces, especially in heterogeneous catalysis and many other potential applications.[32] Particles with a size between 1 and 100 nm are normally regarded as *nanomaterials*. Near-spherical particles which are smaller tham 10 nm are typical called *nanoclusters*. The number of atoms in a cluster increases greatly with its diameter. Clusters may have a symmetrical structure which is, however, often different in symmetry from the one of the bulk. They may also have an irregular or amorphous shape.[33]

It is below a dimension of 100 nm where properties such as melting point, color (i.e., band gap and wavelength of optical transitions), ionization potential, hardness, catalytic activity and selectivity, or magnetic properties such as coercivity, permeability and saturation magnetization, vary with size.[33] For example, palladium which is non-magnetic in the solid state can give rise to non-zero magnetic moment in discrete clusters. A common example is also the depression of the melting temperature in metallic systems at a nanoscale.[34] Noble metal nanoparticles also possess interesting optical properties. When these nanoparticles are embedded in appropriate glassy hosts they show nonlinear and optical limiting properties useful in sensors and ultrafast optical communications (switches).[35]

There are basically two types of size-dependent effects: smoothly scalable ones which are related to the fraction of atoms at the surface, and quantum effects which show discontinuous behavior due to the completion of shells in systems with delocalized electrons.[36] Quantum size effects are observed in metal and semiconductor fine particles if their size is small enough so that the spacing between the discrete levels in the electronic energy spectrum becomes comparable with some of the characteristic energy parameters like kT, μH, $\hbar\omega$, etc., thereby giving rise to changes in the thermodynamic, magnetic and optical properties, respectively. So, nanocristalline materials have been found to exhibit increased strength and

hardness, enhanced diffusivity, improved ductility, reduced density, etc., compared to the bulk.[8] Small metal clusters also show enhanced activity and selectivity due to the uncompensated spins at the cluster surface.[37]

But another reason for the interest in clusters is the size-depend evolution of cluster properties. Their chemical and physical properties may be tuned by varying the composition and atomic ordering, as well as the size of clusters.[38] A detailed understanding of their structural and thermal properties is of great importance for the controlled preparation and design of such clusters.[39]

The unusual properties of nanoparticles of noble metals lead to applications in semiconductors, catalysis, photonic crystals and magnetic materials.

2.2.2 Bimetallic systems

The range of properties of metallic systems can be greatly extended by taking mixtures of elements to generate intermetallic compounds and alloys. In many cases, there is an enhancement in specific properties upon alloying, due to the synergistic effects, and the rich diversity of compositions, structures and properties of metallic alloys has led to widespread applications in electronics, engineering and catalysis.[38] Both ligand effects (i.e., an electronic factor due to the change in electron density) and ensemble effects (i.e., a surface structure factor due to the positioning of different atom types) can contribute to the synergistic effects often observed for bimetallic surfaces and particles.[40] The existence of an electron transfer between metals has been clearly demonstrated in single crystal bimetallic samples, for example, in cases of Ag/Pd(100)[41] and Ag/Pt(111).[42] A so called “initial state effect” was also observed for bimetallic particles in highly dispersed systems. It indicates a change in electron density due to the electron transfer between the components of the bimetallic system.[1]

In fact, bimetallic nanoparticles played an important role in improving the catalyst quality, changing the surface plasmon band, and regulating the magnetic properties. Because of these special properties that are brought about by the change on surface and structure caused by alloying, control of the composition distribution of bimetallic nanoparticles is crucial to the improvement of particle properties.[19] Bimetallic catalysts have also been considered to be valuable for investigating the relationship between the catalytic activity and the structure of catalysts.[34]

2.2.3 Clusters in zeolites

The zeolite nanometric channels and cavities provide a perfect environment for the formation of metal nanoclusters, and such systems are widely used in a catalytic world.

In recent years, tiny metal clusters encaged in zeolites have attracted a special attention due to their higher catalytic activity and selectivity.[23]

In particular, *platinum* clusters dispersed in zeolites are highly active catalysts for the oxidation of CO and residual hydrocarbons in automotive exhaust catalysis and for the hydrogenation in petrochemical reactions and other commercial applications.[37]

Zeolite-supported *palladium* catalysts are active for various reactions such as hydrogenation, the dimerization of small olefins, and hydrocarbon conversion. Their catalytic properties are strongly dependent on the nature and location of the metal ions and on their accessibility to and coordination with adsorbate molecules.[43] Palladium exchanged X and Y zeolites have been found to exhibit high catalytic activities for ethylene dimerization.[44]

Silver-exchanged zeolites have been of great interest because of their potential utilization in light-write and light-erase materials, and in many possible applications as catalysts in several chemical reactions, such as cleavage of water into hydrogen and oxygen, ethanol oxidation to acetaldehyde, isomerization of n-butenes as well as aromatization of alkanes, alkenes, and methanol. Ag^{+}-exchanged zeolites have also been widely studied in various NO_x removal processes.[45]

3 Experimental methods

There are many ways to provide data about the physicochemical properties of transition metal ions on surfaces. Information about coordination, oxidation states and dispersion of supported transition metal ions could be obtained. But it is clear that no characterization technique will be capable of providing all the information needed for a full and a successful characterization; that is why a researcher needs a multitechnique approach. In this chapter, principles of the experimental techniques used in this work, such as Infrared (IR), Electron Paramagnetic Resonance (EPR) spectroscopes, Extended X-ray Absorption Fine Structure (EXAFS) and nitrogen sorption analysis are briefly summarized.

3.1 Infrared Spectroscopy

Vibrational spectroscopy is among the most popular spectroscopic techniques for characterizing heterogeneous catalysts and the major method of this work. Theoretical and practical aspects of IR spectroscopy are in detail described in the books by Helmut Günzler and Hans-U. Gremlich;[46] or Gerhard Herzberg;[47] edited by Bert M. Weckhuysen;[48] or by Norman B. Colthup, Lawrence H. Daly, Stephen E. Wiberley;[49] all of these books were used to give an overview of this technique here.

The common application of infrared spectroscopy for studying metals on surfaces is to identify the adsorbed species and to study the way these species are chemisorbed/ anchored on the catalysts surface.

Infrared radiation is just suitable to excite the vibrations in the molecule. The frequencies, which are needed for the excitation of vibrations, lie in the IR radiation region (wavelengths of 780 nm–50 μm or wavenumbers of 12800–200 cm^{-1}). If the energy quantities are lower, the molecules can only be induced to rotate, for small molecules the frequencies still lie in the longwave region of the IR spectrum (far IR, over 50 μm = below 200 cm^{-1}), but generally in the microwave region.[46]

3.1.1 Molecular Vibration

The two atoms in a diatomic molecule vibrate in phase about their equilibrium position in the molecule in opposite direction, being kept together by a weightless elastic spring, which is characterized by the elastic *force constant k* (Hooke's law). This classical physical model of the atomic vibrations is that of the *harmonic oscillator*.

The resulting potential energy is:[48]

$$E_{vib} = \frac{1}{2}k(r - r_{eq})^2 \qquad (3.1)$$

where r_{eq} is the equilibrium bond distance, and the *vibrational frequency* is:[46]

$$\upsilon_{vib} = \frac{1}{2\pi}\sqrt{\frac{k}{\mu}} \qquad (3.2)$$

with μ = reduced mass = $m_1 \times m_2/(m_1+m_2)$.

In vibrational spectroscopy, one usually uses *wavenumbers* in cm^{-1} instead of frequencies υ_{vib} in s^{-1} or Hz: [48]

$$\tilde{\upsilon} = \frac{1}{2\pi c}\sqrt{\frac{k}{\mu}} \qquad (3.3)$$

Where c is the velocity of light in vacuum, 3×10^8 m s^{-1}.

From *(3.3)*, one can conclude that the vibrational frequency of a chemical bond is related to the masses of the vibrating atoms and the force constant. The larger the force constant, the higher the vibrational frequency. On the other hand, vibration frequencies relate inversely to the masses of the vibrating atoms: a light atom oscillates faster than a heavy one. This is illustrated in Table 3.1 for the CO molecule with different isotopic combinations:

Table 3.1: Vibration frequency of CO with different isotopic combinations.[48]

molecule	wavenumber (cm^{-1})
$^{12}C^{16}O$	2143
$^{13}C^{16}O$	2096
$^{12}C^{18}O$	2091
$^{13}C^{18}O$	2041

In quantum mechanics the harmonic vibration of a diatomic molecule is treated by solving the corresponding time-independent Schrödinger equation. The solution is that the vibrational energy is quantized according to:[48]

$$E_{vib} = h\upsilon_{vib}\left(\upsilon + \frac{1}{2}\right) \text{ with } \upsilon = 0, 1, 2,\ldots. \qquad (3.4)$$

υ is the *vibrational quantum number*, h is the Planck constant, 6.626×10^{-34} Js. At any temperature T, the systems are distributed over the energy levels according to Boltzmann's

law. At room temperature, only the level $\upsilon = 0$ is occupied. Thus, when the molecules interact with the light of frequency υ_{vib}, they absorb the photon and are excited to the level $\upsilon = 1$.

3.1.2 Vibrational spectra

Within absorbing energy, a transition occurs in the molecule from energy state E'' of the particular atomic group to the energy state E' having a higher quantum number.[46]

$$E' - E'' = h\upsilon = hc\tilde{\upsilon} \tag{3.5}$$

and

$$\tilde{\upsilon} = \frac{E'}{hc} - \frac{E''}{hc} \tag{3.6}$$

Each of the two ratios in *(3.6)* is defined as a *term*. The wavenumber of absorbed radiation directly results from the term difference of an energy transition.

For the terms of a harmonic oscillator, a vibrational term G(υ) is:[46]

$$G(\upsilon) = \frac{E_\upsilon}{hc} = \tilde{\upsilon}(\upsilon + \frac{1}{2}) \tag{3.7}$$

For the selection principle applicable to the harmonic oscillator ($\Delta\upsilon = \pm 1$) there is only one single absorption band in the IR spectrum at the wavenumber $\tilde{\upsilon}$.

But the real potential energy curve of a diatomic molecule deviates from that of the harmonic oscillator (parabola). For $r < r_{eq}$ this is due to the electronic repulsion; for $r > r_{eq}$ it can be ascribed to electronic rearrangements as the atoms move further apart. This difference is called *anharmonicity*. The transition $\upsilon = 0$ to $\upsilon = 1$ for the anharmonic oscillator is:[48]

$$h\upsilon_a = E_1 - E_0 = (1 - 2\chi_a)h\upsilon_{vib} \tag{3.8}$$

χ_a is the *anharmonicity constant*, which is always small but positive, υ_a is the vibrational frequency of the anharmonic oscillator, which is lower than that of the harmonic vibration υ_{vib}. The difference between the energy levels of the harmonic and anharmonic vibrations increases with quantum number υ. The second consequence of an anharmonicity is that besides $\Delta\upsilon = \pm 1$, the higher order transitions $\Delta\upsilon = \pm 2, \pm 3, \ldots$ are also allowed and visible in the spectra. These bonds are called *overtones* and are usually much less intense than the fundamental ones with $\Delta\upsilon = \pm 1$. For example, CO has $\chi_a = 0.0061$. This results in a vibration at a lower wavenumber (2143 cm^{-1}) in comparison with that of the ideal harmonic oscillator approach (2169 cm^{-1}). The first overtone for CO is at 4259 cm^{-1}.[48]

3.1.3 Molecular Rotation

According to classical mechanics, the rotational energy E_{rot} of a linear molecule (a model of a *rigid rotator*) is defined by:[46]

$$E_{rot} = \frac{1}{2} I w^2 = \frac{1}{2} I (2\pi \upsilon_{rot})^2 \qquad (3.9)$$

with the moment of inertia $I = \mu r^2$ and the angular velocity $w = 2\pi\upsilon_{rot}$, where μ is the reduced mass and υ_{rot} is the rotational frequency. The solution of the corresponding Schrödinger equation yields the discrete energy eigenvalues:[46]

$$E_{rot} = \frac{h^2}{8\pi^2 I} J(J+1) \qquad (3.10)$$

The parameter *J* is the *rotational quantum number*. It takes all positive integers as value starting from zero. In contrast to the vibrational state, the molecule in the rotational ground state $J = 0$ has no zero-point energy.

Thus, there is a series of discrete energy levels whose energy increases quadratically with increasing *J*. The selection rule is $\Delta J = \pm 1$.

3.1.4 Rotational spectra

The rotational term E/hc (units cm^{-1}), according to (3.10), is given by:[46]

$$F(J) = \frac{E}{hc} = \frac{h}{8\pi^2 cI} J(J+1) = BJ(J+1) \qquad (3.11)$$

where B is the *rotational constant:*[46]

$$B = \frac{h}{8\pi^2 cI} = \frac{27.986}{I} \times 10^{-47} cm^{-1} \qquad (3.12)$$

According to (3.9) and (3.10), the rotational frequency is:[49]

$$\upsilon_{rot} = c\ 2B\sqrt{J(J+1)} \approx\ c\ 2BJ \qquad (3.13)$$

The difference of two terms with the rotational quantum numbers *J′* and *J″* is then, because of the selection rule, $\Delta F = 2B(J+1)$. At $J = 0$, the first line lies at $\tilde{\upsilon} = 2B$.

The spectrum of the simple rigid rotator consists of a series of equidistant lines with the distance of 2B. Since the real molecule is not a rigid object, the rotational constant B decreases with increasing rotational quantum number *J* (due to the changes of interatomic distance *r* and therefore the moment of inertia *I*). The term differences ΔF thus increase less than expected for the rigid rotator, and the line distances become shorter than $2B$ with the increasing quantum number.

3.1.5 Rotational–Vibrational Interaction and Spectra

The molecules rotate and vibrate simultaneously. Thus, there is a system with the energy composed of the energy fractions of the anharmonic oscillator and that of the non-rigid rotator. The vibrational-rotational interaction results in an increase of the average interatomic distance and, therefore of the moment of inertia. The *actual rotational constant*, given by:[46]

$$B_v = B - a(v + \frac{1}{2}) \qquad (3.14)$$

is smaller than the rotational constant B (a is a molecule-specific constant).

The selection rules for the rotating oscillator/ vibrating rotator are the same as in separate cases. But now $\Delta\upsilon = 0$ and $\Delta J = \pm 1$ are allowed, which means that the rotating oscillator can also absorb corresponding energy quantities exclusively for rotational transition. The absorption spectrum contains a larger number of individual lines, the series with $\Delta J = +1$ is calls the R-branch and the series with $\Delta J = -1$ as the P-branch. They are separated by a gap at the wavenumber corresponding to the pure vibrational transition ($\Delta J = 0$). Due to the interaction between rotation and vibration the line distances on both sides of the gap are unequal. With the increasing distance from the center, the line distances decrease in the R-branch but increase in the P-branch.

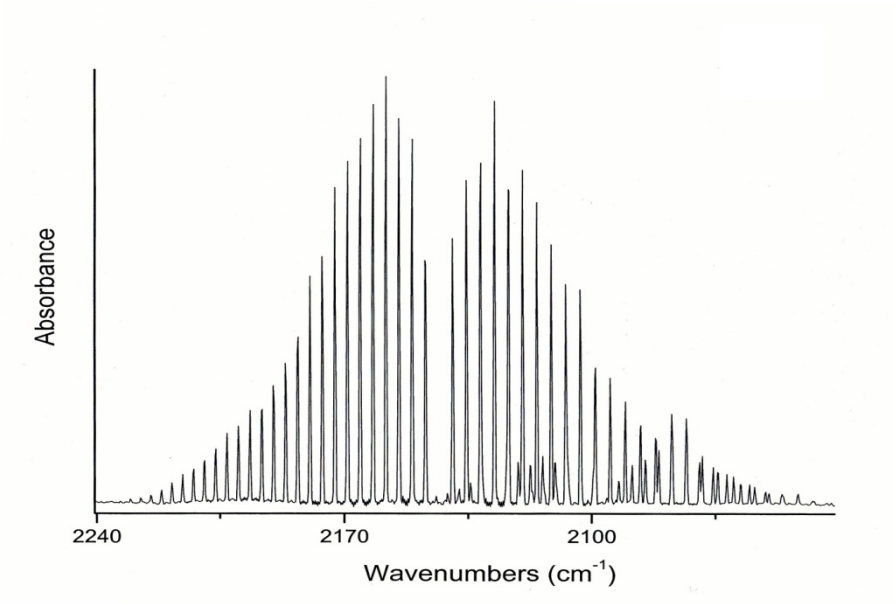

Figure 3.1: Rotational–vibrational spectrum of carbon monoxide (gas).

Figure 3.1 shows the IR spectrum of CO as a typical spectrum of a diatomic rotating oscillator having a clearly recognizable gap in the center as well as decreasing and increasing

line distance in the R- (at higher wavenumbers) and P-branch (at lower wavenumbers), respectively.

The electromagnetic radiation of the corresponding frequency can only then be absorbed by a molecule if a change in the dipole moment is associated with the vibrational excitation of the atomic group concerned. Diatomic molecules with the same atoms, in principle, cannot be excited to vibrate, due to the absence of any dipole moment. However, after adsorption, for example, on a zeolite, the symmetric molecules, as H_2, O_2 or N_2, lose their symmetry and exhibit a vibrational–rotational spectrum. Molecules consisting of various types of atoms can always interact with IR radiation (as HCl or CO). When a dipole moment is not present from the beginning, at least those vibrations are excited for which a dipole moment results from antisymmetric displacement of the center of charge (as in case CO_2, antisymmetric valence vibrations). Vibrations showing no change of the dipole moment are infrared inactive (for example, CO_2, symmetric valence vibrations).

3.1.6 Interpretation of IR Spectra

The position and intensity of absorption bands of a substance are extremely specific to that substance. Like a fingerprint of a person, the IR spectrum is highly characteristic for a substance. In particular, infrared spectra of CO bonded to a metal will be discussed in detail in Section 3.1.9.

The individual bands are often described alone by the band position as well as by the half-intensity width. Furthermore, for qualitative analysis one uses the *Bouguer-Lambert-Beer* law. If I_0 is the intensity of the radiation entering the sample, and I is the intensity transmitted by the sample, then the ratio I/I_0 is called the *transmittance* (T) of the sample. For the sample with thickness d, while the absorbing component has a concentration c, then the fundamental equation governing the absorption of radiation as a function of transmittance is:[49]

$$T = I/I_0 = 10^{-\varepsilon cd} \qquad (3.15)$$

The constant ε is called the *absorptivity* and is characteristic for a specific sample at a specific wavelength. The $\log_{10}I_0/I$ is given the symbol A and is called the *absorbance*. Beer's law is usually written as a function of the absorbance:[49]

$$A = log_{10}I_0/I = \varepsilon cd \qquad (3.16)$$

In the IR spectrum a measure for the radiation adsorption of a substance is the intensity of its bands. The determined total area of a single band is called the *integral absorbance*.

A number of effects contribute to the width of spectroscopic lines. In gaseous samples one important broadening process is the Doppler effect, in which radiation is shifted in frequency when the source is moving towards or away from the observer. The lifetime broadening is due to quantum mechanical effects.

For the band fitting one can use theoretically functions – the Lorentz or the Gauss function. The Lorentz function is applicable for the profiles of rotational–vibrational lines of gases, when the broadening is mainly caused by a collision process (pressure broadening). In contrast, in the lower pressure regions of gases, the Doppler broadening predominates, which leads to Gauss curves. It is favorable for neighboring lines. The band fitting becomes more complex when various bands overlap one another.

3.1.7 Fourier Transform Spectroscopy

One distinguishes between dispersive and non-dispersive (Fourier transform) infrared spectroscopy. The older design of dispersive instruments employs prisms or gratings as monochromators in order to select IR radiation of a certain frequency from the originally continuous radiation generated by a source. The dispersive spectrometers are generally double-beam instruments, where one beam (I_0) does not transmit the sample and is used for a comparison. The energy of another beam I, received by the detectors, is lower than I_0, and a plot of the transmittance *vs.* the frequencies provides the conventional IR spectrum.

The concept of FTIR is completely different. In a FTIR instrument, the polychromic source is modulated into an interferogram which contains the entire frequency region of the source. Therefore, all frequencies are measured simultaneously. It allows to obtain the high quality spectra with a large signal-to-noise ratio. This advantage is most useful when the available spectral energy is low, or when a large scale expansion is needed to record very weak bands. In addition, the spectra can be recorded in less time.

3.1.8 The Fourier Transform Spectrometer

The main parts of the FT spectrometer are presented in Figure 3.2. A source of the infrared radiation is usually some solid material heated to the incandescence by an electric current. After the source there must be some kind of the device to analyze the radiation so that the intensity can be evaluated for each wavelength resolution effect. In Fourier transform spectroscopy one uses a Michelson interferometer. The device consists of two plane mirrors, one fixed and one moveable, and a beam splitter. One type of a beam splitter is a thin layer of

germanium on an IR-transmitting support. The radiation from the source strikes the beam splitter at 45º, and it transmits half of the radiation and reflects the other half. The transmitted and reflected beams strike two mirrors – movable and fixed, respectively – and so the interference occurs at the beam splitter where the radiation from the two mirrors combines.

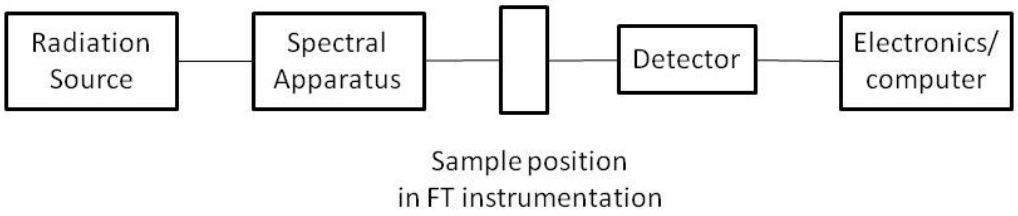

Figure 3.2: Schematic design of an IR spectrometer.

The sample is placed between the interferometer and the detector. Cells for holding samples or windows within a spectrometer must be made of infrared transmitting material. KBr is one of the most popular materials for solid samples, NaCl – for liquids.

The detector is used for converting the optical signal into easily measurable electrical signals. This is aided by corresponding electronics for amplifying and digitizing the signals. There are two basic types of the infrared detectors: thermal detectors, which measure the heating effects of radiation and respond equally well to all wavelengths, and selective detectors, whose response is dependent on the wavelength.

3.1.9 Infrared spectroscopy of metal carbonyls

It has been found that CO molecule mainly shows two types of bonding – terminal and bridging. As the C–O stretching frequency is quite sensitive to small changes in the electronic environment, one can identify these by IR spectral studies. The C–O stretching frequencies of terminal carbonyls are observed in the range of 2120–1850 cm^{-1}, usually similar to the free carbon monoxide molecule (2143 cm^{-1}), while bridging carbonyl stretching frequencies are observed in the range of 1850–1750 cm^{-1}.[32] Different types of bonding are presented in Figure 3.3.

CO typically binds in terminal mode through carbon. However, bridging carbonyls are not uncommon and often undergo exchange with terminal carbonyls. A variant of a bridging carbonyl is the “semi-bridging” carbonyl, in which the M–CO–M bond is asymmetric rather

than symmetric. These can be considered as being intermediate between terminal and bridging carbonyls. In another unsymmetrical form called the σ/π bridge, CO acts as a four or six electron donor, and shows a side-on coordination. Isocarbonyl coordination through the oxygen atom was very rarely observed (for metals such as titanium, aluminum and the lanthanides).[32]

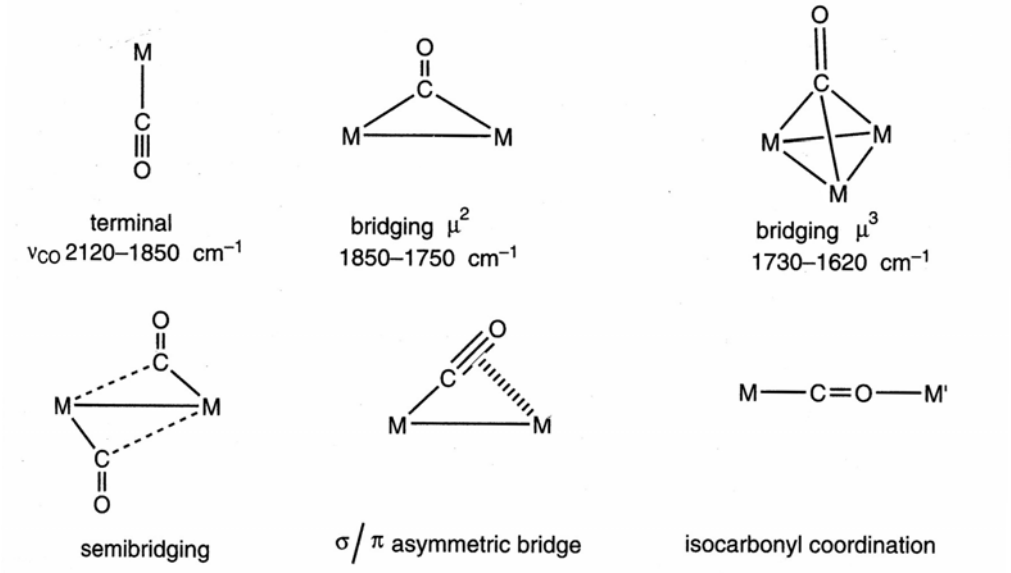

Figure 3.3: Various bonding modes of CO.[32]

The bonding of CO to a metal can be described as consisting of two components. The first component is a two electron donation of the lone pair on carbon (coordination exclusively through the oxygen is extremely rare) into a vacant metal d orbital (Figure 3.4).

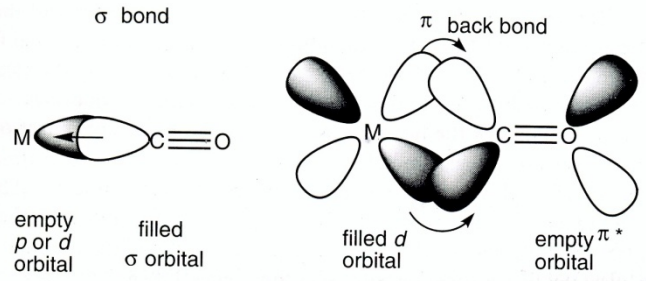

Figure 3.4: Orbital overlap for σ and πbonding in metal carbonyls.[32]

This electron donation makes the metal more electron rich, and in order to compensate for this increased electron density, a *filled* metal d orbital can interact with the *empty* π^* orbital

on the carbonyl ligand to relieve itself of the added electron density. This second component is called π-backbonding (backdonation).

This occupation of the π^* on CO does lead to a decrease of bond order in the carbon monoxide molecule itself. The consequences that one might expect if the C–O bond order was reduced would be a lengthening of the C–O bond, shortening of the M–C bond and a decrease in the carbonyl stretching frequency in the IR spectra (so-called red-shifts of the stretching frequency). As the electron density on a metal increases, more π-backbonding to the CO ligand(s) takes place. This weakens the C–O bond further by pumping more electron density into the formally empty carbonyl π^* orbital. This increases the M–CO bond strength making it more like double-bond M=C=O.

The charge of the metal, and thereby electron density are the essential factors; electronegativity and size of the metal are being projected as influencing the electronic effects, but they are minimal and contribute less to the observed CO stretching frequencies.

3.2 Electron Paramagnetic Resonance Spectroscopy

Electron paramagnetic resonance (EPR) or electron spin resonance (ESR) spectroscopy is a useful method to characterize small paramagnetic clusters and ions in zeolites without destroying their structures. The information about cluster size, structure, charge and local environment can be obtained.[37] This method based on the interaction of an electron spin with a magnetic field in the presence of microwaves. A detailed information about spin resonance spectroscopy can be found in books by John A. Weil and James R. Bolton;[50] Marina Brustolon and Elio Giamello;[51] Neil M. Atherton;[52] and edited by Bert M. Weckhuysen,[48] they were also used when writing this overview.

3.2.1 General principles

All elementary particles; i.e., electrons, protons and neutrons, possess the property of spin. The quantum number associated with the spin property of these elementary particles S is equal to 1/2. The consequence is that all atoms or molecules with unpaired electrons possess a spin S = 1/2, 1, 3/2, 2,...

An electron and a proton can be depicted as a spinning charged body, which is characterized by a *mechanical angular momentum*, which is controlled by the rules of quantum mechanics:[51]

$$\left|\vec{S}\right| = \hbar\sqrt{S(S+1)} \qquad (3.17)$$

where $\hbar$ is the Planck constant divided by 2π. For protons and electrons – both with S = 1/2 – the length of the angular moment vector is equal to $0.87\hbar$. Unlike spinning macroscopic bodies, which can be made to spin in any directions, there are quantized limits to the direction of the angular momentum of elementary particles. First, the number of allowed orientations is given by 2S+1. Thus, for an electron with S= 1/2 only two directions are allowed.[48] These states are usually indicated by letters α and β. The spin vector $\vec{S}$ has components along the *x,y,z* axes of a Cartesian frame. For an electron spin, quantum mechanics requires that S_z be in $\hbar$ units of either 1/2 (α state or spin up (↑)) or –1/2 (β state or spin down (↓)).

Secondly, the allowed values for the z-komponent of the momentum can be deduced using magnetic quantum numbers, m_s:

$$-S \leq m_s \leq +S \qquad (3.18)$$

In the electron case, in the α and β states the components along the z axis assume the m_s values 1/2 and –1/2. In the absence of any preferential direction, any choice for the direction in space of the z axis is allowed. As long as this space isotropy holds, the α and β electron spin states have the same energy and they are said to be *degenerate*, but not if the electron spin interacts with a magnetic field.

Due to its spin, a single isolated electron possesses a magnetic moment:[51]

$$\overrightarrow{\mu_e} = g_e \mu_B \vec{S} \tag{3.19}$$

where μ_B is the *Bohr magneton,* $\mu_B = -\frac{|e|\hbar}{2m_e}$ .The g_e is the *g-factor*, also called the Landé factor. It is equal to 2.002319 for a free electron, when $\mu_B = -9.274\times10^{-24}$ JT^{-1}, with m_e the electron mass 9.1093×10^{-31} kg, and e the electron charge -1.6021×10^{-19} C.[51]

3.2.2 Magnetic interactions

When an external magnetic field $\vec{B}$ is supplied to the system, there is the interaction between an external magnetic field and a spin, due to the existence of magnetic dipole generated by the spinning charged body.

The electron spin energy depends on the orientation of μ_e with respect to $\vec{B}$:[51]

$$E = -\overrightarrow{\mu_e}\vec{B} \tag{3.20}$$

and the Hamiltonian for a free electron in a magnetic field is obtained:[52]

$$H_{ZI} = g_e \mu_B \vec{S}\vec{B} = g_e \mu_B B_0 S_z \tag{3.21}$$

where B_0 is the magnitude of a magnetic field and z axis is along the direction of $\vec{B}$.

Because two states for electron spins are allowed, one observes the splitting of the electron spin energy levels: $E_\beta = -1/2\ g_e\mu_B B_0$ and $E_\alpha = +1/2\ g_e\mu_B B_0$.[48] This effect is called the *Zeeman effect*, and the interaction of a magnetic moment with an external applied magnetic field is called the electron *Zeeman interaction* (Figure 3.5).

The fundamental equation of EPR spectroscopy gives us the energy difference:[51]

$$h\upsilon = E_\alpha - E_\beta = g_e|\mu_B|B_0 \tag{3.22}$$

where υ is the radiation frequency in GHz.

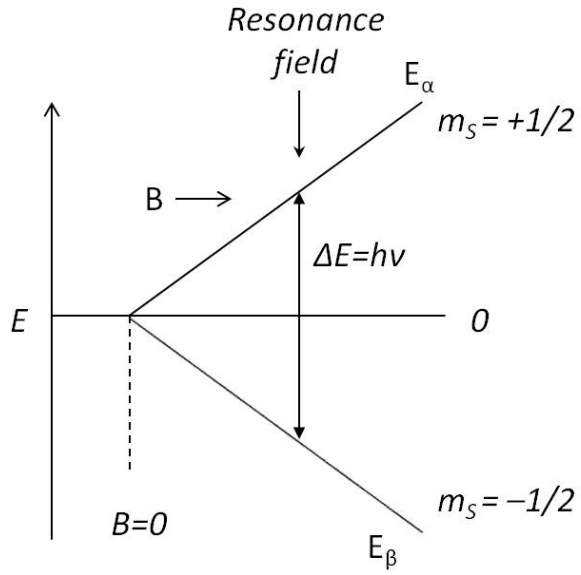

Figure 3.5: Energy-level scheme of a S = 1/2 system, at increasing external magnetic field.

For the spin system to absorb the radiation energy, the oscillating magnetic field $\overrightarrow{B_1}$ associated with the electromagnetic radiation should be in the *xy* plane, which is perpendicular to the static Zeeman field $\overrightarrow{B_0}$.

An isolated electron spin placed in a static magnetic field $\overrightarrow{B_0}$ and in the presence of a microwave oscillating magnetic field $\overrightarrow{B_1}$ perpendicular to $\overrightarrow{B_0}$ undergoes transitions from the low energy level state β to the upper one α, and vice versa. These, absorptions and stimulated emissions, compensate each other. In real chemical systems, the electron spins are, however, never completely isolated. The single unpaired electron is associated with at least one atom and the second contribution to paramagnetism stems from the electron motion in an orbital with *orbital angular momentum* $\vec{L}$. The magnetic moment of an electron is then the sum of two terms: $\mu_e = \mathrm{g}_e\mu_B\vec{S} + \mu_B\vec{L}$.[51] Since the spin motion and orbital motion are not independent of each other and spin and orbit angular momenta are coupled by the spin-orbit coupling, a new Hamiltonian must be added to the electronic Zeeman term:[52]

$$H = \mu_B\vec{B}\left(\vec{L} + \mathrm{g}_e\vec{S}\right) + \lambda\vec{L}\vec{S} = \mu_B\vec{B}\mathbf{g}\vec{S} \qquad (3.23)$$

with λ, the *spin-orbit coupling constant*, for the particular shell in a particular atom, and **g**, the effective g-value. The effect of spin-orbit coupling is to restore a small amount of orbit contribution, which results in a deviation of the g factor from the free electron value g_e. The

shift of the g-value is large for metal complexes, where the electron moves in the nearness of a heavy atom nucleus, and very small for organic radicals which contain only light atoms. The value of **g** depends on the direction of the magnetic field with respect to the molecular axis.

$$H_{LS} = \lambda[L_x S_x + L_y S_y + L_z S_z] \qquad (3.24)$$

The anisotropy in **g** is classified into isotropic (one g-value, $g_{xx} = g_{yy} = g_{zz}$), axial (two g-values, $g_{xx} = g_{yy} = g_{\parallel}$ and $g_{zz} = g_{\perp}$) and rhombic (three g-values, $g_{xx} \neq g_{yy} \neq g_{zz}$).

The magnetic moment of the electron will also undergo additional interactions with local magnetic fields originating from non-zero nuclear spins, which are located on the atom with the unpaired electrons. This coupling is known as the *hyperfine interaction*:[52]

$$H_{HF} = \vec{I}\boldsymbol{A}\vec{S} \qquad (3.25)$$

where **A** is the *hyperfine coupling tensor* (characterized by three orthogonal principle values A_{xx}, A_{yy} and A_{zz}) and $|\vec{I}|$ is the magnitude of the spin angular momentum of a nucleus. By analogy with the mechanical angular momentum S, $|\vec{I}| = \hbar\sqrt{I(I+1)}$, where I is the nuclear spin quantum number. The nuclear magnetic moment is given by:[51]

$$\mu_N = g_N \mu_N \vec{I} \qquad (3.26)$$

where the nuclear magneton $\mu_N = e_p\hbar/2m_p = 5.0507\times10^{-27}$ JT^{-1} with the mass of a proton, $m_p = 1.6726\times10^{-27}$ kg, the charge $e_p = 1.6021\times10^{-19}$ C. g_N is the nuclear g-factor and is equal to 5.5856 for a proton.[51]

The energy of the nuclear spin is influenced by an internal magnetic field similar to a free electron. The nuclear magnetic moment provides an additional magnetic field which influences the magnetic moment of the electron spin. It causes a splitting of the resonance EPR lines into 2I+1 components.

Inside the nucleus the hyperfine field is constant; its energy contribution is called the *contact* (or *Fermi*) contribution, which is:[51]

$$E_{HF} = a\vec{S}\vec{I} \qquad (3.27)$$

where *a* is a constant (*hyperfine coupling constant*), which depends on $|\Psi(0)|^2$, the square of the wavefunction that describes the probability of finding the electron at the nucleus.

If the nuclear spin is not on the atom with the unpaired electron, its interaction is called superhyperfine splitting.

Some nuclei with spins ≥ 1 possess an electric quadrupole moment because of the non-spherical charge distribution in the nucleus. The interaction of such nuclei with an electric field gradient is the *quadrupole interaction*.

If two or more unpaired electrons are present, so that the total spin S is greater than 1/2, one has to take into account the interaction of the electrons with the electric field generated by the surrounding atoms (i.e., the crystal field or ligand field). This interaction causes a splitting of the more than two-fold (Kramers-) degenerate ground state of the electron system even in the absence of an external magnetic field (i.e., *zero field splitting*).

Summarizing, four major different interactions may occur, which influence the behavior of electrons in a magnetic field: (a) the Zeeman interaction, H_{ZI}; (b) the nuclear hyperfine interaction, H_{HF}; (c) the electrostatic quadrupole interaction, H_Q and (d) the zero-field splitting if S > 1/2, H_{FS}. The sum of these interactions results in the total spin Hamiltonian H_T:

$$H_T = H_{ZI} + H_{HF} + H_Q + H_{FS} \qquad (3.28)$$

Not all these interactions can be observed by EPR spectroscopy. It depends on the element, the molecular structure and physical state.

3.2.3 Transition metal ions in EPR

Transition metal ions (TMI) have been investigated intensively by EPR since the introduction of this technique. The number of unpaired electrons of transition metal complexes depends on the ion and its oxidation state, on the symmetry of the coordination, and on the strength of the crystal field. The simplest cases are d^1 and d^9 ions, which always have S = 1/2. For the other ions the spin state depends on the coordination, and the same ion can be in a low spin or high spin state in different compounds. The EPR spectra of transition metal ions, with the exception of S = 1/2 ions, are generally dominated by a zero field splitting term.[51]

The g values of TMIs frequently deviate considerably from that of the free spin because of the orbital angular momentum. For ions in which the d shell is less than half full, $g < g_e$; for ions in which the d shell is greater than half full, $g > g_e$.[50]

3.2.4 EPR Spectrometer

There are nowadays a wide variety of EPR techniques available, each with their own advantages and limitations. In continuous wave EPR (CW-EPR), the sample is subjected to a continuous beam of microwave irradiation of fixed frequency and the magnetic field is swept. One uses also different microwave frequencies or other techniques, such as electron nuclear double resonance (ENDOR) and electron spin echo envelope modulation (ESEEM) spectroscopes. Both these pulsed EPR techniques require the use of advanced instrumental equipment.

The basic components of a classical low-frequency EPR spectrometer are the microwave bridge, the resonator, the magnet system, and the control electronics (Figure 3.6).

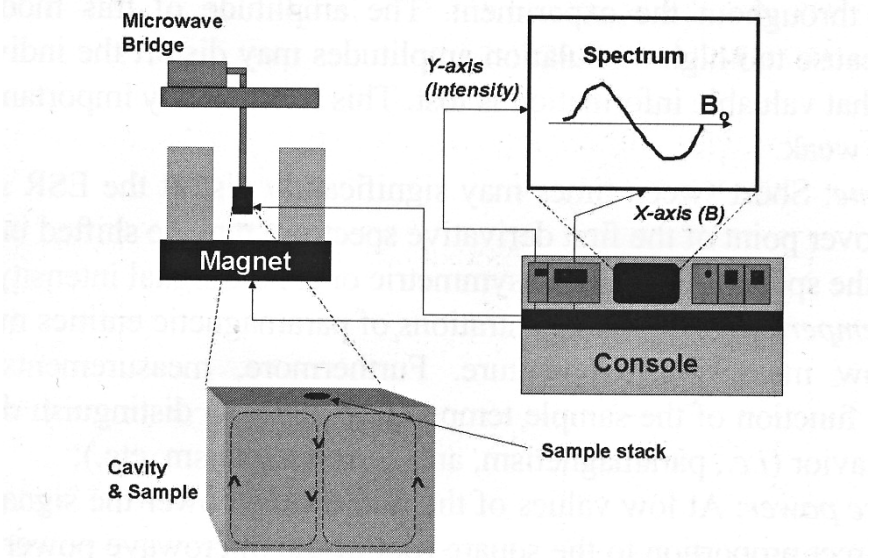

Figure 3.6: General layout of a classical low-frequency EPR spectrometer.[48]

The microwave bridge supplies microwaves at a fixed frequency and chosen power, and the microwave source is a klystron or a gundiode. The microwaves are transmitted to a sample cavity via a waveguide. The sample cavity is a device in which the sample can be irradiated with the microwave energy, but which is also capable of being tuned so that the microwave energy can be reflected back to a detector in the microwave bridge. The design of the cavity depends mainly on the applied microwave frequency because the dimensions of the cavity must match the wavelength of the microwaves.

The microwave frequency is kept constant and the applied magnetic field is varied over a range wherein the microwave absorption is expected. This is called continuous wave electron spin resonance. At this stage, the intensity change of the reflected microwave energy is measured by the detector and the obtained signal is amplified, recorded and stored for the further treatment.

3.2.5 Quantitative analysis

The analysis of the line positions and spectral profile of an EPR spectrum can be done on the basis of the magnetic interactions of the corresponding paramagnetic species. The term "quantitative EPR" refers to the analysis of the signal amplitude to obtain information on the absolute number of unpaired electron spins in the sample or their changes induced by a certain sample treatment. To determine the absolute number of spins in the sample, usually a double resonator and a reference sample with a known number of spins are employed.

The concentration *C* of a paramagnetic entity in a sample is given by:[48]

$$C = \frac{KI}{GP} \tag{3.29}$$

where *K* is a proportionality constant, *I* – the EPR line intensity, *G* – the amplifier gain of the spectrometer and *P* – the EPR transition probability. *K* depends on the properties of the sample cavity, the applied microwave power and modulation amplitude. *I* can be obtained by the double integration of the recorded first derivate spectrum. *K* and *P* mast be identical for the standard and the sample. It means that the sample container, the volume of the sample, the positioning in the sample cavity and the dielectric properties of both samples are identical.

The general formula for calculating the spin concentration [X] using a standard sample of the known concentration [Std] is:[50]

$$[X] = \frac{A_X R_X (Scan_X)^2 G_{Std} (B_m)_{Std} (g_{Std})^2 [S(S+1)]_{Std}}{A_{Std} R_{Std} (Scan_{Std})^2 G_X (B_m)_X (g_X)^2 [S(S+1)]_X} \times [Std] \tag{3.30}$$

with *A* – the measured area under the absorption curve, obtained after double integration of the EPR signal; *Scan* – the horizontal scale, B_m – the modulation amplitude, G – the relative gain of the signal amplifier and *R* – an integrated fraction of the total spectrum. If the same microwave power is used, the Q value of the cavity and the other experimental parameters were constant while measuring the sample and the standard, eq. 3.30 can be simplified to:

$$[X] = \frac{A_X (g_{Std})^2}{A_{Std} (g_X)^2} \times [Std] \qquad (3.31)$$

Absolute determination of paramagnetic entities, especially TMI, can only be done within 10 to 20 % accuracy. This explains why the number of quantitative EPR studies in the field of heterogeneous catalysts is limited.[48]

3.3 Nitrogen Physisorption Studies

Nitrogen sorption analysis is one of the most powerful tools for the determination of the porosity in solid materials. This technique allows the determination of the specific surface area, the pore volume and the pore size distribution.

According to the IUPAC classification, the diameter of micropores ranges from 0.3 to 2 nm, of mesopores from 2 to 50 nm and of macropores from 50 nm up to 100 μm.[9]

The sorption isotherms of relatively inert gases such as N_2 and Ar, typically measured at the condensation temperature of the corresponding gas, reflect the size and shape of the pores. These sorption isotherms can be classified into six principal types and are shown in Figure 3.7:

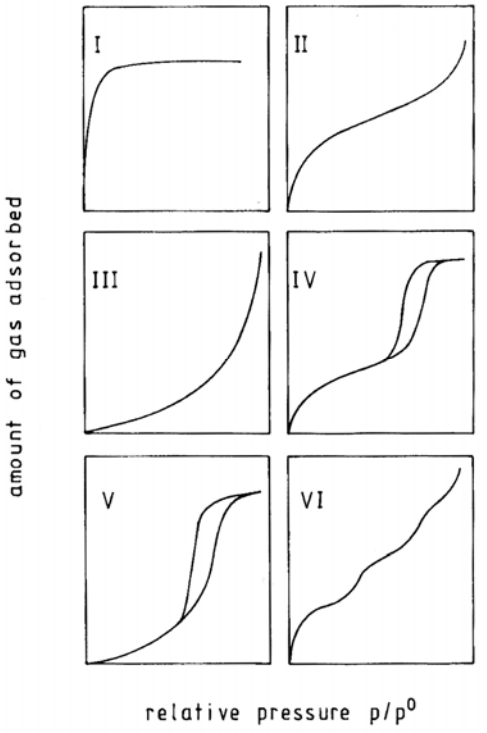

Figure 3.7: Types of sorption isotherms.[9]

Type I describes the adsorption in micropores and is typical for benzene, adsorbed on zeolites; type II is characteristic for the multilayer adsorption on flat surfaces (e.g., N_2 on SiO_2, Al_2O_3); type III and V are usual for weak gas-solid interactions (e.g., H_2O on noble metals); type IV signalizes the multilayer adsorption and pore condensation and type VI describes non-porous adsorbents (e.g., Kr on graphite).

From type II and type IV isotherms, the specific surface area of the adsorbents can be determined by applying the BET theory. It is an extension of the Langmuir theory for the monolayer molecular adsorption, and is applicable to the multilayer adsorption with the following assumptions: (1) gas molecules physically adsorb on a solid in layers infinitely; (2) there is no interaction within the adsorption layer and (3) the Langmuir theory can be applied to each layer. The resulting BET equation, which was derived by Stephen Brunauer, Paul Emmett and Edward Teller,[53] is expressed by:

$$\frac{p}{(p_0 - p)V_a} = \frac{1}{cV_{mon}} + \frac{(c-1)p}{cV_{mon}p_0} \qquad (3.32)$$

Where V_a is the volume of gas adsorbed, V_{mon} the volume of gas adsorbed in a monolayer, p and p_0 are the equilibrium and the saturation pressure of the gas, c is the BET constant which is proportional to the energy of adsorption of the first layer. The BET surface area is determined from the correlation of p/p_0 *vs.* $p/V_a(p_0–p)$ using the pressure range $0.05 < p/p_0 < 0.3$ (due to the linear relationship in this range). This plot is called a *BET plot*.

The BET surface area, S_{BET}, is evaluated by the following equation:

$$S_{BET} = V_{mon}N_a s \qquad (3.33)$$

where N_a is Avogadro's number, and s is the adsorption cross section. For nitrogen s(N_2) is 13.5 Å^2.[54]

The simple BET analysis was developed explicitly for non-microporous (i.e., mesoporous) solids and in the relative pressure range, $0.25 > p/p_0 > 0.05$, which guarantees no capillary condensation in pores. So, the simple BET analysis is not enough for microporous solids. The correct way is to use the comparative plots (i.e., t-plot) which can supply the micropore volume.[55]

The *t-plot method,* applied for a quantitative determination of the micropore volume, is attributed to Lippens and deBoer.[56,57] For a large number of non-porous solids the shape of the N_2 sorption isotherm can be represented with a single curve, by plotting the ratio V_a/A (V_a being the volume of N_2 adsorbed, A the surface area of the sample) as a function of the relative pressure p/p_0. The resulting, so-called *t-curve*, which is in principle a BET type II isotherm, reflects the statistical thickness of the adsorbed N_2 multilayer (t) and can be calculated according to:[57]

$$t = \sqrt{\frac{13{,}99}{-\log\left(\frac{p}{p_0}\right) + 0{,}034}}\ \text{Å} \qquad (3.34)$$

Deviations of the t-plot from the ideal behavior allow the deduction of the nature of pores and to determine the micropore volume. The experimental points of this t-curve were found to give a good agreement with the isotherm equation of Harkins and Jura.[58]

For the multimolecular adsorption, the experimental points should fall onto a straight line and pass through the origin for a non-porous material. The slope (V_a/t) of this line and the corresponding surface area, S = 15.47× (V_a/t), give the specific area of the catalyst in m²/g.[57] For a porous material, the line will have a positive intercept indicating micropores, or deviate from the linearity suggesting a filling of mesopores.

The pore size distribution (PSD) of porous materials is another important characteristic. Horvath and Kawazoe (HK)[59] proposed a very attractive model of instant filling of a slitlike micropore at a definite pressure in the bulk phase. This model was extended to cylindrical and spherical pores. It suggests that the adsorption was described as a sequential filling of micropores from the smallest accessible pores to larger ones as the pressure increases. Such a sequential filling allows each micropore to be either empty or completely filled. To determine the pressure of instant filling, the authors implicitly used the principle of equality of the chemical potential in the bulk phase and that in the adsorbed phase, applying the mean value of potential energy.[60]

3.4 Fundamentals of EXAFS

To understand the activity of metal nanoparticles one should understand the role(s) that their size, shape and extent of the interaction with the support play. However, due to their small nature, they are often difficult to characterize. XAS (X-ray absorption spectroscopy) and, in particular, EXAFS (extended X-ray absorption fine structure) can be employed to study such samples also under in situ conditions.[61]

XAS can provide information about the nanostructure (e.g., coordination numbers, interatomic distances, and oxidation states of absorption atoms). This structural information is averaged over all of the X-ray excited atoms in the entire sample, but since a large percentage of the atoms in nanoparticles are at the interface, the information obtained is sensitive to the bimetallic interfacial structure. Furthermore, analysis by EXAFS can be useful for identifying the occupied sites around specific atoms. Using EXAFS, the interatomic distances, the variations in distances, and the identity and the number of nearest neighbor atoms within the first few coordination shells of the X-ray-excited atoms can be determined.[34]

In 1930's X-ray absorption was being carried out using a continuum source of X-rays, a dispersive spectrometer, and a film detector. The sample absorbs X-rays according to the Beer-Lambert law (eq. 3.15). In these experiments it was found that each absorption line is asymmetric, showing a long tail extending to high photon energies and also some sharp structure to low energy of the sharp low energy absorption edge. The pre-edge structure of the K-edge, corresponding to the removal of a K-shell (1*s*) electron, is due to the electron being promoted to unoccupied orbitals, such as 5*p* or 5*d*. The edge itself represents the onset of the ionization continuum for the removal of a 1*s* electron. It was observed, in some cases of X-ray absorption that there was some fine structure, it is known as extended X-ray absorption fine structure (EXAFS).[62] The main features of this experimental method are: a synchrotron as continuum radiation source; a concave toroidal mirror to focus the radiation; a double-crystal monochromator, acting as diffraction gratings, and two ion chambers, which measure the intensities I and I_0 of the incident beam.

The EXAFS technique is used primarily for investigations of disordered materials and amorphous solids. It can be used for different elements in the same material or for different absorption edges, such as 1*s*, 2*s*, or 2*p*, in the same element.[62]

In detail one can read about this effective technique in the following books: by H. Wende;[63] D. Ahlers;[64] edited by Q. Jr. Lawrence;[65] and by J. M. Hollas.[62]

4 Experimental details and sample characterization

This chapter describes the experimental work details: how the bimetallic and monometallic samples were prepared, the operation specialties of IR, EPR spectroscopes and nitrogen sorption analysis.

4.1 Sample preparation

The commercially available NaY zeolite (Zeocat, Z6-01-01 from CU Chemie Uetikon, with a Si/Al ratio of 2.31) was heated in air with a rate of 1 K min^{-1} and calcined at 773 K for 14 h to burn off impurities. The unit cell composition of this zeolite is $Na_{58}[(AlO_2)_{58}(SiO_2)_{134}]$.

All of the samples under investigation were prepared by the ion exchange in a flask containing 1 g of the pre-treated zeolite with ***V*** ml of an aqueous metal salt solution with the molarity ***X*** mM, which was stirred at the temperature T_1 for the time t_1. The exchanged zeolite was filtered, washed with bidistilled water to remove Cl^-/ NO_3^- ions and dried in an oven/ in air at T_2 for t_2.

The experimental parameters for the *monometallic samples* are presented in Table 4.1:

Table 4.1: Parameters of ion exchange for the monometallic samples.

	Pt	***Pd***	***Ag***
T_1, *K*	*343*	*298*	*298*
t_1, *hours*	*48*	*20*	*12*
salt	$[Pt(NH_3)_4]Cl_2$ *(Sigma-Aldrich Co., 99.99%)*	$[Pd(NH_3)_4](NO_3)_2$ *(Sigma-Aldrich Co., 99.99%)*	$AgNO_3$ *(ChemPur GmbH, 99.998%)*
***V**, ml*	*100*	*200*	*200*
***X**, mmol*	*3*	*1*	*0.1*
T_2, *K*	*343*	*298*	*298*
t_2, *hours*	*48*	*24*	*24*

The experimental technique for the plain Pt sample was taken from the work of Akdogan *et al*.[66] and for the plain Pd sample from the work of Sheu *et al*.[67] For the purpose of this work,

silver was at first added to a plain Pd sample to obtain a bimetallic alloy; only after that the monometallic samples were synthesized to compare their properties with the bimetallic ones. That is why the technique for the plain Ag sample is almost the same as for the plain Pd sample. Smaller time for the ion-exchange is caused by a smaller concentration of the metal in a solution. The samples, containing Ag, were protected from the light due to their photo/ light sensitivity.

Binary PdAg samples were prepared in two steps: first by the exchanging with 200 ml 1 mM $[Pd(NH_3)_4](NO_3)_2$ solution. After 20 hours at 298 K 200 ml $AgNO_3$ (0.1 mM or 1 mM water solution) was added and stirred for another 12 hours (drying parameters are the same as for the monometallic Ag and Pd samples). In this way, two samples with the same loading of Pd and different loading of Ag were synthesized. Another bimetallic PdAg with enhanced loading of Pd was prepared by the same "two step" way with 1 mM $AgNO_3$ and 5 mM $[Pd(NH_3)_4](NO_3)_2$ water solutions.

The synthesis of the binary PtAg sample was complicated by the possibility of AgCl formation. To avoid this reaction, the Pt-exchanged zeolite (by the "plain Pt" method) was thoroughly washed with NH_4OH to remove the Cl anions. Then, the Ag salt solution was added ("plain Ag" method, but with 1 mM solution).

The resulting loadings of metals in a zeolite were determined by the atomic absorption spectroscopy (the measurements were performed by Ms. H. Fingerle from the Institute of Technical Chemistry, University of Stuttgart) and are presented in Table 4.2. The corresponding loadings per unit cell and the concomitant indication of the samples under investigation are also given.

Table 4.2: Metal loadings.

	Pt	***PtAg***	***Ag***	***PdAg(1)***	***PdAg(2)***	***PdAg(3)***	***Pd***
wt.%	*4.5*	*5.03/1.96*	*0.21*	*1.73/0.34*	*1.85/2.42*	*9.15/2.46*	*1.81*
per u. c.	$Pt_{3.81}$	$Pt_{4.24}Ag_{2.98}$	$Ag_{0.31}$	$Pd_{2.66}Ag_{0.52}$	$Pd_{2.80}Ag_{3.61}$	$Pd_{14.67}Ag_{3.88}$	$Pd_{2.70}$

According to the literature, the ion exchange capacity of a typical zeolite Y is lower than that of, for example, zeolite X due to the lower framework charge. Many exchange reactions do not go to the completion at normal temperatures. Some of the exchanged cations are too large to penetrate the small β-cages. For univalent ions the level of the exchange is usually 35 of

the 51 univalent ions (in case of $Na_{51}[(AlO_2)_{51}(SiO_2)_{141}]$, dry) originally present in the unit cell. The difference, 16 univalent ions, corresponds to the 16 sites I located in the double-six rings (D6R, see Figure 2.1).[27] Ag is small enough to occupy the β-cages.

None of the divalent or trivalent ions, studied in zeolite Y, is completely exchanged at room temperature, and the maximum degree of exchange appears to be 0.68.[27] With zeolite Y, the interaction of cations with the lattice is one of the most important factors in the exchange. Calcination and reduction temperatures are also very important. For instance, Pt, exchanged by the $Pt(NH_3)_4^{2+}$ complex, can be deposited in small sodalite cages, in supercages and on the external surface of the NaY, which depends on the treating temperatures.[28]

The predicted (100% of an exchange) and obtained metal loading per gram of NaY zeolite are presented in Table 4.3.

Table 4.3: Metal loading in mg/ 1g NaY.

	Pt	***PtAg***	***Ag***	***PdAg(1)***	***PdAg(2)***	***PdAg(3)***	***Pd***
calculated	*58.50*	*58.50/21.28*	*2.16*	*21.28/2.16*	*21.28/21.6*	*106.4/21.6*	*21.28*
measured	*45.02*	*50.34/19.58*	*2.06*	*17.34/3.35*	*18.54/24.21*	*91.49/24.56*	*18.01*

Univalent Ag, as expected, exhibits the highest exchange extent. In some cases the measured amount of silver in a zeolite was even higher than the predicted one, which could be caused by errors during the sample preparation and/or atomic absorption spectroscopy measurements. If one compares Pd and Pt, Pd exchanges slightly better.

Exchanged $Pt_{3.81}$ and $Pt_{4.24}Ag_{2.98}$ samples were calcined in flowing O_2 (20 ml $min^{-1}g^{-1}$, (Westfalen AG in Germany, 99.999%) using a ramping rate of 0.5 K min^{-1} from room temperature to $\boldsymbol{T_c}$ = 573 K, and then holding the temperature for the $\boldsymbol{t_c}$ = 300 minutes; for $Pd_{2.70}$, $Pd_{2.66}Ag_{0.52}$, $Pd_{2.80}Ag_{3.61}$, $Ag_{0.31}$ $\boldsymbol{T_c}$ was equal to 523 K, and $\boldsymbol{t_c}$ to 120 minutes. For $Pd_{14.67}Ag_{3.88}$ the $\boldsymbol{T_c}$ of 773 K was used.

The wafers for IR measurements were prepared from the calcined samples.

4.2 IR measurements

Small amounts of the catalyst powder were pressed into 1 cm diameter wafers of 20–30 mg cm^{-2}. The wafers were transferred to the IR cell equipped with KBr windows and recalcined

in O_2 for 10 minutes. O_2 was then replaced by N_2 (Westfalen AG, 99.999%). The absence of water was verified by the absence of bands around 1650 and 3650 cm^{-1}.

The wafer was heated up under hydrogen (Westfalen AG, 99.999%) to 473 K at a rate of 6 K min^{-1}, and then held for 20 minutes. The gas was then removed. After reduction, the FTIR spectra showed a strong band near 3650 cm^{-1}, confirming the formation of Si(OH)Al acidic bridging hydroxyl groups.[67]

Flowing CO (Westfalen AG, 99.999%) was introduced at 298 K. Background spectra were recorded with a reduced wafer. The spectra of adsorbed CO were then obtained by subtracting the background.

FTIR spectra were recorded in the 4000–400 cm^{-1} range on a Nicolet Magna-IR 560 spectrometer at a spectral resolution of 2 cm^{-1}, accumulating 256 scans.

The adsorption bands were fitted using Lorenzian lines.

4.3 EPR measurements

Continuous wave electron paramagnetic resonance spectra were recorded with a X-band Bruker EMX spectrometer with a microwave frequency of about 9.466 GHz at the temperature 4 K, using an Oxford temperature controller. For cooling the samples a helium Oxford EPR-900 continuous-flow cryostat was used.

CW-EPR records derivatives of absorption spectra by using magnetic field modulation of 100 kHz, and this particular method enjoys the advantages of narrowband detection at the modulation frequency and of better resolution of the derivative as compared to the absorption lineshape. The receiver gain varied from 1×10^4 to 1×10^5 depending upon the signal-to-noise ratio.

The spin concentration of a sample was calibrated against the standard sample (ultramarine blue diluted by KCl) via double integration of the derivate signal. The general formula for the calculating the spin concentration of a sample using a standard sample of known concentration is given by eq. 3.30.

EPR spectra simulations were carried out using the EasySpin computational simulation package, based on MATLAB numerical functions.

The spectra were recorded for the samples in different states: calcined, reduced, with adsorbed CO and after CO desorption.

4.4 Nitrogen physisorption details

Nitrogen sorption (adsorption-desorption) measurements were performed at 77 K on a Micromeritics ASAP 2010 volumetric adsorption analyzer (Neuss, Germany). The mesopore surface area was estimated using the Brunauer-Emmett-Teller (BET) method,[53,68] the micropore surface area and the volume of micropores were computed by the t-plot method,[56,57] while the pore size and their distribution was computed by the Horvath-Kawazoe method.[59] The pore volume was determined from the amount of N_2 adsorbed at a relative pressure of 0.99. Before the experiments, 50–100 mg of a calcined (the calcination parameters are given in section 4.1) sample were degassed at 373 K for 8 h in the degassing port of the adsorption apparatus. The analyses were done using the DataMaster program and the DFTplus module from Micromeritics.

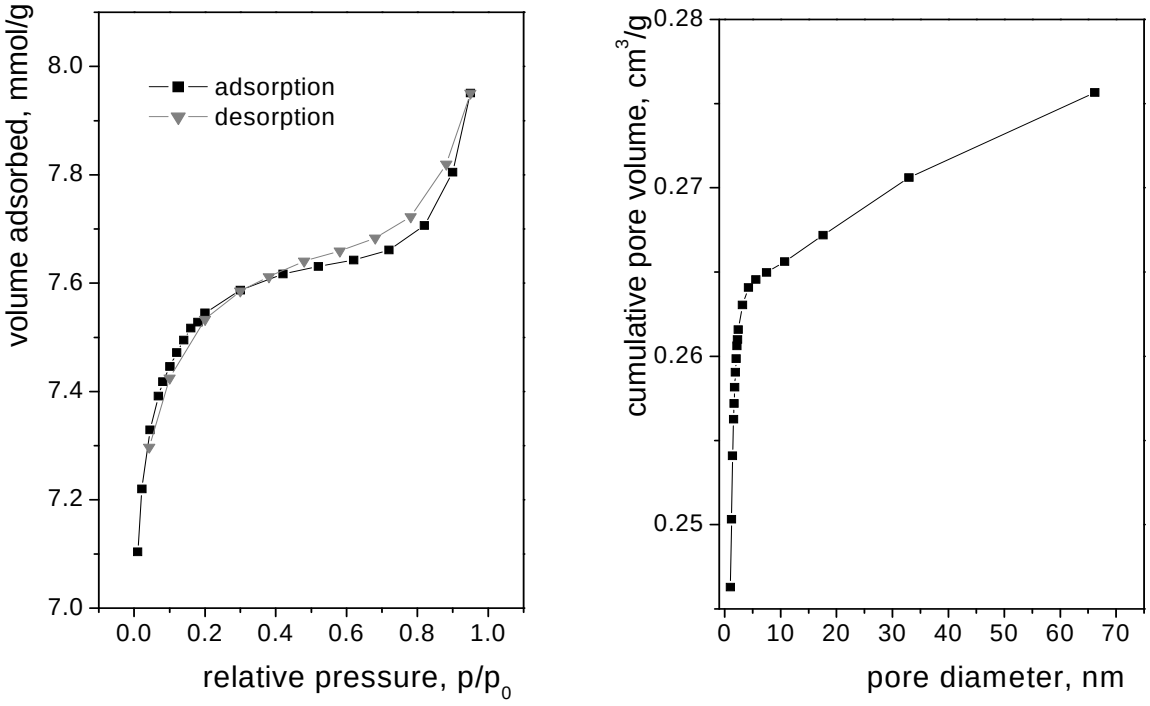

Figure 4.1: BET isotherm (left) and HK pore size distribution (right) of calcined $Pd_{2.66}Ag_{0.52}$.

According to the literature, the NaY zeolite has BET surface area of 281–735.4 m^2/g, the most probable pore diameter about 0.8–0.9 nm and pore volume of 0.19–0.42 cm^3/g.[69,70] (the data vary depending on Si/Al ratio). This microporous solid exhibits a Type I isotherm that reaches a plateau, indicative of saturating adsorption, at very low relative pressure. As an

example, the isotherm and the pore–distribution for the $Pd_{2.66}Ag_{0.52}$ sample are shown in Figure 4.1.

One can see that although the NaY zeolite is a microporous solid, there is still some volume of large mesopores (Figure 4.1, right), which also could appear during the heat treatment under high temperatures, or it can be the space between the crystallites. Due to the presence of mesopores a small hysteresis in the sorption curves can be observed (Figure 4.1, left). At low relative pressure $p/p_0 < 0.4$ the adsorption in micropores is the prevailing process. At this pressure adsorption/desorption curves are almost identical. At higher pressure $p/p_0 > 0.4$ the adsorption in mesopores proceeds until condensation takes place. The desorption occurs via evaporation of the nitrogen from mesopores and usually takes place at a pressure lower than that of capillary condensation, resulting in hysteresis. A similar behavior was observed for all samples under investigation.

The samples physical properties are summarized in Table 4.4.

Table 4.4: Physical properties of the calcined samples determined from the nitrogen adsorption analysis.

Sample	BET surface area, m^2/g	Micropore area, m^2/g	Micropore volume, cm^3/g	Median pore diameter, nm
not exchanged NaY	636 ± 11	607	0.244	1.0260
$Ag_{0.31}$	593 ± 13	549	0.237	1.0333
$Pd_{2.70}$	564 ± 11	518	0.230	1.0423
$Pd_{2.66}Ag_{0.52}$	592 ± 11	540	0.239	1.0219
$Pd_{2.80}Ag_{3.61}$	516 ± 10	490	0.217	1.0403
$Pd_{14.67}Ag_{3.88}$	415 ± 8	390	0.173	1.0423
$Pt_{3.81}$	546 ± 10	502	0.222	1.0294
$Pt_{4.24}Ag_{2.98}$	423 ± 8	383	0.169	1.0151

According to these data, surface and micropore properties depend on the amount of the exchanged metal. BET surface area, micropore area and micropore volume values decrease with increasing metal loading in NaY. Small fluctuations (an increase while going from $Pd_{2.70}$ to $Pd_{2.66}Ag_{0.52}$) can be caused by an inaccuracy of the method. The median pore diameter

does not seem to be dependent on the amount of the metal. These pores should be the α-cages (or supercages) of the NaY zeolite.

5 Experimental results and discussion for PdAg bimetallic nanoalloys

The goal of this study is the understanding of the alloying mechanism and the corresponding effects of alloying. First, the spectra of the unexchanged NaY zeolite should be compared with the spectra of monometallic samples. Then it will be possible to assign the signals to certain species before the analysis of the spectra of bimetallic samples can be started.

5.1 FTIR spectra of adsorbed CO

CO is used as a probe molecule for the recognition of the electronic properties and the surface composition of the binary metal clusters. In the non-alloyed case one would expect the spectra of the bimetallic samples to be superpositions of those of the monometallic ones, possibly accompanied with small shifts if electronic effects are transmitted through the zeolite lattice. Thus, the main criterion for alloying will be that there are major spectral differences compared with the monometallic samples.

Some of the results and spectra of this chapter were published.[71]

5.1.1 Adsorption of CO on NaY

The Na^+ cations of the NaY zeolite occupy SI, SI' and SII sites and only negligible numbers of them are in SIII positions (see Figure 2.2). The SI and SI' sites are located in the hexagonal prisms and the sodalite cages, respectively, where they are not accessible at low temperature even for small molecules such as CO.[72] The only accessible Na^+ cations are in SII positions, in six-ring windows, where they are coordinated to three framework oxygen atoms to form a regular triangle. This structure allows the principal possibility of simultaneous coordination of more than one CO molecule to a cation; at 85 K one may also expect the formation of Na^+ dicarbonyls. The interaction of CO with basic metal cations is weak and has essentially an electrostatic character. For this reason, the adsorption of CO on Na^+ has to be studied at low temperatures.[72]

Figures 5.1 and 5.2 present the IR spectra of adsorbed CO for NaY at room and low temperatures. At room temperature, one can observe IR band progressions around 2166 and 2124 cm^{-1} assigned to the R and P rotational–vibrational branches of gaseous CO (Figure 5.1, spectrum a; Figure 3.1). The gas-phase bands can be easily removed by evacuation (spectra b

and c). Weak bands at 2003, 2033, and 2073 cm^{-1} characterize CO adsorption on unspecified zeolite centers. There is no CO absorption on the Na^+ cations of the NaY zeolite at 298 K.

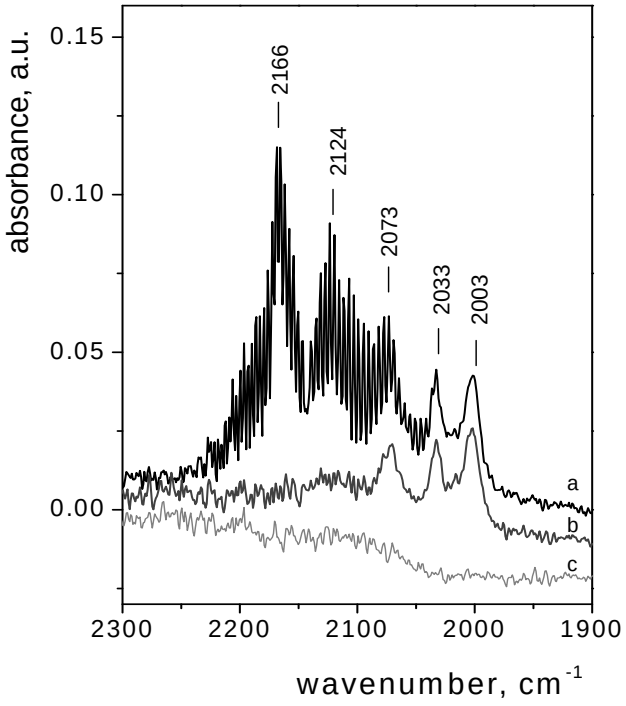

Figure 5.1: FTIR spectra recorded after CO adsorption (500 mbar) at 298 K on NaY, followed by evacuation. p (CO) = 50 mbar (a), 2 mbar (b), under vacuum (c).[71]

At 85 K (Figure 5.2) one observes a very strong and narrow band at 2173 cm^{-1}. It is, in a general consensus, assigned to the fundamental CO stretching mode of the probe forming Lewis-type adducts with Na^+, and results in the formation of $Na^+(CO)$ carbonyls through a C-atom with Na^+ in SII positions of the zeolite.[72-74] In addition, a weak band appears at 2123 cm^{-1}. It can be assigned to the ^{13}CO stretching mode of $Na^+(^{13}CO)$; its isotopic shift coincides with the theoretical expectation.[72] The intensity of the CO band at 2173 cm^{-1} is so high that instrumental limitations do not allow the exact determination of the maximum, even under vacuum conditions. Only by increasing the temperature does the intensity of the band decrease (spectra a–d). The weak bands, assigned above to CO adsorption on zeolite centers, are not visible at the scale of Figure 5.2 but they remain unchanged (see inset in Figure 5.2).

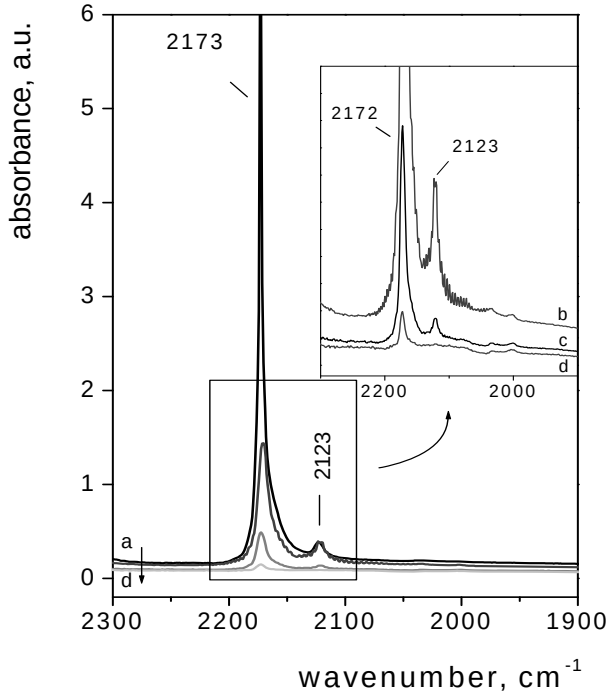

Figure 5.2: FTIR spectra recorded after CO adsorption (100 mbar) at 85 K on NaY, followed by evacuation at 85 K (a), 173 K (b), 223 K (c), and 273 K (d).[71]

5.1.2 Adsorption of CO on Ag

FTIR Spectra of CO adsorbed on Ag-exchanged NaY/ plain NaY at room and low temperatures are presented in Figures 5.3 and 5.4, respectively.

For the $Ag_{0.31}$ sample at 298 K one observes a spectrum with a new broad band centered at 2185 cm^{-1} in addition to the bands observed for plain NaY. At 85 K (Figure 5.4) one can distinguish a new band for $Ag_{0.31}$ at approximately 2188 cm^{-1} with a shoulder at 2197 cm^{-1}. This stretching frequency belongs, according to the literature, to $Ag^{+}CO$,[45,75-77] the only feature that relates to CO adsorption on silver. It is blue-shifted from 2143 cm^{-1} (free gas phase value) by 45 cm^{-1}. A shoulder at 2197 cm^{-1}, which comes from the small peak at approximately 2195 cm^{-1}, possibly belongs to some $Ag^{\delta+}CO$ species. It is in line with the work of Lynn *et al.*,[75] who also observed a surprisingly high stretching frequency (2204 cm^{-1}) for the Ag–CO complex.

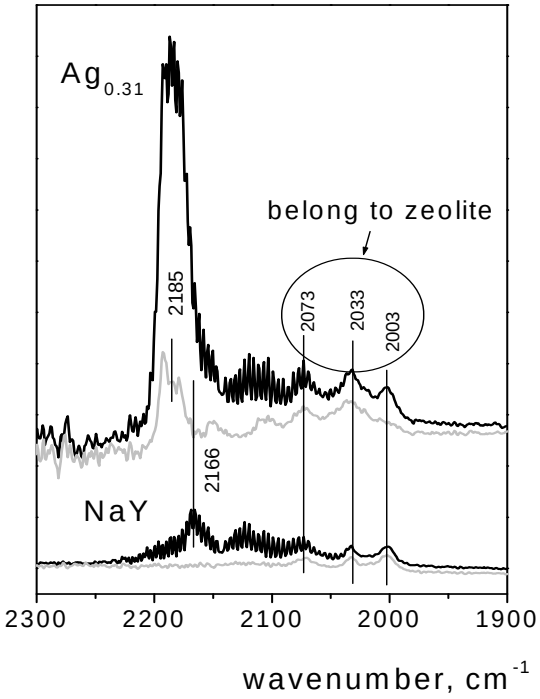

Figure 5.3: FTIR spectra recorded after CO adsorption (500 mbar) at 298 K on NaY and $Ag_{0.31}$, followed by evacuation. p (CO) = 90 mbar (black line), 1 mbar (grey line).

Generally, CO, adsorbed on a metal, exhibits stretching frequencies that are lower than the 2143 cm^{-1} frequency of free CO. This reduction in CO stretching frequency is usually taken as evidence for M → CO backbonding: the donation of electron density from the metal *n*d orbitals into the antibonding 2π orbital of CO (Figure 3.4). This backbonding weakens the C–O bond and lowers the stretching frequency. But there are also some "nonclassical" carbonyl complexes, and d^{10} Ag(I) complexes with linear carbonyl ligands are at one extreme of nonclassical carbonyls, in which the CO stretching frequency is close to or even higher than that in free CO, an indication that no significant Ag → CO backbonding occurs even though there is a surfeit of d-electron density available. These systems exhibit less M → CO backbonding into the C–O antibonding 2π* orbital, but significant OC → M σ-donation from the CO 5σ orbital resulting in the high stretching frequencies.[75]

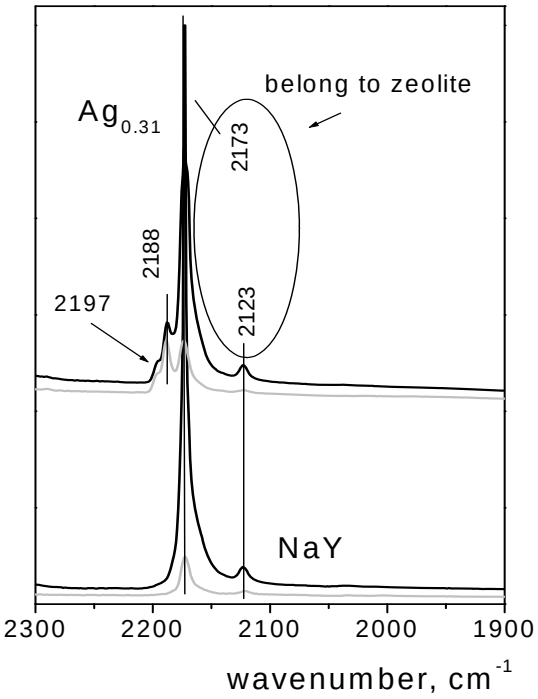

Figure 5.4: FTIR spectra recorded after CO adsorption (100 mbar) at 85 K on NaY and $Ag_{0.31}$, followed by evacuation at 85 K for 30 min (black line) and 1 hour (grey line).

After H_2 reduction, and since CO is also a reducing agent, one should expect the presence of peaks which belong to Ag^0CO species, but, according to the literature, adsorption of CO on Ag^0 can form a very weak bond only at low temperatures, and this IR band was rarely observed.[20,45] Another workgroup reported that CO does not interact with Ag^0 atoms under the present conditions at all.[76]

It is known, that in low concentrations Ag^+ has a strong affinity for site SI in the hexagonal prisms which join two adjacent sodalite units. The next preferred site is SI'.[78] Some authors also reported the presence of Ag^+ in NaY zeolite in the SII sites.[79,80] Since SI and SI' positions are not accessible for CO, the IR signals at 2188 and 2197 cm^{-1} belong most probably to Ag^+ in the SII sites. Although Ag^+-exchanged zeolites are intensively studied, some debates still exist on the nature and location of the silver cations inside the cavities of zeolites.[45] The cation migration from site to site also cannot be completely excluded.[80]

5.1.3 Adsorption of CO on Pd

The characterization of Pd nanoparticles with FTIR studies of adsorbed CO was already discussed in numerous works.[81-85] Some of them are also dedicated to Pd clusters entrapped in NaY zeolite supercages.[11,67] Due to the extensive experimental database the observed infrared frequencies can be easily correlated with the corresponding palladium carbonyls. CO stretching frequencies for Pd in a Y zeolite are also relatively high, because the metal in interaction with acid sites is usually electron deficient.[86]

For the $Pd_{2.70}$ sample it was observed a spectrum (Figures 5.5) which is akin to the one obtained earlier by Sheu *et al.*[67] for $Pd_{13}(CO)_x$ clusters in NaY zeolite, suggesting that a very similar or identical structure was synthesized. The present spectrum shows CO ligands in terminal, doubly and triply bridging positions.

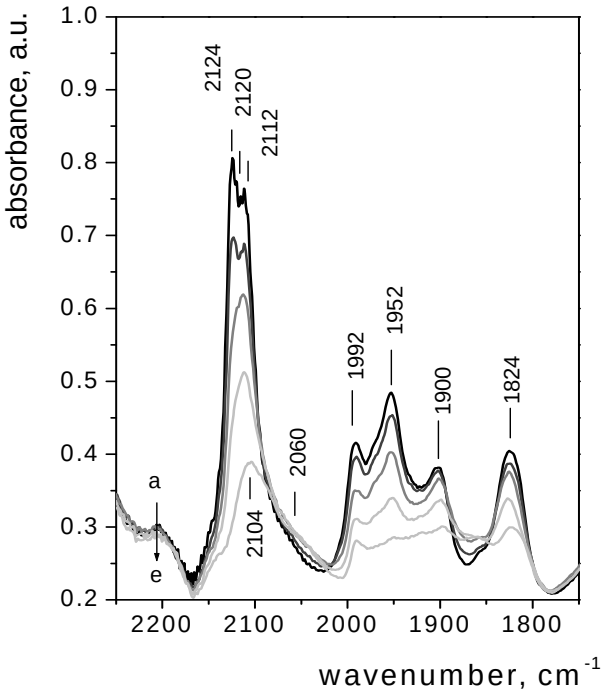

Figure 5.5: FTIR spectra of adsorbed CO (500 mbar) at 298 K on $Pd_{2.70}$, recorded during the desorption at the equilibrium pressure of CO (a) 30 mbar, (b) 6 mbar, (c) 2 mbar, (d) 0.5 mbar, followed by evacuation for 1 hour (e).

Four bands could be assigned to multiply bonded CO ligands, namely, to CO adsorbed on Pd in two-fold (three overlapping bands at 1992, 1952, and 1900 cm^{-1}) and three-fold (the band at 1824 cm^{-1}) binding sites. In the region of terminal CO ligands, the broad strong peak

centered at approximately 2118 cm^{-1} can be separated into two peaks which are assigned to $Pd^{+}CO$ (2124 cm^{-1}) and $Pd^{0}CO$ (2112 cm^{-1}) complexes. There is also a possibility of the presence of $Pd^{\delta+}CO$ species, with the $Pd^{\delta+}$ presumably occupying SII sites, while the CO ligand may be coordinated to it through the 6R ring (at 2120 cm^{-1}).[67]

One can notice the shift of the broad band, centered at approximately 2118 cm^{-1} at high CO coverage to 2104 cm^{-1} at lower CO coverage. In addition, a weak band develops at 2060 cm^{-1} during CO desorption. These observations are in full agreement with observations of Sheu *et al.,*[67] who distinguished two states of the cluster – fully carbonylated with CO and partially decarbonylated. The cluster, fully carbonylated with CO, is likely to be in the cage center, after decarbonylation it shifts towards the cage wall.[67]

During the experimental work it was noticed that the monometallic Pd samples were not stable and the clusters often appeared to disintegrate at higher CO pressure during CO adsorption. In Figure 5.6 one can follow the changes in the IR spectra during the possible disintegration of the cluster.

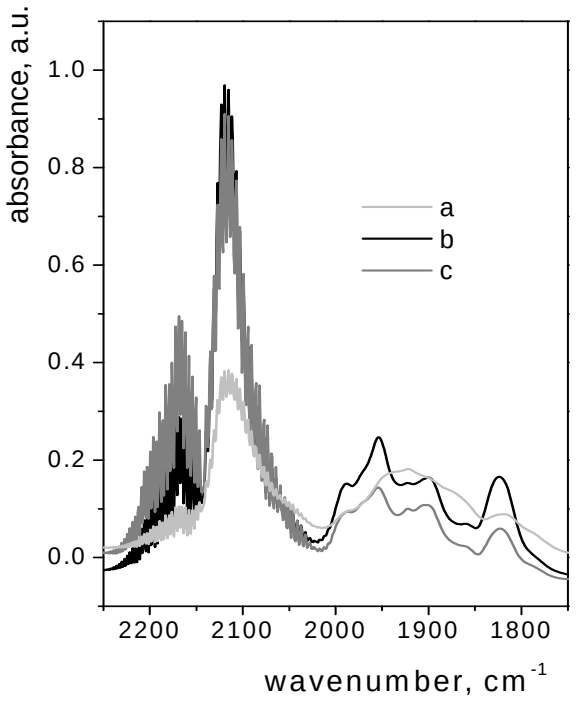

Figure 5.6: FTIR spectra of adsorbed CO on $Pd_{2.70}$, recorded during the adsorption at 298 K. The equilibrium pressure of CO is (a) 60 mbar, (b) 200 mbar, (c) 300 mbar.

Adsorbing CO, first a broad peak can be observed in the bridge region at low CO coverage (line a), with time and increased CO pressure (line b) one can distinguish four peaks, characteristic for the Pd cluster. Newly prepared samples were usually stable at this and higher CO pressure, but for the aged samples it was observed a sudden reduction of intensity for the peaks in the bridge region with increased CO pressure (line c). In this spectrum one can see a rise of the peak at 2166 cm^{-1} (R-branch of rotational–vibrational spectrum), but the peaks in the bridge region diminish. With time they disappear completely. After one night under 100–200 mbar of CO, no peaks could be observed in the bridge region. The reproducing the IR spectra for a some months old $Pd_{2.70}$ sample did not succeed even at low CO pressure.

Akdogan *et al.*[87] described a similar reconstruction for Pt_{13} clusters breaking up into $Pt_2(CO)_m$, which also led to changes in IR spectra in the bridge region (it will be discussed in section 6.1.2 in detail).

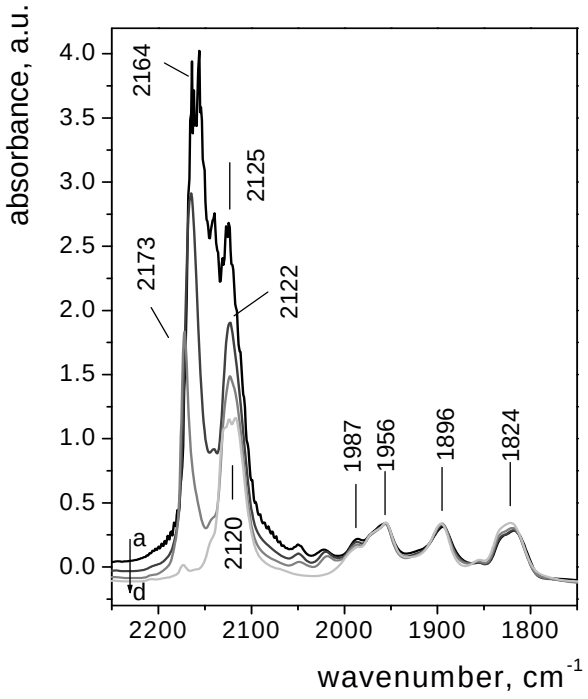

Figure 5.7: FTIR spectra of adsorbed CO (100 mbar) at 85 K on $Pd_{2.70}$, recorded during the desorption at the equilibrium pressure of CO (a) 60 mbar, (b) 1.5 mbar, followed by evacuation for 20 minutes (c) and 2 hours (d).

CO was also adsorbed on the $Pd_{2.70}$ sample at 85 K (Figure 5.7), but there are no essential differences between the spectra at room and low temperatures concerning PdCO species: one observes insignificant shifts (max. ±5 cm^{-1}) of the major bands in the bridge region: the peak at 1992 cm^{-1} shifts to 1987 cm^{-1}, at 1952 to 1956 cm^{-1}, at 1900 to 1896 cm^{-1}. Due to these shifts the bands in the bridge region are less overlapping. The assignment of the peaks remains the same.

As for the linear region – there is an overlapping of the peaks from CO adsorbed on Na and Pd cations. At higher CO coverage (Figure 5.7, line a), the linear $Na^{+}CO$ species (band at 2173 cm^{-1}) are converted into other types, which reveal at the lower wavenumber (2164 cm^{-1}). It can be explained by the formation of dicarbonyls, and the peak at 2164 cm^{-1} is assigned to $Na^{+}(CO)_2$ species.[72] The broad peak centered at 2120 cm^{-1} (line d) consists of three overlapping peaks – the one from $Na^{+}(^{13}CO)$ (2123 cm^{-1}) and another two from $Pd^{+}CO$ (2124 cm^{-1}) and $Pd^{0}CO$ (2112 cm^{-1}).

5.1.4 Adsorption of CO on bimetallic samples

Three bimetallic samples were prepared – two with almost the same loading of palladium and different loadings of silver: $Pd_{2.66}Ag_{0.52}$ and $Pd_{2.80}Ag_{3.61}$; and one with increased loading of palladium – $Pd_{14.67}Ag_{3.88}$. The IR spectra of adsorbed CO for the first two samples were quite identical. In Figure 5.8 one can follow the changes in the IR spectra by comparing them with the spectra for the monometallic Ag and Pd samples.

5.1.4.1 Assignment of the bands

The bands observed for the binary samples $Pd_{2.80}Ag_{3.61}$ and $Pd_{2.66}Ag_{0.52}$ (spectra b and c in Figure 5.8) are, in principle, similar to those of $Pd_{2.70}$ (spectrum d). Adding silver mostly seems to shift the bands in the bridge-bonded and linear regions relative to those of the $Pd_{2.70}$ sample. Four bands at 1950, 1881, 1857, and 1789 cm^{-1} can be still assigned to multiply bonded CO on Pd. Clearly, the shifts are due to the effect of alloying, which will be discussed below. One further distinguishes two overlapping bands in the linear region: at 2123 cm^{-1}, assigned above to $Pd^{+}CO$, and at 2080 cm^{-1}, which must belong to terminally bonded CO in the alloy.

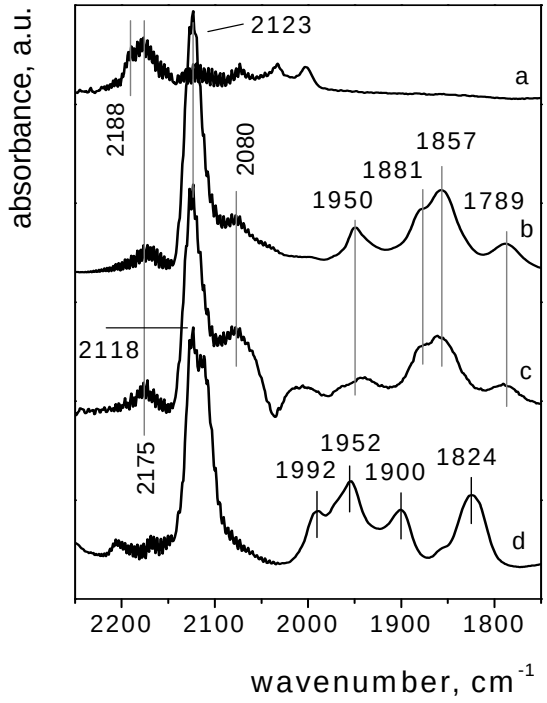

Figure 5.8: FTIR spectra recorded after CO adsorption (500 mbar) at 298 K on $Ag_{0.31}$ (a), $Pd_{2.80}Ag_{3.61}$ (b), $Pd_{2.66}Ag_{0.52}$ (c) and $Pd_{2.70}$ (d). The equilibrium pressure of CO is 100 mbar.[71]

The component at 2175 cm^{-1} (Figure 5.8, traces a–c) is assigned to CO adsorbed on Na^+ ions (weak interaction at room temperature). There is no signal from Ag^+CO at 2188 cm^{-1} (Figure 5.8, line a) in the spectra of the bimetallic samples at 298 K. There is a possibility that in the presence of Pd, Ag^+ could be more easily reduced to Ag^0, which does not adsorb CO and is not visible in the IR spectra. A similar phenomenon was already observed by Michaelis *et al.*[17] who reported that Ag^+ ions were reduced in the absence of palladium with an induction period of several minutes, and in the presence of Pd practically instantaneously.

FTIR spectra obtained at 85 K are presented in Figure 5.9A (linear region) and 5.9B (bridge region). The strong band at 2173 cm^{-1} in the linear region belongs to ^{12}CO adsorbed on Na^+ ions. The one at 2123 cm^{-1} corresponding to $Na^+(^{13}CO)$ species is clear for $Ag_{0.31}$ (Figure 5.9A, spectrum a), but for other samples it overlaps with the band near 2127 cm^{-1}, belonging to Pd^+CO (Figure 5.9A, spectrums b, c, d). For the samples containing silver one also observes the small peak at 2188 cm^{-1} with a shoulder at 2197 cm^{-1} characteristic for Ag^+CO and $Ag^{\delta+}CO$ (Figure 5.9A, lines a–c), overlapping with the peak at 2173 cm^{-1}.

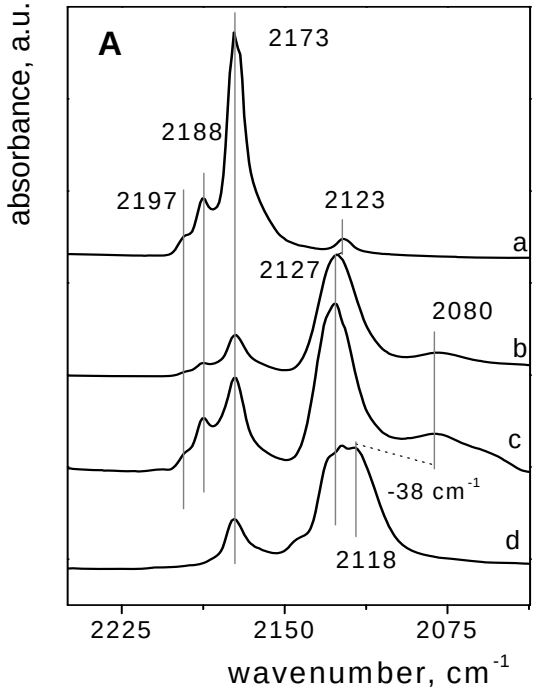

Figure 5.9A: FTIR spectra recorded after CO adsorption (100 mbar) at 85 K, followed by evacuation for 30 minutes on $Ag_{0.31}$ (a), $Pd_{2.80}Ag_{3.61}$ (b), $Pd_{2.66}Ag_{0.52}$ (c) and $Pd_{2.70}$ (d) in the linear region.[71]

Since the 2188 cm^{-1} band is important for the determination of silver species, the present low temperature spectra were recorded after 30 minutes evacuation where the peak at 2173 cm^{-1} is less intense. The amount of adsorbed and partly desorbed CO differs for each sample and the spectra recorded at 85 K serve only for a qualitative analysis.

5.1.4.2 Discussion of red shifts in the bridge region

In comparison with the monometallic Pd sample, the IR spectra of the bimetallic $Pd_{2.66}Ag_{0.52}$ and $Pd_{2.80}Ag_{3.61}$ samples at 85 K (Figure 5.9B, lines d, c, and b) show distinct changes in the bridge-bonded region. Although the overall appearance of this region is the same, there is a red shift of −38 cm^{-1} relative to the peaks of $Pd_{2.70}$ for three of the four bands, for example, the band in the triply-bonded region at 1824 cm^{-1} shifts to 1786 cm^{-1}. At the same time, its relative intensity reduces. This may be a geometry effect of alloying because the number of adjacent Pd surface sites which are necessary for multiply coordinated CO are diluted by Ag atoms. Such phenomena were also described in several works devoted to the investigation of Pd-based bimetallic alloys. For instance, Abbott *et al.*[40] reported, that adding Au to Pd alloy suppresses bonding in bridge geometries and leads to a substantial increase in the intensity of

the CO atop species; Khan *et al.*[21] discussed an effect of Ag on Pd in the blocking of CO adsorption on multiply coordinated sites and the increase in linearly-bonded CO on the particles; and Huang *et al.*[4] reported the complete disappearance of bridge-bonded CO on PdAg alloy, due to isolation of Pd atoms by Ag atoms.

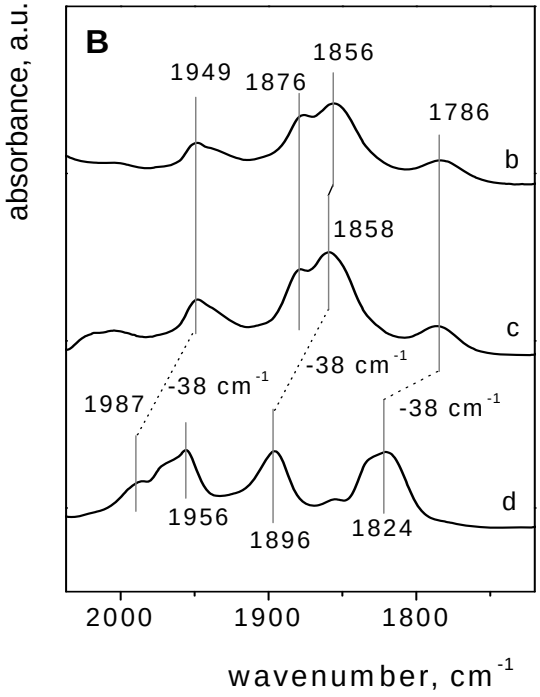

Figure 5.9B: FTIR spectra recorded after CO adsorption (100 mbar) at 85 K, followed by evacuation for 30 minutes on $Ag_{0.31}$ (a), $Pd_{2.80}Ag_{3.61}$ (b), $Pd_{2.66}Ag_{0.52}$ (c) and $Pd_{2.70}$ (d) in the bridge-bonded region.[71]

A peak at 1896 cm^{-1} (Pd_2CO) for $Pd_{2.70}$ shifts to 1858 cm^{-1} ($\Delta\tilde{\upsilon}$ = – 38 cm^{-1}) in the case of the bimetallic samples, and this peak overlaps with another one, leading to a shoulder at 1876 cm^{-1} (Figure 5.9B). In contrast, two overlapping bands at 1987 and 1956 cm^{-1} for $Pd_{2.70}$, also assigned to a Pd_2CO stretching frequency, merge to one peak at 1949 cm^{-1} for the bimetallic sample (1987 – 1949 = 38 cm^{-1}). In general, it can be stated that the region of bridge-bonded CO gets a relatively strong red-shift by adding Ag to the Pd sample. These shifts to lower wavenumbers reveal a weakening of the C–O bond in comparison with the plain Pd sample. The presence of Ag atoms around the Pd atoms could lead to an increasing electron density on Pd by electron transfer from Ag (electronic effect of alloying), resulting in a stronger M

→ 2π backdonation from Pd to the carbonyl C atom. It would possibly lead to a strengthening of the Pd–CO bond and a subsequent weakening of the C–O bond (Figure 5.10).

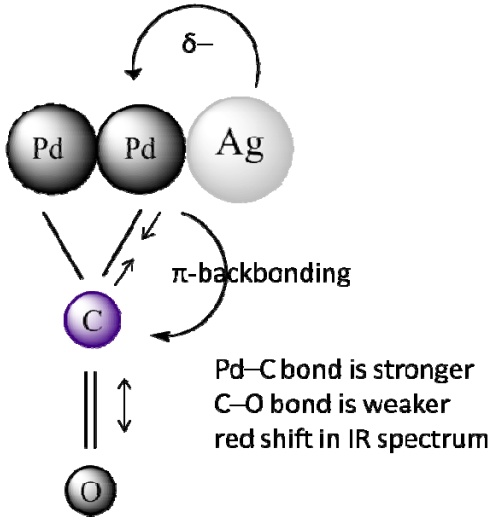

Figure 5.10: Schematic view of an electron effect of alloying against the CO stretching frequency (CO is bonded on Pd in bridge mode).

5.1.4.3 Changes between bimetallic samples

While there is a significant change between the monometallic $Pd_{2.70}$ and the bimetallic $Pd_{2.66}Ag_{0.52}$ sample, in particular, in the bridge-bonded region (Figure 5.9B, spectra d and c), there are quite unexpectedly no significant changes when more silver is added ($Pd_{2.80}Ag_{3.61}$, spectrum b).

Relying on the IR spectra alone, it is hard to say precisely whether the CO molecules adsorb in the bridge mode both on Ag and Pd atoms or whether these bonds are to two Pd atoms that are surrounded by Ag atoms. However, since the spectra for two samples which differ in Ag loading by a factor of 7 are quite identical, it can be concluded that CO is likely bridge-bonded on the same metal; that is, carbon monoxide molecules adsorb preferentially on Pd atoms. This assumption is in line with the work by Heinrichs *et al.*[15] on SiO_2-supported PdAg alloy and by Huang *et al.*[4] on Na^+-β-zeolite-supported PdAg catalysts, reporting that CO molecules form chemical bonds with Pd atoms only.

The identical value for the red shifts of both Pd_2CO and Pd_3CO bands in the bimetallic samples indicates the same effect of the presence of Ag and suggests a well mixed alloy. The fact that this value is also equal for both bimetallic samples (i.e., independent of the Ag loading, though one should expect further red shifts or any other differences in the spectra

with higher Ag loading), can be discussed from two points of view. The first possible explanation: both binary samples may actually contain an equal amount of alloyed Pd and Ag atoms. The excess Ag atoms are isolated and can occupy the cationic sites in the sodalite cages or the hexagonal prisms of the NaY zeolite. The second possibility consists of a „limited" effect of alloying: no matter how much Ag was added to the Pd-based alloy, the effect saturates already at low Ag loading. In favor of this interpretation is the good mixing ability of Pd and Ag, noted in the literature; because of the similarity of the two atoms, they generally form a well-mixed alloy.[4,8,13,21]

5.1.4.4 Changes in the linear region

In the linear region, there are only two overlapping bands assigned to $Pd^{+}CO$ and $Pd^{0}CO$. For $Pd_{2.70}$ we observe them at 2127 and 2118 cm^{-1} at 85 K (Figure 5.9A, spectrum d). For binary samples, the strong peak at 2127 cm^{-1} remains invariable (it was assigned to the isolated Pd cations, thus, it is clear that the position of this band would not be changed on adding Ag), but one weak and inhomogeneous peak appears at 2080 cm^{-1}. This new peak could belong to the $Pd^{0}CO$ species, being red-shifted from 2118 cm^{-1} (by –38 cm^{-1}) due to the effect of the presence of Ag, as described for the bridge region.

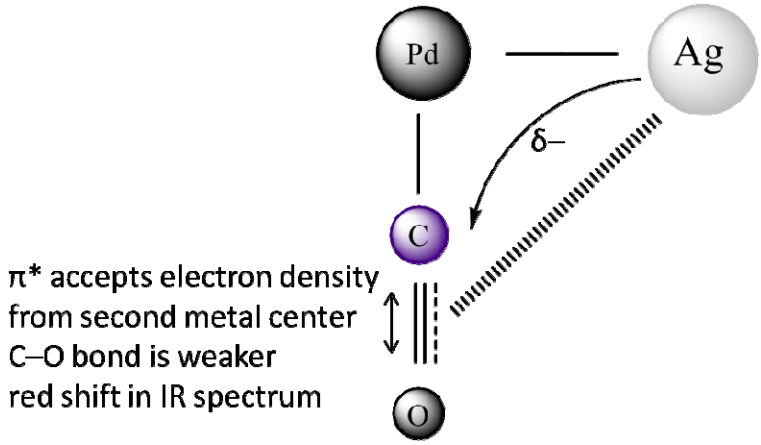

Figure 5.11: Schematic view of an electron effect of alloying against the CO stretching frequency (CO is bonded on Pd in linear mode).

Alternatively, one could imagine that CO is still adsorbed mostly in terminal mode at Pd, but tilted toward Ag so that the CO π^* system can accept electron density from the Ag, which would also lead to a weakening of the C–O bond and concomitant red shifts (Figure 5.11).

In this case the CO acts not only as a traditional σ-donor/π-acceptor to one metal center, but also as a π-donor to an additional metal. The CO ligand in „semi-bridging“ carbonyl acts as a 4 or 6 electron donor.

5.1.4.5 CO adsorption on $Pd_{14.67}Ag_{3.88}$

The instability of monometallic Pd clusters was mentioned already in 5.1.3. The bimetallic samples on the contrary have shown high stability and reproducible IR spectra even after two years of the storage. Apparently, alloying with Ag is able to stabilize them, perhaps because the stronger multiple bonds are disfavored. A similar effect was studied in the work of Cheng *et al.*,[88] who calculated that the melting temperatures (the stability measure) of the 55-atom AgPd bimetallic clusters increase monotonically with the concentration of the Ag atoms first. Finally, they decrease sharply at the specific composition (at high concentration of Ag).

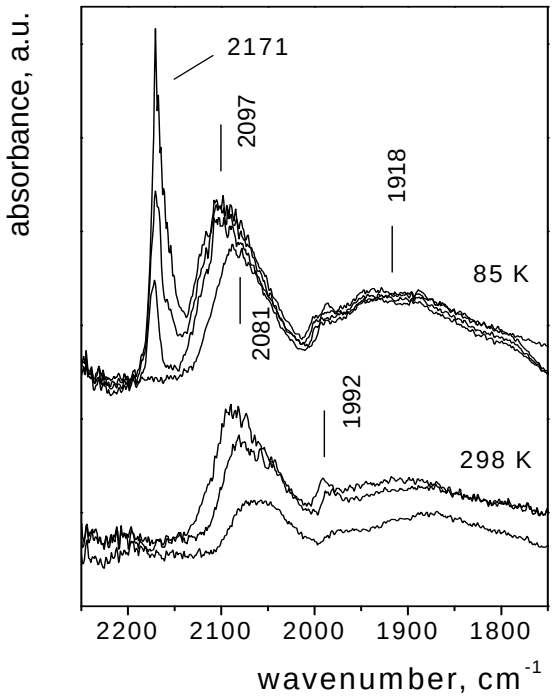

Figure 5.12: FTIR spectra of adsorbed CO (500 mbar and 100 mbar) at 298 K and 85 K on $Pd_{14.67}Ag_{3.88}$, recorded during the desorption.

The IR spectra for the third bimetallic sample $Pd_{14.67}Ag_{3.88}$ (Figure 5.12) with increased loading of Pd show that the cluster structure was possibly destroyed, since there is only one broad peak in the bridge region. It can also be a superposition of several slightly inequivalent peaks.

Two peaks in the linear region could be assigned to Na^+CO (2171 cm^{-1}) and to PdCO linear carbonyls (2081–2097 cm^{-1}). Interestingly, the peak at 2127 cm^{-1} from Pd^+CO species or the one at 2188 cm^{-1} from Ag^+CO are absent in these spectra. The low intensity is most likely due to a very poor dispersion of metallic Pd in a zeolite, as has been observed in the study of Rades *et al*.[5] Their IR spectra of Pd-exchanged NaY were also very noisy. Due to the absence of narrow and intensive bands the $Pd_{14.67}Ag_{3.88}$ sample was not further analyzed.

5.1.5 Quantitative analysis

To obtain the quantitative information, the spectra recorded at room temperature were used to study the amount of actually adsorbed CO. The adsorption bands were fitted with Lorenzian lines. In Figures 5.13 and 5.14 the integrated relative absorbance per gram (the band area) is plotted against the equilibrated CO pressure during the desorption process. Four bands are presented as examples, two of them in the bridge region at 1824($Pd_{2.70}$)/ 1789 cm^{-1} (for both binary samples) and 1992($Pd_{2.70}$)/1950 cm^{-1} (for both binary samples) (Figure 5.13).

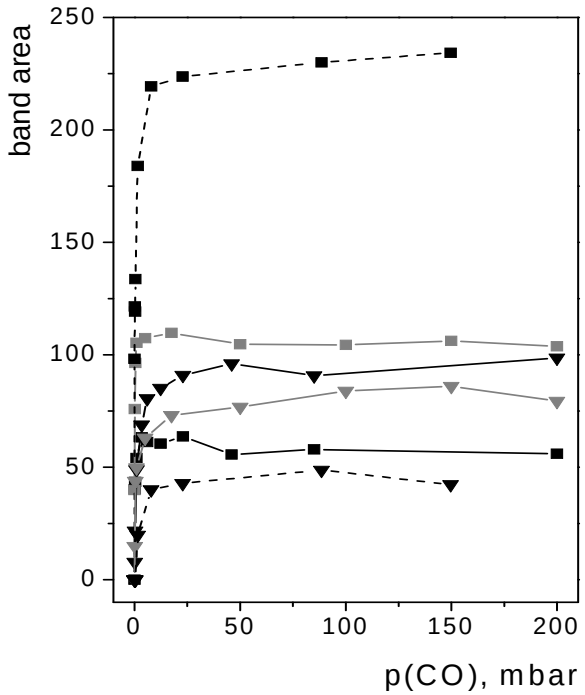

Figure 5.13: Integrated absorption of the CO bands at 1824/1789 cm^{-1} (squares) and 1992/1950 cm^{-1} (triangles) for $Pd_{2.70}$ (dashed line), $Pd_{2.66}Ag_{0.52}$ (black line) and $Pd_{2.80}Ag_{3.61}$ (grey line) during the desorption at 298 K.[71]

These bands have essentially constant areas down to a CO pressure of ≈10 mbar, indicating that the M–CO bonds remain stable. Below this pressure the bonds break and the corresponding IR peaks decrease quickly and disappear. Such a behavior was observed for all major bands in the bridge region.

Clearly, by adding Ag, the number of Pd_3CO positions will be diluted, and in Figure 5.13 one can see a significant decrease of the band area for binary samples compared to the plain Pd sample (squares, 1824/1789 cm^{-1} band). For two-fold positions the value does not differ notably.

The bands in the linear region (Figure 5.14) at 2112($Pd_{2.70}$)/ 2080 (for both binary samples) show a different behavior: with decreasing CO coverage, the integrated relative absorbance of the corresponding peaks decreases slowly. Around 12.5 mbar one observes a sudden decrease of the 2112/2080 cm^{-1} band area, while, simultaneously, a new peak grows in at 2060/2047 cm^{-1} for $Pd_{2.70}$/the binary samples (inset in Figure 5.14).

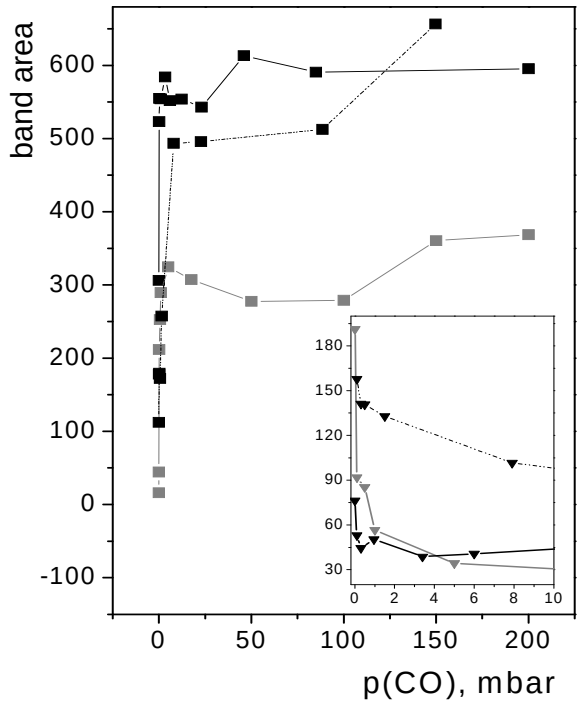

Figure 5.14: Integrated absorption of the CO band at 2112/2080 cm^{-1} (squares) and 2060/2047 cm^{-1} (triangles) for $Pd_{2.70}$ (dashed line), $Pd_{2.66}Ag_{0.52}$ (black line) and $Pd_{2.80}Ag_{3.61}$ (grey line) during the desorption at 298 K.[71]

A peak at 2127 cm^{-1} also disappears (not shown here), and at low CO coverage, there is only a small new peak, which also decreases with further CO desorption. It was already mentioned, that Sheu *et al.*[67] distinguished two states of high and low CO coverage, suggesting that the fully carbonylated Pd_{13} cluster locates near the supercage center, and the partially decarbonylated one interacts with the cage wall.

From Figure 5.14, one can also see that the terminal bond is not as stable as the Pd_2CO or Pd_3CO bonds. This fact is also in line with the other works,[83,85] reporting that, at room temperature, CO adsorbs on Pd mainly in a bridge-bonded configuration. At low CO coverage, an adsorbed CO molecule binds to two or three Pd atoms. At high and/or saturation coverage, the CO molecules become linearly bonded.[85] Theoretical calculations also confirm that CO adsorption at three-fold sites is energetically preferred over on-top sites, and the strongest CO bonding is at bridge positions.[83]

It is also clear from Figures 5.13 and 5.14, that the characteristic behavior of the Pd cluster does not change significantly on adding Ag.

The fitting of the IR bands assigned to the $Pd^{+}CO$/ $Pd^{\delta+}CO$ species at 2123 cm^{-1} for $Pd_{2.70}$ (due to the overlapping with the signal from $Pd^{0}CO$, a more precise separation of the peaks was not possible) and also at 2123 cm^{-1} for both binary samples is shown in Figure 5.15.

These bands for $Pd_{2.70}$ and $Pd_{2.66}Ag_{0.52}$ have lower band area values than those from $Pd^{0}CO$ (Figure 5.14), indicating that there are less $Pd^{+}CO$/ $Pd^{\delta+}CO$ species. For the $Pd_{2.80}Ag_{3.61}$ samples these values are almost equal. It is clear, that adding Ag increases the amount of positively charged Pd species. Since in the bimetallic alloy the electron density transfer generally takes place from Ag to Pd,[14] the appearance of $Pd^{\delta-}$ species is expected. The amount of Na^{+} should be, however, also taken into account. With the increasing metal loading the number of Na cations decreases, but the cations are still needed to preserve the charge balance in NaY. Since Ag can be easily reduced and is present most probably in the neutral form (with exception of some isolated Ag^{+} ions), the Pd ions should remain positively charged. This assumption can explain the increasing amount of the $Pd^{+}CO$/ $Pd^{\delta+}CO$ species with the increasing total metal loading of a zeolite.

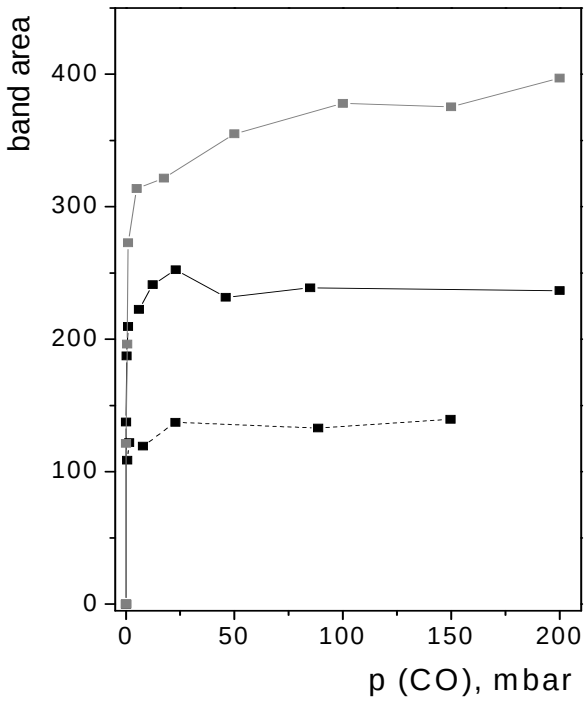

Figure 5.15: Integrated absorption of the CO band at 2123 cm^{-1} for $Pd_{2.70}$ (dashed line), $Pd_{2.66}Ag_{0.52}$ (black line) and $Pd_{2.80}Ag_{3.61}$ (grey line) during desorption at 298 K.

5.1.6 Conclusions based on IR spectra

The proof that the two metals form a nanosized alloy comes already from IR spectroscopy of adsorbed CO. On addition of Ag to Pd, large shifts of the vibrational bands reveal clearly that the CO molecules experience an electronic environment which is different from that of the monometallic samples and that the metals must be alloyed. Because of a surface ensemble effect, CO bonding in bridge geometries is slightly suppressed in alloyed samples, which is clearly noticeable for Pd_3CO species. Furthermore, adding Ag increases the stability of the Pd cluster during the CO adsorption most probably due to the electron density transfer from Ag to Pd (electronic effect of alloying). This also leads to the strong red-shifts in IR spectra, which is interpreted as evidence for a weakening of the C–O bond in the ligand.

Some uncertainty remains about the interpretation of the IR spectra of $Pd_{2.80}Ag_{3.61}$, where the atomic fraction of Ag has multiplied by a factor of 7 without affecting the spectra any further; in agreement with the literature it was found that CO does not adsorb on neutral Ag to any significant extent. If only a fraction of Ag atoms were present in the alloy with Pd and the remaining Ag stayed unalloyed as isolated Ag atoms or even in small clusters, this could explain the similarity of the spectra.

It was also noticed that the higher metal loading of NaY leads to an increase of the amount of positively charged Pd particles that are most likely essential to preserve the charge balance of a zeolite.

5.2 EXAFS Results

The element-specific information about the composition of alloys and, in particular, about coordination numbers and therefore on the particle size can be obtained from Extended X-ray Absorption Fine Structure (EXAFS) experiments at the Pd and Ag absorption edges.

The EXAFS measurements of the $Pd_{2.70}$ and $Pd_{2.66}Ag_{0.52}$ samples were carried out at the beamline X1 of Hasylab, Hamburg, Germany in collaboration with Dr. Sankaran Anantharaman. Unfortunately, the analysis of these results was not completed. The personal communication lets us operate with the approximate total coordination numbers, which are useful for the understanding of the obtained alloy structure.

Since Pd and Ag are adjacent atoms in the periodic table, it is very difficult to distinguish between these two neighboring elements in the EXAFS fits and to determine whether they are alloying. The total coordination numbers are 8.5±0.5 around Pd in both, $Pd_{2.70}$ and $Pd_{2.66}Ag_{0.52}$. Assuming monodisperse spherical clusters this corresponds to a size of at least 55 atoms.[61] Sheu *et al.*[67] synthesized the Pd_{13} cluster with a diameter of 8.2 Å. The 55-atom cluster (the next magic number of atoms) with an icosahedral structure consists of a core, which is just the 13-atom icosahedron, plus 12 more atoms atop the 12 vertices of the icosahedron and 30 more atoms, one in the centre of each of the 30 edges of the icosahedrons (see Figure 5.16). In a cluster of 55 atoms, 42 atoms are on the surface.

Such a cluster still fits in a supercage of NaY with a diameter of 13 Å, it was reported that a cluster consisting of 50–60 Pt atoms fills the supercage of NaY,[30] and Pd atoms have approximately the same size as Pt atoms. In such a case, there seemed to exist significant interaction between Pd and the supercage wall, which can stabilize the cluster size that just fits for a supercage.[30] The possibility of the formation of Pd nanoparticles onto the external surface of the zeolite crystal cannot be excluded completely (it usually takes place if the ion-exchanged zeolite is directly reduced with H_2 at high temperature without activation in O_2).[30] However, this formation is less probable, since in such a case one should expect a bigger size of a cluster and corresponding higher coordination numbers. A formation of 55 atoms, which fits exactly in a supercage, should be stabilized by a zeolite support. Since such a cluster fills

the supercage almost completely, CO can adsorb through four apertures of the supercage (7.4 Å in a diameter). The tetrahedral arrangement of the four 12R windows of every supercage would easily permit coordination of multiple terminal, double and even four triply bridging CO ligands on a Pd surface.[67] There exists also a possibility that a zeolite cristallinity may be destroyed with the formation of bigger pores.

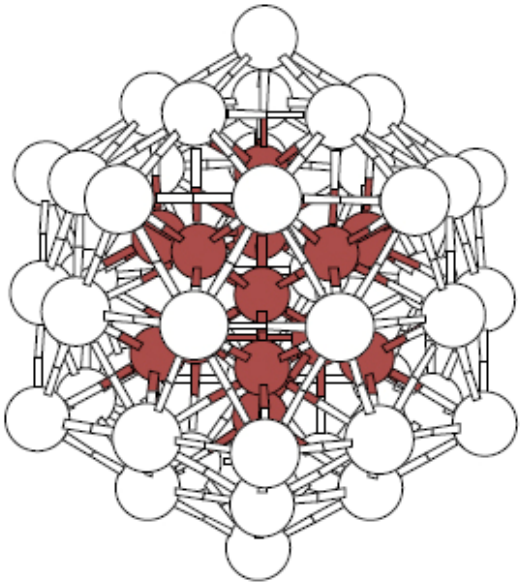

Figure 5.16: 55-atom cluster with an icosahedral structure, dark balls show 13-atom icosahedron.[89]

At the Ag absorption edge the coordination number is only 6.5±0.5 in the $Pd_{2.66}Ag_{0.52}$ bimetallic sample, significantly less than for Pd, indicating that many of the Ag atoms are accommodated in smaller clusters. For random alloying one would expect identical CN values for both elements of a bimetallic sample. The fact that it is somewhat lower for Ag can mean either that Ag has a preference to segregate to the surface, or alternatively that some of the Ag ions are involved in smaller clusters or even completely isolated (agreeing with the finding that IR revealed the presence of isolated Ag^{+}). Conversely, it can be excluded that the minority element, Ag, is located in the core of the cluster, as this should increase its CN to metal neighbors towards 12. The lower coordination number for the minority species reveals that Ag is not located in the core of the particles but either has a slight preference for the surface or a larger fraction of isolated ions, atoms or very small clusters.

5.3 EPR Spectra

Electron paramagnetic resonance spectroscopy is a local non-invasive technique that yields the information on paramagnetic clusters and ions. EPR method has been shown to be an important tool for the characterization of many transition metals in zeolites. In many cases it is possible to distinguish between different oxidation states, coordination numbers, complex symmetries and crystal field strength.[90]

5.3.1 EPR Spectrum of NaY

On the EPR spectrum of an unexchanged NaY (Figure 5.17) one can see two strong signals – one with g = 4.3, the well-known iron signal from impurities in the zeolite and one with g ≈ 2.0, that is also ascribed to the zeolite.[37] According to the work of Liu *et al.*,[37] the signal with g ≈ 2.0 appears due to a small hyperfine coupling, which could be assigned to Al or to Na. Some authors assign both signals to iron impurities in a zeolite.[91]

Mostly, only these two signals were present in the spectra of samples under investigation. The measurements were performed for the samples in different states: calcined, reduced and under CO atmosphere. Some of them revealed additional signals, although almost always weak. The most suitable for the discussion spectra are presented in this section.

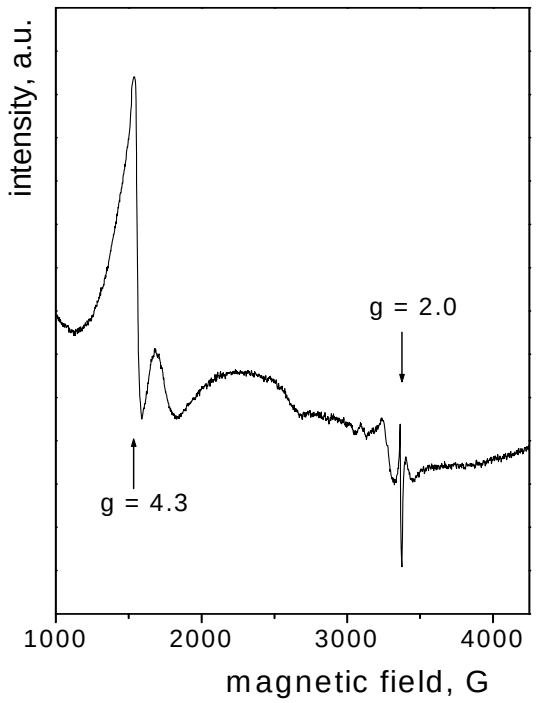

Figure 5.17: X-band EPR spectrum of calcined NaY measured at 20 K.

5.3.2 EPR Spectra of Ag

Various studies of Ag^+-exchanged zeolites were carried out and different paramagnetic clusters, such as Ag_2^+, Ag^{2+}, Ag_3^{2+}, Ag_6^+ and others, were stabilized. The cluster nuclearity depends basically on the Ag loading, however, the hyperfine structure of individual clusters was usually complicated to interpret reliably due to the coexistence of several different structures.[92] Naturally occurring Ag is composed of the two stable isotopes ^{107}Ag and ^{109}Ag, possessing almost the same percentage, viz. ^{107}Ag 51.839% and ^{109}Ag 48.161%, in natural abundance. Their nuclear magnetic moments are nearly equal, viz. −0.11 μ_N of ^{107}Ag and −0.13 μ_N of ^{109}Ag; both isotopes have a nuclear spin equal to 1/2.[93] Although bulk Ag has the electronic configuration of $[Kr]4d^{10}5s^1$, it exhibits diamagnetic ordering, because the incompletely filled $5s^1$ electronic state is inside the completely filled $4d^{10}$ electronic state.[94] Atomic Ag^0 is, however, paramagnetic. Due to the two almost equally abundant isotopes the EPR spectrum of Ag^0 (electron spin 1/2) consists of two doublets.[78] The paramagnetic property of reduced Ag clusters derives from the odd-number of 5s valence electrons in the open-shell configuration.

A large number of the studies were devoted to Ag^+-exchanged A zeolites,[92,93,95-98] and just a few works to Ag in NaY zeolites,[99,100] there exist also several comparative studies of Ag supported on the A, X and Y zeolites.[78,80] The low „popularity" of the Y zeolite can be due to the higher Si to Al ratio and resulting less favorable charge density per sodalite cage to stabilize the ionic Ag clusters.[101] For example, octahedral hexasilver clusters, usual for the A zeolite, have never been found in Ag-X and Ag-Y by any direct method.[80] In the Y zeolite one usually studies Ag^{2+}, produced by γ-irradiation.

The recorded EPR spectra of the $Ag_{0.31}$ sample after calcination, reduction, CO adsorption/ desorption are presented in Figure 5.18.

In the spectrum of the calcined sample (line a) there is only a signal with $g \approx 2.0$, assigned to a zeolite. One can observe an appearance of new signals for the reduced sample (line b), then the CO adsorption affects the spectrum (line c), but a spectrum after desorption (line e) is identical to the one of the reduced sample. It was rather complicated for the simulation. The best fitting is shown in Figure 5.19.

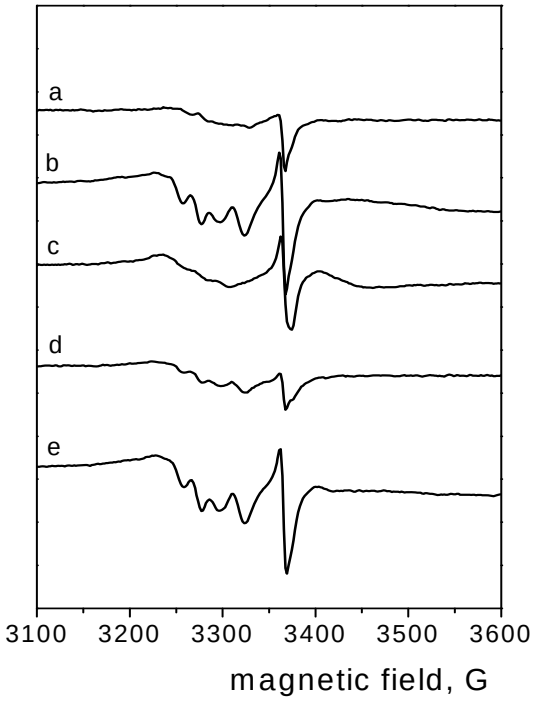

Figure 5.18: EPR spectra of $Ag_{0.31}$ measured at 20 K after (a) calcination, (b) reduction, (c) CO adsorption, (d) during CO desorption (e) after desorption for 8 hours under vacuum.

According to the simulation, there are three species *s1*, *s2* and *s3* with the intensity ratio 1:3.2:4, respectively. Species *s3* with an axial symmetry ($g_\perp$ = 2.008, $g_\parallel$ = 2.095) can be assigned to the zeolite.[37] Two observed doublets for the *s1* ($g_\perp$ = 2.066, $g_\parallel$ = 2.092, $A_\perp$ = 40 G, $A_\parallel$ = 10 G) and *s2* ($g_\perp$ = 2.051, $g_\parallel$ = 2.115, $A_\perp$ = 50 G, $A_\parallel$ = 10 G) species are characteristic for the paramagnetic Ag species. The axial symmetry of the g tensor means that the species are located at or near a typical cation site of a zeolite.

It was reported, that free silver atoms in NaY supports normally exhibit two well-resolved doublets with a large isotropic hyperfine coupling constant of A_{iso} = 590 – 700 G, due to the *s* character of the Ag^0 atom.[78,99,100] However, these paramagnetic species were coordinated to four water molecules, and the water ligands obviously lead to a much softer and more isotropic crystal field.[78] It was also noticed that upon dehydration, silver atoms were no longer screened by water molecules and were then transformed into diamagnetic species.[99]

A smaller hyperfine splitting, which was called superhyperfine splitting, was also observed in the Ag-NaY with Ag^{2+} ions.[99] Such a hyperfine structure was assigned to an interaction with Al nuclei (I = 5/2) of the zeolite framework. It was suggested, that the Ag ions move towards

cationic sites of the zeolite, mainly to sites SI' (see Figure 2.2). Then the Ag ions were bonded to lattice oxygens via ionic bonds. Since neighboring Al are electron acceptors, they exhibited an EPR spectrum with superhyperfine structure due to the Al nuclei.[99] However, it seems clear that Ag^{2+} cannot form in the present system without γ-irradiation and when the starting material is reduced by hydrogen.

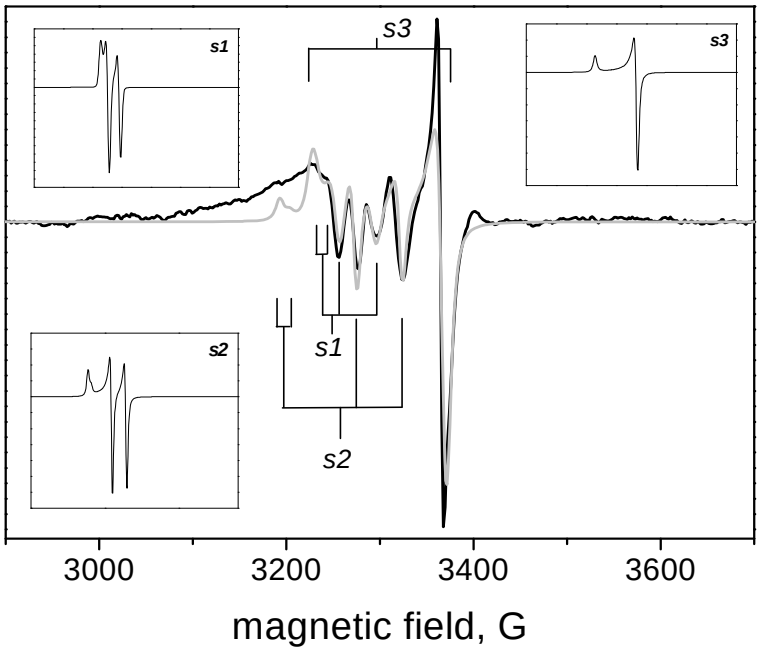

Figure 5.19: EPR spectra of $Ag_{0.31}$ measured at 20 K (black line) and simulated (grey line). Insets show simulated spectra for each of three contributing species, marked as *s1*, *s2* and *s3*.

The g and A values, close to the observed for the $Ag_{0.31}$ sample, were not found in the literature, not taking into account the values corresponding to Ag^{2+} ions. The hyperfine constants depend on the occupation of the unpaired electron in the s-orbital of Ag, or simply on the spin density at the nucleus. For instance, in 12 wt.% Ag/NaA, the highest nuclearity of the reduced Ag_6^+ cluster generally leads to the lowest hyperfine interactions of the silver nuclei with the unpaired electron (about 73 G).[92] For the paramagnetic *s1* and *s2* species in the $Ag_{0.31}$ sample $A_{iso} = (2A_\perp + A_\parallel)/3 = 30$ G and 36.7 G, respectively.

The g_{iso} values (2.075 and 2.072 for the *s1* and *s2* species) are significantly higher than g_e of the free electron, which normally indicates admixture of a transition metal d-orbital into the semi-occupied orbital. $g_\parallel > g_\perp > g_e$ corresponds to a $d_{x^2-y^2}$ elongated octahedral state due to

the spin-orbit coupling.[102] Thus, the ground state of this paramagnetic species can be $[Kr]4d^9 5s^2$. Since the unpaired electron does not locate in the s-orbital, it can explain low A values. At the same time, the low g-anisotropy points to a larger s-orbital contribution. It is quite complicated to assign the observed signal to a specific silver species.

By calibrating the spectrum against a reference sample the spin concentration of the sample was computed via eq. 3.31. The calculations were performed for the signal of reduced $Ag_{0.31}$ (Figure 5.18, line b) and showed, that the sample has a very low spin concentration of $\approx 4 \times 10^{14}$ spins/g. Assuming that it is a signal from paramagnetic Ag species, it corresponds to the only 0.003% paramagnetic Ag atoms; the amount of spins per u.c. is $\approx 10^{-5}$. Thus, most of the silver is EPR silent, that is diamagnetic or unobservable due to the high spin states.

The structures, sizes and charges of the Ag particles/ clusters, formed in NaY, are sensitive to the Ag loading, the calcination/ reduction temperatures and the form of the zeolite (hydrated/ dehydrated). For example, it was reported, that at low Ag^+-exchange levels, all silver ions in hydrated Ag-faujasites are easily reduced to generate clusters, leaving no isolated Ag ions in the lattice.[103] The high- and low-temperature reduction mechanisms produce different species. At low temperature, hydrogen reduction probably resulted in the formation of Ag_3^+ clusters in sodalite cages. Above 623 K, large silver particles were found on the external surface of the zeolite.[104] However, a linear trisilver cluster, extending from a sodalite cage through a D6R window to another sodalite cage, is the most favorable species in reduced faujasites.[80]

The IR spectra of $Ag_{0.31}$ (Section 5.1) confirmed the presence of Ag^+ ions, but Ag^0 atoms are IR inactive.

Relying on the EPR observations, it can be assumed, that the $Ag_{0.31}$ sample contains some minority paramagnetic species, which are characterized by a low g-anistropy and hyperfine splitting constants.

5.3.3 EPR Spectra of Pd

Paramagnetic Pd species supported on different zeolites were also widely investigated by EPR spectroscopy.[23,43,44,105-108] Naturally occurring Pd has one stable isotope ^{105}Pd, 22.33% natural abundance with nuclear spin of 5/2. Other isotopes have a nuclear spin of I = 0 (^{102}Pd, 1.02%; ^{104}Pd, 11.14%; ^{106}Pd, 27.33%; ^{108}Pd, 26.46%; ^{110}Pd, 11.72%,). Isolated Pd^0 with the electronic configuration $[Kr]4d^{10}$, Pd^{2+} and Pd^{4+} are not paramagnetic. In case of faujasites,

Pd^{3+} in the d^7, S = 1/2 state, was observed to exhibit a sharp isotropic singlet,[23,105] and Pd^{+} in a d^9, S = 1/2 state – a sharp anisotropic singlet.[23,105]

In this work the calcined $Pd_{2.70}$ did not exhibit any EPR signals, thus indicating that all the Pd should be in the nonparamagnetic Pd^{2+} or Pd^{4+} state. The spectra of reduced $Pd_{2.70}$, after CO adsorption and desorption are presented in Figure 5.20, and the simulation for the sample under CO atmosphere – in Figure 5.21.

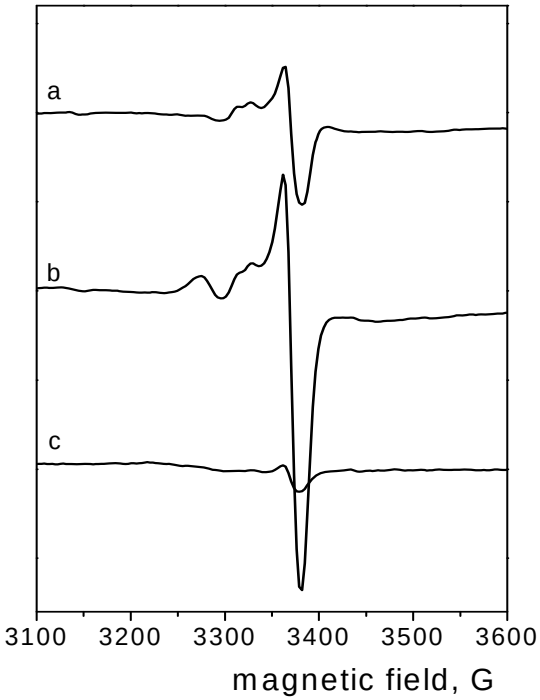

Figure 5.20: EPR spectra of $Pd_{2.70}$ measured at 20 K after (a) reduction, (b) CO adsorption, (c) after CO desorption for 8 hours under vacuum.

The treatment with hydrogen leads to $Pd^{2+} \rightarrow Pd^{+} \rightarrow Pd^{0}$ transformations, also to the formation of small neutral $[Pd_n\text{-}H_z]$ clusters. Pd^{+} ions can occupy SI, SI', SII, SII', SIII and SIII' positions in zeolite Y. The ions at these positions have different coordination symmetry, resulting in different, often overlapping, EPR signals, which also leads to a broadening of EPR signals.[23] A few overlapping EPR signals were obtained also in this work for the reduced sample (Figure 5.20, line a). However, they seem to have low g-anisotropy, which is unusual for Pd^{+} ions, which are characterized by its strong anisotropy with $g_{\perp} << g_{\parallel}$.[23] After CO adsorption (Figure 5.20, line b) the formation of new species was observed, and they have a slightly higher g-anisotropy. After CO desorption these signals disappear, leaving a

weak signal, assigned to a zeolite. It should be mentioned, that this zeolite signal is not permanent, it depends on the metal loading of the zeolite, the measuring temperature, the pre-treatment and also the age of the sample. This signal is not in the focus of the present work, so it will be not discussed in detail. Since the discussed EPR signals from Pd paramagnetic species are near to the $g \approx 2.0$, one cannot be absolutely sure that these signals come not from a zeolite. However, in case of unexchanged NaY, the intensity of the signal at $g \approx 2.0$ was very low (see Figure 5.17). In case of the Pd sample, the line intensities were much higher.
The low g-anisotropy points to a larger s-orbital contribution, which should lead to a large hyperfine interaction for the ^{105}Pd isotope. Hyperfine splitting was, however, not resolved, not only in the present experiments, but also in numerous works,[23,44,105,107,109] due to the low abundance of this isotope. Rarely, the hyperfine pattern with low hyperfine constants was observed.[108]

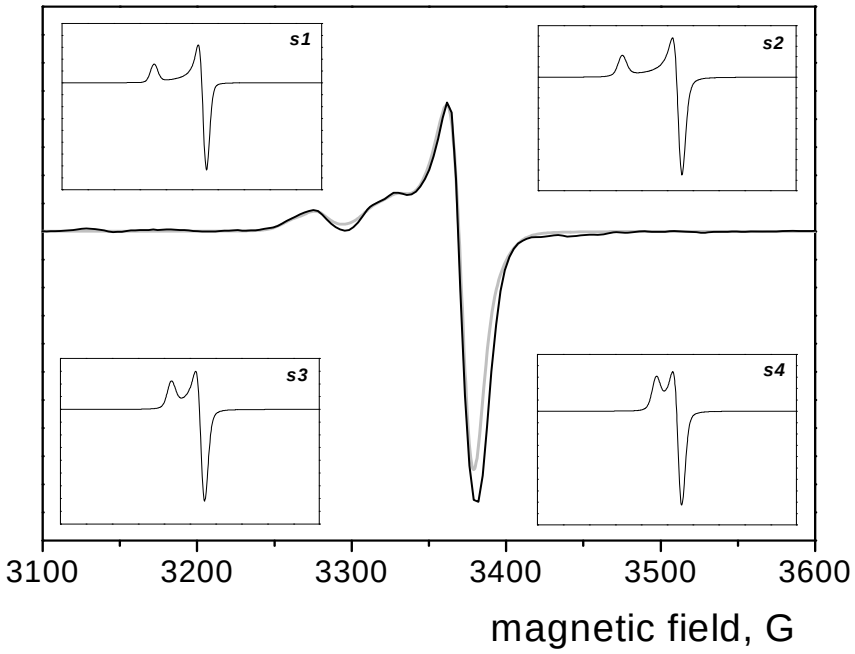

Figure 5.21: EPR spectra of $Pd_{2.70}$ measured at 20 K (black line) and simulated (grey line). Insets show spectra of four contributing species, marked as *s1*, *s2*, *s3* and *s4*.

According to the simulation for the Pd(CO) sample (Figure 5.21), five paramagnetic species contribute to the observed EPR signal with the intensity ratio *s1*:*s2*:*s3*:*s4*:*s5* equal to 1:1:0.7:0.7:1. Four of them have an axial symmetry with an equal $g_\perp$ value of 2.005. $g_\parallel$ values

for *s1–s4* are 2.064, 2.073, 2.041, and 2.032, respectively. *s5* exhibits an isotropic signal with $g_{iso} = 2.004$.

It is not possible to assign these overlapping signals precisely. IR spectra (Section 5.1.3) confirmed that Pd is present in the Pd^0, Pd^+ and $Pd^{\delta+}$ states of oxidation. The positively charged Pd particles and/or small Pd_nH_z/ $Pd_m(CO)_y$ clusters (with possible partial positive charge) may be stabilized by the framework oxygen and exhibit a paramagnetism. Pd clusters with different nuclearity or size can be responsible for the broadening of the EPR signals.

Stokes *et al.*[108] investigated Pd(I) species in ZSM-5 and β-zeolite and also adsorbed CO. $Pd^+(CO)$ species in β-zeolite produced a spectrum with slightly rhombic character, exhibiting overlapping signals with different values of $g_1 = 2.20$; 2.17; 2.12, and constant $g_2 = 2.07$ and $g_3 = 2.05$. The shape of their spectra is very close to the one obtained in this work. They explained the variation of g_1 values by the heterogeneity of the location, symmetry and coordination of the metal-carbonyl complexes. They have also noticed that interactions with the zeolite framework play an important role. The more CO which interacts with Pd, the less the interacion with the framework. For the reduced Pd sample Stokes *et al.* observed similar spectra, with axial/ rhombic symmetry (there was an overlapping of many signals), different $g_{\|}/g_1$ values and identical $g_{\perp}/g_2$, g_3 values. Differences in $g_{\|}/g_1$ values are due to the differences in the zeolite structures.

By calibrating the spectra of reduced $Pd_{2.70}$ (Figure 5.20, line a) and $Pd_{2.70}$ under CO atmosphere (Figure 5.20, line b) against an ultramarine-blue reference sample the spin concentration was calculated via eq. 3.31, and it came to $\approx 7\times10^{16}$ spins/g (corresponding to $\approx 2\times10^{-3}$ spins per u.c.; 0.067% of the Pd atoms are paramagnetic) and $\approx 2\times10^{16}$ spins/g (corresponding to $\approx 6\times10^{-4}$ spins per u.c.; 0.023% of the Pd atoms are paramagnetic), respectively. Thus, CO adsorption reduces the amount of paramagnetic Pd species. It is not unexpected, since CO is a reducing agent and it reduces paramagnetic $Pd^+/Pd^{\delta+}$ species to nonparamagnetic Pd^0. According to the calculations, most of the Pd is present in the diamagnetic/ unobservable form. Although, IR spectra of CO adsorbed on Pd (Section 5.1.3) show the presence of $Pd^+/Pd^{\delta+}$ species, the corresponding IR peaks strongly overlap with the peaks from other species, in particular with those from Pd^0CO, and at low temperature also from $Na^+(^{13}CO)$ species. So, it is hard to calculate, relying on the IR spectra, the ratio of $Pd^+/Pd^{\delta+}$ ions and Pd^0 atoms.

5.3.4 EPR Spectra of bimetallic samples

No reports were found devoted to EPR investigations of AgPd bimetallic clusters supported on zeolites. Although, such studies were probably performed due to the popularity of bimetallic alloys, but without any publishable results. In the present work, EPR spectra of three bimetallic samples under different conditions were measured at room and low temperatures, but most of the spectra are not suitable for the presentation and discussion. The clearest signals were measured for the calcined and reduced $Pd_{2.80}Ag_{3.61}$ samples; they are shown in Figure 5.22. Bimetallic samples under CO atmosphere did not exhibit any remarkable signals.

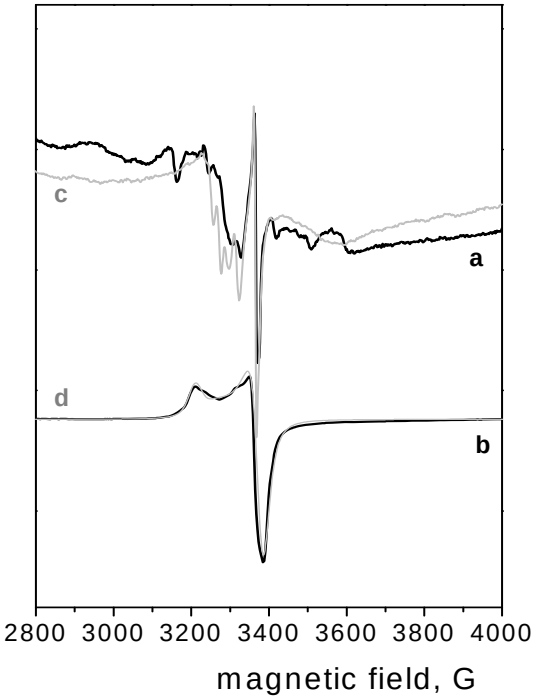

Figure 5.22: EPR spectra of calcined (a) and reduced (b) $Pd_{2.80}Ag_{3.61}$, reduced $Ag_{0.31}$ (c) measured at 20 K. Line d is a simulation of a line b.

In spite of the difficulty for the simulation of the spectrum of calcined $Pd_{2.80}Ag_{3.61}$ (Figure 5.22, line a), one can notice that it is similar to the one of reduced $Ag_{0.31}$ (line c), but it is not so well-resolved. It confirms that the same paramagnetic species, which were observed for $Ag_{0.31,}$ are present also in the bimetallic sample.

Simulation (line d) of the spectrum of reduced $Pd_{2.80}Ag_{3.61}$ (line b) consists of two overlapping signals with an axial symmetry; both species have a $g_{\perp}$ value of 2.003, $g_{\parallel}$ values

are 2.107 and 2.070. The species have 4:1 intensity ratio, respectively. The one with $g_{\perp}$ = 2.003 and $g_{\parallel}$ = 2.107 possesses the highest g-anisotropy, measured in this work, which is close to values, observed by other researchers.[23]

By calibrating the spectra against a reference sample the spin concentrations were calculated via eq. 3.31. For calcined $Pd_{2.80}Ag_{3.61}$ (Figure 5.21, line a) it was equal to $\approx 2\times10^{16}$ spins/g. Assuming that it is a signal from paramagnetic Ag species, this value corresponds to $\approx 5\times10^{-4}$ spins per u.c. (0.015% of Ag atoms are paramagnetic). For reduced $Pd_{2.80}Ag_{3.61}$ (Figure 5.22, line b) the spin concentration is $\approx 2\times10^{17}$ spins/g, assuming that the signal comes from paramegnetic Pd, it corresponds to $\approx 6\times10^{-3}$ spins per u.c. (0.2% of Pd atoms are paramagnetic).

5.3.5 Discussion and conclusions based on EPR spectra

The quantitative results are summarized in Table 5.1.

Table 5.1: Calculated spin concentrations and amounts of paramagnetic atoms for AgPd system.

sample	spins/ g	spins/ u.c.	total amount of Ag/Pd atoms/ g	percentage of paramagnetic atoms
$Ag_{0.31}$ (reduced)	3.6×10^{14}	9.7×10^{-6}	1.2×10^{19}	0.003%
$Pd_{2.70}$ (reduced)	6.8×10^{16}	1.8×10^{-3}	1.0×10^{20}	0.067%
$Pd_{2.70}$ (+CO)	2.4×10^{16}	6.4×10^{-4}	1.0×10^{20}	0.023%
$Pd_{2.80}Ag_{3.61}$ (calcined)	2.0×10^{16}	5.5×10^{-4}	1.4×10^{20} (Ag)	0.015%
$Pd_{2.80}Ag_{3.61}$ (reduced)	2.1×10^{17}	5.6×10^{-3}	1.1×10^{20} (Pd)	0.200%

Concluding from the observations, in case of monometallic Ag, the observed hyperfine structure with two doublets is typical for the paramagnetic Ag species, but it is not possible to assign this EPR signal conclusively. The correlation of the EPR data with the IR observations is complicated by the fact that Ag^0 atoms are paramagnetic and IR inactive, and, vice versa, Ag^+ ions are IR active, but EPR silent. However, the calculated amount of paramagnetic Ag is very low in the monometallic sample.

Although the paramagnetic species of both monometallic Ag and Pd samples exhibit low g-anisotropy which differs from the literature data, the shapes of the spectra of the reduced

$Pd_{2.70}$ and the sample under CO atmosphere are similar to those observed by other researchers, and are characteristic for $Pd^{+}/Pd(CO)^{+}$ species. The percentage of paramagnetic Pd species in the monometallic sample is higher than that one of Ag in $Ag_{0.31}$, but still very low, less than 0.1%. Adding CO, as expected, decreases this amount.

In case of the $Pd_{2.80}Ag_{3.61}$ sample, the EPR signal, observed earlier for the plain Ag sample, revealed in the spectrum of the calcined sample. Interestingly, for the monometallic silver sample it appeared in the spectrum of the reduced $Ag_{0.31}$. With the assumption that this signal belongs to the paramagnetic Ag species, there is a possible explanation of this observation. In case of the plain $Ag_{0.31}$ sample, the Ag ions first occupy cationic positions, and only after hydrogen reduction they can form the neutral paramagnetic species (i.e., Ag^{0}, Ag_3^{0}). In case of the $Pd_{2.80}Ag_{3.61}$ sample, as it was confirmed by the IR results, adding Ag increases the amount of positively charged Pd ions, which most likely compensate the negative charge of the zeolite framework. Thus, paramagnetic neutral Ag species appear already in the calcined sample; the amount of these species is, however, also very low, <<0.1%. There is also the possibility of the silver autoreduction process in the presence of Pd. Such an autocatalytic electroless deposition process (Ag^{+} deposition onto Ag^{0}) was confirmed for the Ag-Pt/SiO_2 catalysts.[12]

The fact that most of the Ag is present in a diamagnetic/ unobservable state is not unexpected. Oxidized Ag clusters are presumably EPR inactive due to the lack of unpaired electrons. The reduction probably leads to the formation of neutral Ag dimers, tetramers and Ag_6 clusters which are EPR silent. Such systems are obviously more stable and favorable in the system under investigation.

Numerous unsuccessful attempts were already done on Ag/NaY to stabilize single paramagnetic silver clusters without γ-irradiation, and this work confirms, that the structure of the NaY zeolite is not suitable for this purpose, in contrast to the NaA zeolite.

For the reduced $Pd_{2.80}Ag_{3.61}$ sample the amount of paramagnetic Pd species was increased by a factor of 3 in comparison with the monometallic reduced $Pd_{2.70}$ sample. It is astonishing, because, according to the IR results (Figure 5.15), the amount of $Pd(CO)^{+}/Pd(CO)^{\delta+}$ species in the $Pd_{2.80}Ag_{3.61}$ sample was also increased by a factor of 3 with regard to the plain Pd sample. A good correlation of these two techniques is clear. Although EPR measurements did not provide any outstanding results, they are in line with the IR measurements, without any contradictions.

6 Experimental results and discussion for PtAg bimetallic nanoalloys

6.1 FTIR spectra of adsorbed CO

6.1.1 Adsorption of CO on Pt

The characterization of Pt nanoparticles with FTIR studies of adsorbed CO was performed in numerous works, both for the monometallic as bimetallic alloys,[24,82,110-113] also in case of Pt supported on NaY zeolite.[5,66,87] A few works were devoted to IR studies of AgPt catalysts, for example, $AgPt/SiO_2$,[12,114] but no literature regarding to AgPt/NaY was found.

For the $Pt_{3.81}$ sample at room temperature, it was recorded a spectrum (Figure 6.1) that is akin to the one, obtained earlier by Akdogan *et al.*[87] for the Pt_{13} clusters in a NaY zeolite, suggesting the presence of a very similar structure.

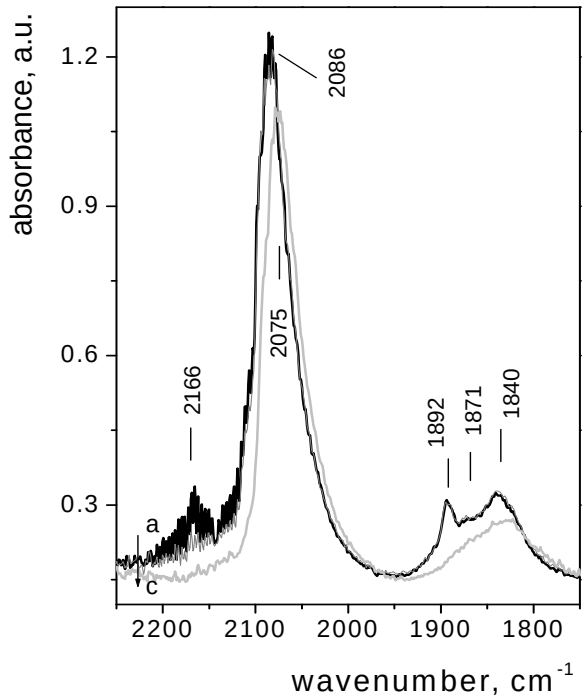

Figure 6.1: FTIR spectra of adsorbed CO (500 mbar) at 298 K on $Pt_{3.81}$, recorded during desorption at the equilibrium pressure of CO (a) 85 mbar, (b) 35 mbar, followed by evacuation for 10 minutes (c).

In the linear region one can distinguish IR band progression at 2166 cm^{-1}, assigned to the R-branch of gaseous CO, and one intensive peak at 2086 cm^{-1} (shifts to 2075 cm^{-1} at low CO pressure). In the bridge region there are the overlapping bands with clear peaks at 1892 and

1840 cm^{-1}. The third contributing peak locates near 1871 cm^{-1}. Such a broad nature of the peaks in the bridge region is usual for Pt.[12]

According to the literature, the band at 2086 (2075) cm^{-1} can be assigned to the Pt^0–CO species and the bands at 1892, 1871 and 1840 cm^{-1} – to the Pt_2CO species.[5] Due to the low activation barrier between two-fold and three-fold bridged species, there may also be contributions from Pt_3CO.[12] In contrast to the $Pd_{2.70}$ sample, it was observed no peaks at the frequencies > 2100 cm^{-1}, which have been usually assigned to the $Pt^{\delta+}$–CO.[87] Akdogan *et al.*[87] did observe a weak signal at 2108 cm^{-1} for $Pt_{13}H_m$ clusters in NaY, assuming some retaining positive charge to preserve the charge balance in the zeolite.

The measuring at 85 K (Figure 6.2) has not resulted to the essential differences in the spectrum, concerning the Pt-CO species.

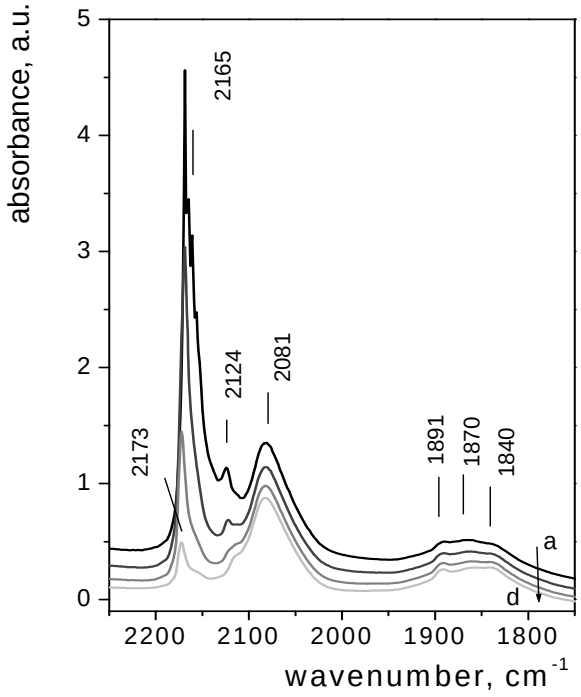

Figure 6.2: FTIR spectra of adsorbed CO (100 mbar) at 85 K on $Pt_{3.81}$, recorded during desorption at the equilibrium pressure of CO (a) 1 mbar, followed by evacuation for (b) 10 minutes, (c) 30 minutes and (d) 60 minutes.

The assignment of the bands remains the same: three overlapping bands in the bridge region, resulting in a one broad peak, belong to the Pt_2CO stretching frequencies; the band at 2081 cm^{-1} belongs to the Pt^0–CO, at 2173 cm^{-1} – to the Na^+CO, at 2165 cm^{-1} – to the $Na^+(CO)_2$

and a small peak at 2124 cm^{-1} – to the $Na^+(^{13}CO)$ species (the adsorption of CO on Na^+ was discussed in section 5.1.1 in detail).

6.1.2 Adsorption of CO on the bimetallic sample

6.1.2.1 Observations and band assignment

The room temperature IR spectra of adsorbed CO for the $Ag_{0.31}$, $Pt_{4.24}Ag_{2.98}$ and $Pt_{3.81}$ samples are shown in Figure 6.3. The adsorption of CO on Ag (line a) was already discussed in section 5.1.2. It is characterized by a peak at 2188 cm^{-1} from Ag^+CO, overlapping with a peak at 2175 cm^{-1} (lines a, b; assigned to CO adsorbed on Na^+ ions), further small peaks belong to CO adsorption on unspecified zeolite centers.

Comparing the spectrum of $Pt_{4.24}Ag_{2.98}$ (line b) with the spectrum of $Pt_{3.81}$ (line c), one cannot observe any significant band shifts in the bridge region (as it was for the bimetallic PdAg), but a new peak appears at 1810 cm^{-1}. In the linear region there is no signal from the Ag^+CO species in the spectra for the bimetallic sample (the same as for the AgPd samples at room temperature). It is in agreement with other works, devoted to AgPt catalysts, who reported that CO does not adsorb on Ag in the presence of Pt at room temperature.[12,115]

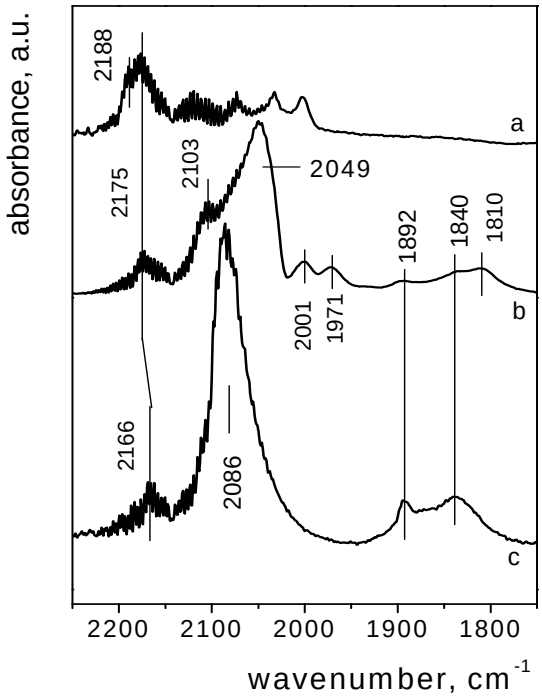

Figure 6.3: FTIR spectra recorded after CO adsorption (500 mbar) at 298 K on $Ag_{0.31}$ (a), $Pt_{4.24}Ag_{2.98}$ (b) and $Pt_{3.81}$ (c). The equilibrium pressure of CO is 100 mbar.

The main peak at 2086 cm^{-1} for the plain Pt (line c) splits in two peaks at approximately 2103 and 2049 cm^{-1}(line b) with adding Ag; also two weak peaks growing at 2001 and 1971 cm^{-1}.
The same range as in Figure 6.3, but measured at 85 K, is presented in Figure 6.4. The observations and assignment of the peaks remain the same. The characteristic peak for the $Ag^{+}CO$ at 2188 cm^{-1} with a shoulder at 2197 cm^{-1} is visible only in the spectrum of the monometallic Ag (Figure 6.4, line a), although in case of the PdAg samples it was also noticeable in the spectra of the bimetallic samples at 85 K.
The intensive bands at 2169–2173 cm^{-1} from the $Na^{+}CO$ species and the corresponding small one at 2123 cm^{-1} from the $Na^{+}(^{13}CO)$ are visible for all samples. From three overlapping and relatively weak bands in the bridge region from the Pt_2CO species for the $Pt_{3.81}$ at approximately 1892, 1871, and 1840 cm^{-1} (Figure 6.4, line c) one can see two bands for the $Pt_{4.24}Ag_{2.98}$ at 1892 and 1836 cm^{-1} (line b). The inhomogeneous and weak peak at 1870 cm^{-1} disappears, but a new peak appears at 1814 cm^{-1}(line b), slightly shifted from the room temperature value of 1810 cm^{-1}. Akdogan *et al.*[87] also observed the growth of this peak for the monometallic Pt after some adsorption–desorption cycles. They assigned this CO stretching frequency to the $Pt_2(CO)_m$ dinuclear carbonyl complex.

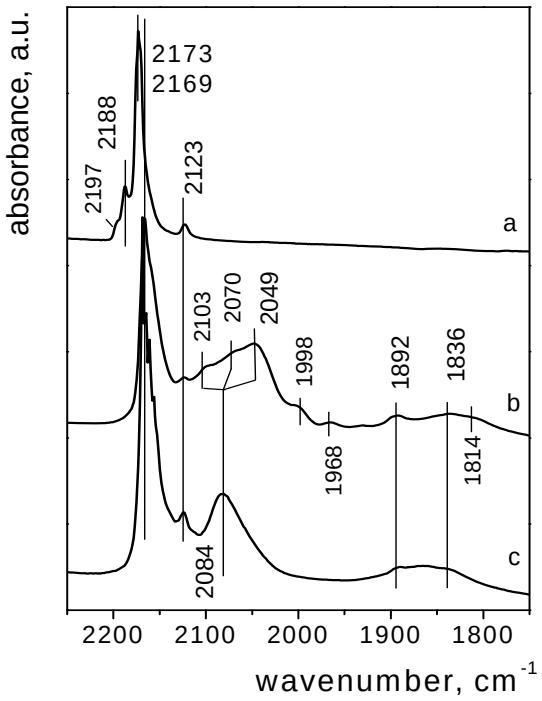

Figure 6.4: FTIR spectra of adsorbed CO (100 mbar) at 85 K on $Ag_{0.31}$ (a), $Pt_{4.24}Ag_{2.98}$ (b) and $Pt_{3.81}$ (c), followed by evacuation for 10 minutes.

The clear peak at 2084 cm^{-1} (assigned to Pt^0CO) for $Pt_{3.81}$ (Figure 6.4, line c) transforms into a broad band for the $Pt_{4.24}Ag_{2.98}$, probably consisting of three overlapping bands (line b). A peak at 1998 cm^{-1} (2001 cm^{-1} at 298 K) was also observed by other researchers for the monometallic Pt sample.[5,87] Rades *et al.*[5] assigned this peak to linearly adsorbed CO on Pt. They explained the unusual lower frequency by a stronger electron back–donation from the Pt atoms to the antibonding $2\pi^*$ orbital of the linearly coordinated CO molecule due to the negative charging of supported metal particles, which occurs because of an electron density transfer, in their case, from the sodium ions remaining in the zeolite after ion exchange.

Akdogan *et al.*[87] observed a growth of the peak at 2001 cm^{-1} also after some adsorption–desorption cycles, simultaneously with a peak at 1813 cm^{-1}, and assigned it to the linearly bonded CO to Pt in the $Pt_2(CO)_m$ dinuclear carbonyl complex. The peak at 1968 cm^{-1} (1971 cm^{-1} at 298 K) lies in the region of the bridge-bonded CO (< 2000 cm^{-1}), but has an unusually high CO stretching frequency for the Pt_2CO. This CO stretching frequency value assigned to Pt species was not found in the literature.

6.1.2.2 Changes in the region of bridge-bonded CO

Due to the absence of strong shifts in the region of bridge-bonded CO, the probable absence of the same geometric (diluting of a number of adjusting Pt atoms) and electronic (the electron density transfer from Ag to Pt) effects of alloying, which have been observed for the AgPd system, can be concluded. The absence of a signal from Ag in the spectrum of the bimetallic sample, neither at 298 nor at 85 K, means that silver is either present only as Ag^0, which is IR inactive, or there is no silver on the surface of the bimetallic alloy (Ag locates in a core).

The literature research showed that the Ag–Pt particles usually possess a core-shell structure,[8,22,25] with no indication of well-mixed alloy formation. Lahiri *et al.*[8] reported core-shell structures with Pt in the core surrounded by a Ag shell which does not agree with the observations of this work. They investigated bimetallic nanorods in aqueous solutions. Feng *et al*.[22] worked with Pt_mAg nanostructures (also in aqueous solutions) and reported a nanostructure transformed from a structure with a Ag–core and an alloyed PtAg–shell to a hollow PtAg alloy structure with the increase in *m*. Thus, in one case the authors synthesized a Pt–core and in another one a Ag–core. It seems to depend on the sample preparation, because Lahiri *et al.* have added Ag to Pt, and Feng *et al*. the contrary – Pt to Ag. Whether and how these two metals mix strongly depends on the experimental method. Wu *et al.*[19]

worked with PtAg nanoparticles in water-in-oil microemulsions and prepared a bimetallic homogeneous alloy structure, mixing equal volumes of two micellar solutions. Ryoo *et al.*[25] synthesized first Pt/NaY and then added $AgNO_3$, which led to the formation of AgPt clusters with the core rich in Pt. In this work, Pt was added to Ag (the sample preparation was described in section 4.1), thus one may expect the formation of a nanostructure with the core rich in Ag. The presence of a Pt–shell would explain an absence of the characteristic Ag peak in the spectrum of the bimetallic sample and, which is more important, an absence of the significant changes in the region of bridge-bonded CO.

The appearance of the new peaks at 1810 and 2001 cm^{-1} (at 298 K) in the spectra of $Pt_{4.24}Ag_{2.98}$ can be explained by the formation of the $Pt_2(CO)_m$ species.[87] AgPt bimetallic structure is probably not that stable as the AgPd one.

6.1.2.3 Changes in the region of linear-bonded CO

However, since there are still the significant changes in the linear region of the IR spectrum, the presence of Ag should somehow affect the electronic properties of Pt. To understand this effect better, one should look at the spectra more closely. The spectra of the $Pt_{4.24}Ag_{2.98}$ sample, recorded at 298 and 85 K during the CO desorption, are shown in Figure 6.5.

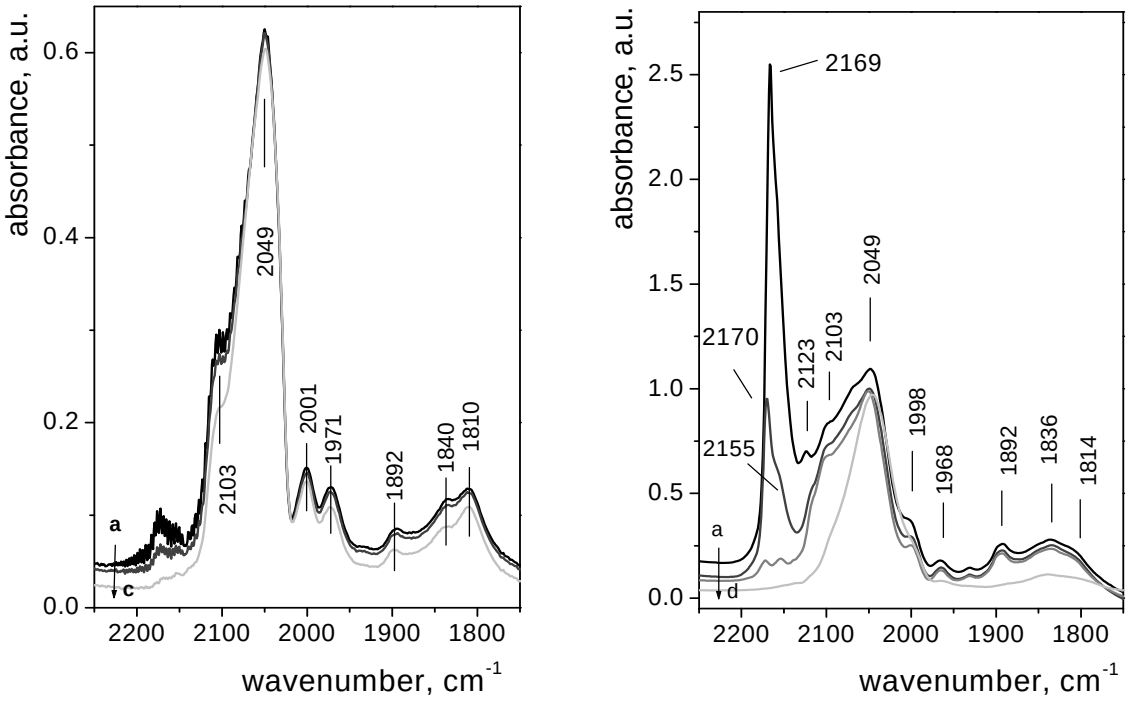

Figure 6.5: FTIR spectra of adsorbed CO (500/100 mbar) at 298 K (left)/ 85 K (right) on $Pt_{4.24}Ag_{2.98}$ recorded during CO desorption, followed by evacuation.

The fitted room temperature spectra of the linear region for the monometallic and bimetallic samples are presented in Figure 6.6.

According to the fitted spectra (Figure 6.6, left), one can distinguish two overlapping peaks in the linear region for the $Pt_{3.81}$, centered at 2088 and 2069 cm^{-1}. They both could be assigned to the Pt^0CO.[66,87] Two Pt^0CO species are not always equivalent – for example, two different Pt atoms could have adjacent atoms with different properties,[5] or it can be one separate Pt atom from six-ring windows (SII sites) and one from the center of a supercage etc. There are a lot of fine factors, and the bands are usually assigned roughly, by the charge values. At lower CO coverage, a peak at 2086 cm^{-1} shifts to approximately 2075–2080 cm^{-1} (Figure 6.1), similar to the plain Pd sample (Figure 5.5), where the cluster changed the location in a supercage depending on the CO coverage.

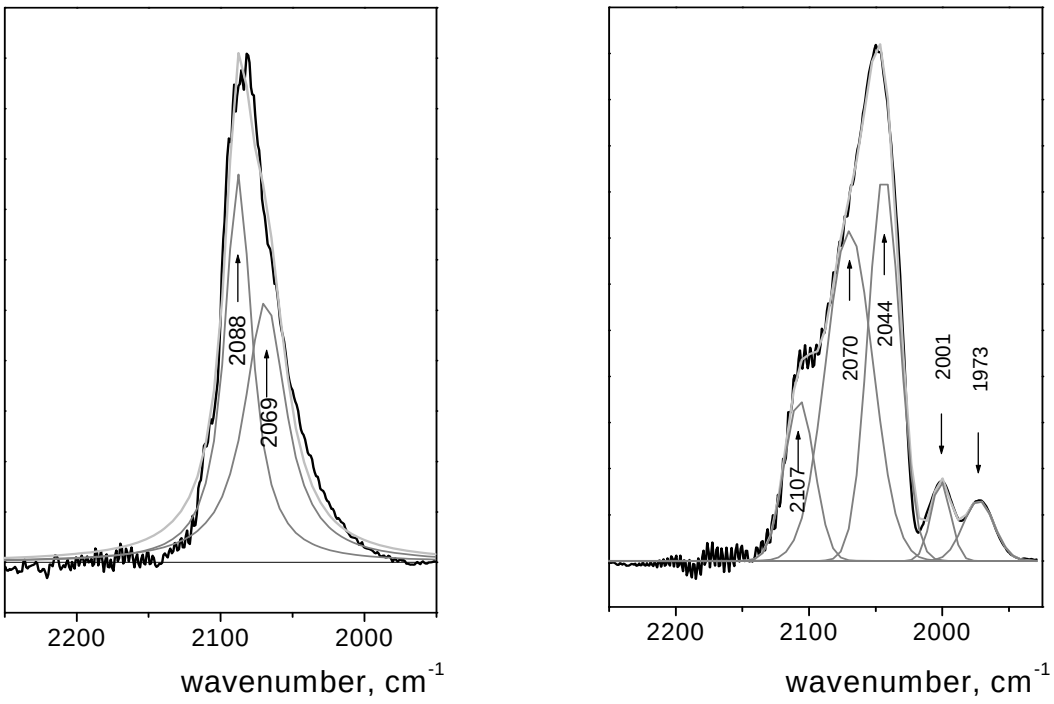

Figure 6.6: FTIR spectra (experiment (black line) and fitted (light grey line)) of adsorbed CO (measured at the equilibrium pressure of CO 90 mbar) at 298 K on $Pt_{3.81}$ (left) and $Pt_{4.24}Ag_{2.98}$ (right).

For the $Pt_{4.24}Ag_{2.98}$ sample the broad band in the linear region could be separated into three overlapping peaks, centered at approximately 2107, 2070 and 2044 cm^{-1} (Figure 6.6, right). The new peak at 2107 cm^{-1} should belong to the $Pt^{\delta+}$–CO species, which have carbonyl band at frequencies ≥ 2100 cm^{-1}.[87] Akdogan *et al.* noticed, that the $Pt^{\delta+}$–CO bond is weak due to

the low Pt – π* back-donation. It is in agreement with the present observations: the peak at 2107 cm^{-1} has a small band area and disappears first during the desorption (quantitative analysis will follow in section 6.1.3). Interestingly, Ag^{+} species disappear, but Pt^{+} species appear in the spectrum of the bimetallic sample. A similar effect was observed for the bimetallic PdAg samples, where the addition of Ag led to an increase of $Pd^{\delta+}$ species. The IR spectrum for the PdAg alloy exhibited, however, both Ag^{+} and Pd^{+} species.

The peak at 2070 cm^{-1} can be undoubtedly referred to the $Pt^{0}CO$ species and a new peak at 2044 cm^{-1} is of more interest. If one looks at the spectra during the desorption (Figures 6.1 and 6.5, lines c and d) it will be clear that these two peaks (at 2086/2081 cm^{-1} at 298/85 K for $Pt_{3.81}$ and at 2049 cm^{-1} at 298/85 K for $Pt_{4.24}Ag_{2.98}$) exhibit a similar behavior, these bonds are more stable than the others and remain intensive while the other bands in the linear region diminish. The fitted peak at 2044 cm^{-1} (Figure 6.6, right) could probably be a peak from the $Pt^{0}CO$, shifted from 2088 cm^{-1} (Figure 6.6, left; red shift by 44 cm^{-1}; at 85 K (fitted spectra are not shown here) this peak shifts from 2084 to 2043 cm^{-1}, red shift by 41 cm^{-1}). The value of this shift is very close to those one observed for PdAg samples in the bridge region (38 cm^{-1}). In addition to a peak at 2044 cm^{-1}, there is still a peak at 2070 cm^{-1} for the bimetallic sample (Figures 6.6, right), indicating the possibility that some Pt atoms remain unaffected by silver. The red shift reveals a weakening of the C–O bond, and a strengthening of the Pt–CO bond, in comparison with the plain Pt sample. This should be due to the electron density transfer from Ag to Pt. Concerning the electron density transfer between Ag and Pt, there is some disagreement in the literature regarding the direction of d-orbital electron transfer.[12] Some researchers, for example, Lima *et al.*[116] confirmed electron transfer from Ag to the Pt 5d orbitals. They investigated PtAg alloys, but with only a fraction of the Ag atoms really alloyed with Pt. Rodriguez *et al.*,[42] on the contrary, reported a transfer from Pt to Ag in case of Ag/Pt(111).

6.1.3 Quantitative analysis

Quantitative analysis was performed by the same way as it was described in section 5.1.5 for the PdAg samples. The absorption bands were fitted with Lorenzian lines. In Figure 6.7 and 6.8 the integrated relative absorbance per gram (the band area) is plotted against the equilibrated CO pressure during the desorption process. For the bridge region there are three bands for the $Pt_{3.81}$ at 1892, 1868, and 1836 cm^{-1} and three bands for the $Pt_{4.24}Ag_{2.98}$ – also at

1892 and 1836 and the new one at 1810 cm^{-1} (Figure 6.7). One can see that, similar to the case of the PdAg samples, most of these bands have essentially constant areas down to a very low CO pressure of ≈0.05 mbar, indicating that the M–CO bonds remain stable. Under vacuum at 298 K for a short time the bonds break and the corresponding IR peaks disappear.

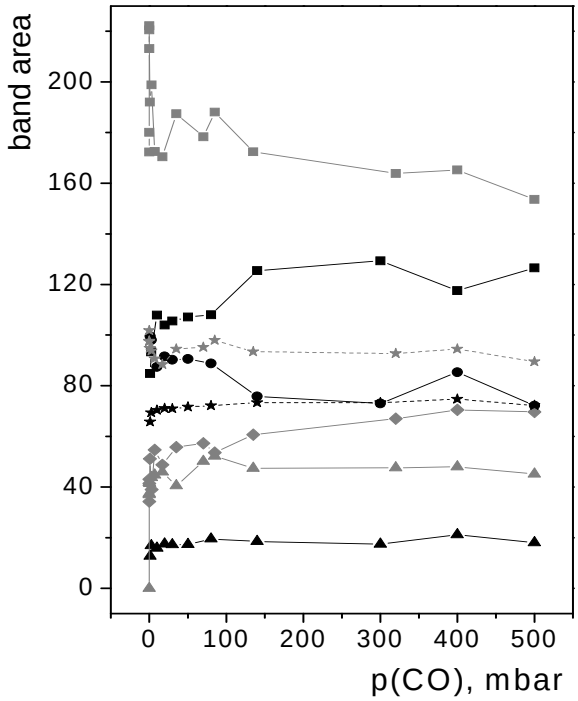

Figure 6.7: Integrated absorption of the CO bands at 1892 (triangles), 1868 (rhombuses), 1836 (squares), and 1810 (circles) cm^{-1} for $Pt_{3.81}$ (grey line) and $Pt_{4.24}Ag_{2.98}$ (black line) during desorption at 298 K. Dotted lines (stars) show average band area value of peaks in the bridge region.

It is also noticable for the peaks at 1892 and 1836 cm^{-1}, which are present in both spectra of the $Pt_{3.81}$ and $Pt_{4.24}Ag_{2.98}$ samples, that the band area is higher for the monometallic Pt sample than for the bimetallic one (Figure 6.7, triangles and squares). An average band area value of three bands in the bridge region for each sample is also plotted in the Figure 6.7 (dotted lines). Here one can see that the average band area value is higher for the monometallic sample by approximately 20%. It contradicts with the supposition that the bimetallic sample can disintegrate to the small separate aggregates (i.e., forming Pt dinuclear carbonyls). In case of the monometallic Pt sample, the possibly formed Pt_{13} clusters entrapped in a supercage have a lower number of Pt atoms on the surface, which are accessible for adsorbing CO than small Pt aggregates. Akdogan *et al.*[87] reported that the Pt dinuclear

carbonyl clusters are in proximity to the zeolite framework and are able to absorb approximately 5 CO molecules per 2 Pt. The observed decrease of the average band area value for the bimetallic sample may be explained by the presence of the IR inactive Ag atoms, which affect the accessibility of the Pt atoms.

At lower CO coverage one observes an increase of the band area value for the peaks at 1836 cm^{-1} ($Pt_{3.81}$) and 1810 cm^{-1} ($Pt_{4.24}Ag_{2.98}$), they become more prominent. When the other bonds are breaking, these two bonds remain favorable, compared to those of other types of bridged CO bands.

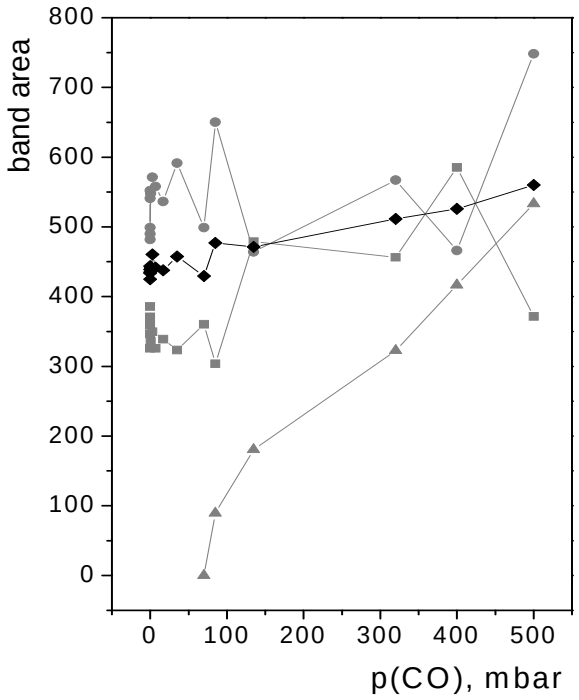

Figure 6.8: Integrated absorption of the CO bands at 2169 (triangles), 2088 (squares), 2069 cm^{-1} (circles) and average value for bands at 2088/2069 cm^{-1} (rhombuses, black line) for $Pt_{3.81}$ during desorption at 298 K.

In Figure 6.8 one can look at the peaks for $Pt_{3.81}$ in the linear region – two from Pt^0CO at 2088 and 2069 cm^{-1}, and one from gaseous CO at 2169 cm^{-1}. The intensity of the latter band decreases very fast and almost linearly proportional to CO pressure. The average band area for two other bands behaves similar to the case of PdAg (Figure 5.12). The integrated relative absorbance decreased slowly with decreasing CO pressure. The individual bands have strong leaps: one peak increases, another one correspondingly decreases. It may be caused by a

fitting error, also by some „flow-over" of CO molecules between coexistent different Pt^0CO species.

The integrated absorption of the four peaks in the linear region of the $Pt_{4.24}Ag_{2.98}$ at 2070, 2044, 2107, and 2001 cm^{-1} (simulation of these bands was shown in Figure 6.6, right) is presented in Figure 6.9. The values for the peak at 1973 cm^{-1} were analogous to those from the one at 2001 cm^{-1}. The band at 2069 cm^{-1} of the $Pt_{3.81}$ sample is also shown here.

The intensity of the peak at 2107 cm^{-1} (triangles) from the $Pt^{\delta+}CO$ decreases very fast; as it was already mentioned above, this bond is very weak.

The Pt–CO bonds with the IR peaks at 2001 cm^{-1} (rhombuses) and 1973 cm^{-1} (not shown) are very stable, their behavior during the desorption is equivalent to those observed for the bridge-bonded CO. They belong most probably to Pt_2CO, but with unusual high stretching frequencies for the bridge-bonded species.

The bands at 2044 and 2070 cm^{-1} (Figure 6.9, squares and circles, respectively) from Pt^0CO behave also similar and ordinary for the linearly bonded CO.

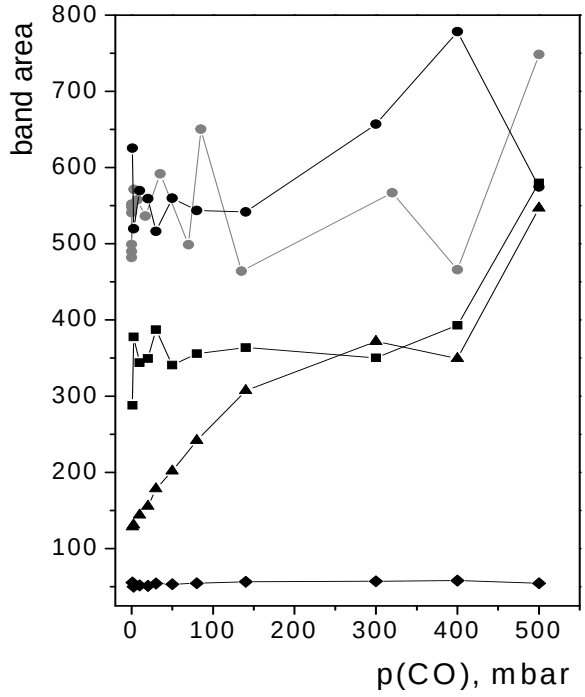

Figure 6.9: : Integrated absorption of the CO bands at 2069/2070 (circles), 2044 (squares), 2107 (triangles) and 2001 cm^{-1} (rhombuses) for $Pt_{3.81}$ (grey line) and $Pt_{4.24}Ag_{2.98}$ (black line) during the desorption at 298 K.

According to the literature,[110] the integrated intensity ratio of linear/ bridge (L/B) bonded CO was dependent on the electron density of a metal surface by both experimental as well as theoretical studies. The higher the electron density of the metal, the lower the L/B ratio. This phenomenon was used to determine the influence of support acidity/ alkalinity on the electron density of supported metal particles.

The calculated linear/ bridge ratio is 5.3 for the monometallic Pt sample and 4.0 for the bimetallic sample, so it can be assumed that the electron density on the platinum is higher in case of $Pt_{4.24}Ag_{2.98}$. This is in line with the fact, that Pt atoms have higher electronegativity and affinity to an electron than Ag atoms, so the electron density transfer from Ag to Pt probably takes place. The other explanation involves that adding Ag reduces the number of sodium atoms in a zeolite, and it was noticed, that the ratio of the linear/ bridge CO depends on support alkalinity.[110]

The average integrated intensity (the band area) of the spectrum of CO adsorbed on the $Pt_{4.24}Ag_{2.98}$ (both linear and bridge regions) is almost by a factor of 2 less than that for the $Pt_{3.81}$. This effect comes mainly from the band intensities of linear Pt–CO complexes, so it can be assumed that the surface concentration of the latter in the alloy is much less than in the monometallic Pt/NaY. A sharp decrease in CO adsorption on Pt due to the Ag coverage of the surface Pt sites was earlier reported.[12]

6.1.4 Conclusions based on IR spectra

The obtained IR spectra are, in principle, characteristic for Pt_{13} clusters in NaY, but they also confirm that some of the Pt atoms are present in the form of $Pt_2(CO)_m$ complexes, described by Akdogan *et al.*[87] The presence of small dinuclear aggregates should lead to a higher amount of accessible Pt atoms for CO than in case of only Pt_{13} clusters. Since the amount of CO, adsorbed on the bimetallic sample, is approximately by a factor of two lower than in case of the $Pt_{3.81}$ sample, it can be assumed that the access of CO molecules to the Pt atoms is essentially suppressed by the presence of Ag.

The signals from Ag^+CO species are absent in the spectrum of $Pt_{4.24}Ag_{2.98,}$ so it can be concluded that if there is Ag on the surface, it is present in the neutral form. Ag unlikely gets into the Pt species, forming the bonds like Pt–Ag–Pt, since no significant changes (i.e., red shifts of the CO stretching frequency) were observed in the region of the bridge-bonded CO, and it is also not the usual behavior for PtAg alloys, according to the previous studies of such systems.[8,16,22,25]

Taking into account the preparation technique of this work, one could expect the formation of a core-shell structure, with Pt–shell and Ag in a core. But, obviously, not all Ag atoms are in the core, since they suppress somehow the CO adsorption on Pt. The presence of Pt should also lead to the autocatalytic reaction $Ag^{+} \rightarrow Ag^{0}$, already in the calcined sample, as it was reported in the work of Schaal *et al.*[12] It would explain the absence of signals from Ag^{+} species in the IR spectra.

6.2 EXAFS Results

The EXAFS measurements of the $Pt_{4.24}Ag_{2.98}$ sample were also carried out at a beamline X1 of Hasylab, Hamburg, Germany in collaboration with Dr. Sankaran Anantharaman. The coordination numbers for the Pt_{13} cluster and dinuclear carbonyls for the comparison are taken from the work of Akdogan *et al.*: Pt_{13} clusters are characterized by a Pt–Pt CN of 5.8±0.6 and $Pt_2(CO)_m$ carbonyls by a CN of 0.9±0.1.[87]

For $Pt_{4.24}Ag_{2.98}$ the coordination numbers of all neighbors are 8.2±0.8 around Ag and 7.9±1.6 around Pt. Silver and platinum are well distinguishable in EXAFS, but unfortunately, Dr. Anatharaman did not finish the analysis of the experimental data and could provide only the common coordination numbers, without distinguishing Pt–Pt, Pt–Ag, Ag–Ag and Ag–Pt neighbors.

Assuming monodisperse spherical clusters, a CN 8 corresponds to a size of approximately 55 atoms, the same as for the AgPd sample.[61] In Section 5.2 the size of such a cluster and its location in NaY were discussed. But in contrast to the bimetallic PdAg sample, the coordination numbers for Ag and Pt are very close, which is an indication, that none of these two elements has a preference for the surface or to the formation of separate small aggregates. A slightly lower number for Pt can be due to the formation of a few $Pt_2(CO)_m$ dimers (according to the IR observations). Although in other works it was found that Pt and Ag most likely form core-shell structures[8,16,22,25] or that only a fraction of the Ag atoms really alloys with Pt,[116] the presence of Ag atoms only in a core would increase the CN for Ag towards 12. So, such a formation does not correlate with the EXAFS results.

There is another possible formation: Ag and Pt particles can be formed in different stages of growth due to the difference in the reduction potentials of Ag and Pt. Both elements have a preference for segregation and the formation of separate particles.[8] The model of partially

separated „layered“ PtAg „alloys” is in line with the IR observations (the absence of the significant changes in the region of bridge-bonded CO).

6.3 EPR Spectra

EPR Spectra of the monometallic Ag sample were shown and discussed in Section 5.3.1.

6.3.1 EPR Spectra of Pt

Paramagnetic Pt nanoparticles were also already studied by EPR spectroscopy, but the number of reports is significantly lower than in case of the Pd species. There is only one of the Pt isotopes ^{195}Pt, with a nuclear spin of I = 1/2 (natural abundance is 33.8%). The other isotopes have a nuclear spin of I = 0 (^{194}Pt, 33.0%; ^{196}Pt, 25.2%; ^{198}Pt, 7.2%). Pt has an electronic configuration [Xe]$4f^{14}5d^{9}6s^{1}$. The Pt^{2+} and Pt^{0} oxidation states are well known, whereas paramagnetic Pt^{+} and Pt^{3+} species are called non-classical states of Pt. Pt^{+} cations supported on NaY usually exhibit a few overlapping orthorhombic EPR signals with resolved ^{195}Pt hyperfine splitting; g-values depend on the cations location in a zeolite.[66,90] The stabilization of the Pt^{3+} cations is difficult in NaY due to the low polarity of this zeolite.[66] Under hydrogen reduction, the formation of $Pt_{13}H_m$ (m up to 30) cluster is possible. It possesses an icosahedral structure, is neutral or with a low positive charge, and is characterized by highly symmetrical EPR spectra.[37,117]

The spectra of the monometallic Pt sample, measured in this work, are shown in Figure 6.10.

In the spectrum of the calcined Pt sample (Figure 6.10, line a) one can see some overlapping orthorhombic signals (the main signal is characterized by $g_1 = 2.55$, $g_2 = 2.22$, $g_3 = 2.03$ ($g_{iso} = 2.23$) and $A_1 = 65$ G, $A_2 = 75$ G, $A_3 = 75$ G), characteristic for the Pt^{+} cations in the NaY zeolite. The detailed information could be found in the works of Schmauke *et al.*[90] and Akdogan *et al*.[66]

The spectrum of the reduced Pt sample (Figure 6.10, line b) is very akin to those observed by Liu *et al*.[37] They assigned a signal with $g \approx 2.0$ to the NaY zeolite; a multiplet with $g_{iso} = 2.357$ represents 12 equivalent Pt nuclei. The detailed analysis can be found in their work.

The spectrum of the Pt sample under CO atmosphere (Figure 6.11, line c) exhibits an EPR signal with an orthorhombic symmetry and not resolved hyperfine interaction with $g_1 = 2.222$, $g_2 = 2.130$, $g_3 = 2.045$ ($g_{iso} = 2.132$). It differs from the observations of Akdogan *et al*.,[87] who observed the orthorhombic EPR signal with $g_{iso} = 1.98$ for the $Pt_2(CO)_m$ aggregates, but the shape of the present signal is similar to that one.

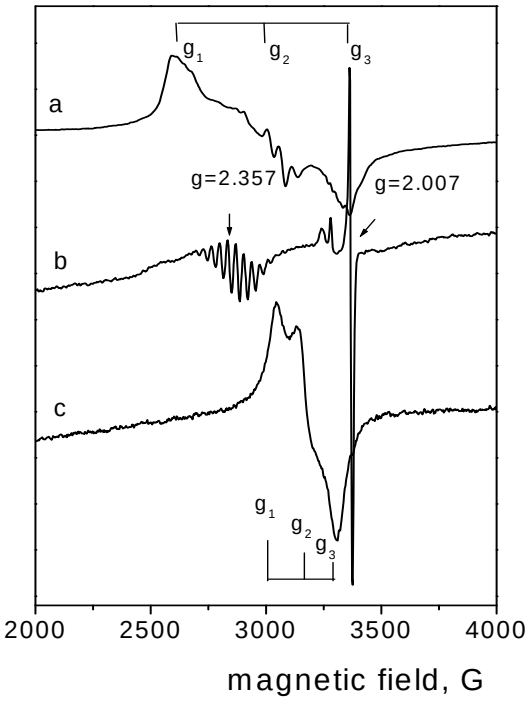

Figure 6.10: EPR spectra of $Pt_{3.81}$ measured at 20 K after (a) calcination, (b) reduction, (c) CO adsorption.

By calibrating the spectra against a reference sample the spin concentrations were calculated via eq. 3.31. They are shown in Table 6.1.

6.3.2 EPR Spectra of PtAg

No clear and strong EPR signals were detected for the bimetallic $Pt_{4.24}Ag_{2.98}$ sample. It should be due to the very low concentration of the paramagnetic Pt/Ag species. The only one clear spectrum of the reduced $Pt_{4.24}Ag_{2.98}$ sample is presented in Figure 6.11. Here one can see the EPR signal with $g_{iso} = 2.07$, which was observed for the plain Ag/ bimetallic PdAg samples and discussed in detail in section 5.3.2. The signal with g = 4.20 belongs to the iron impurities of the zeolite,[37] and an isotropic signal with a high g-value of 2.44 should belong to some paramagnetic Pt species. EPR spectra of the bimetallic sample do not confirm the presence of the Pt_{13} cluster.

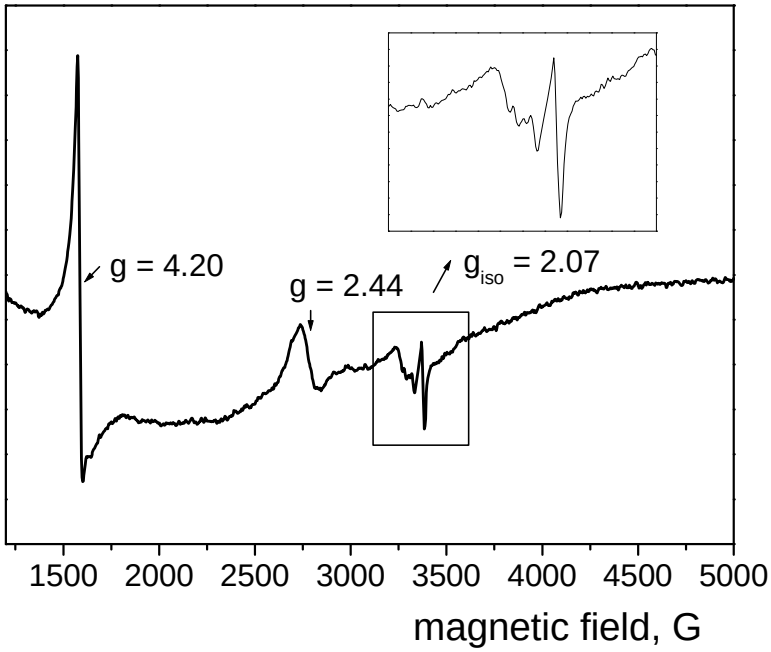

Figure 6.11: EPR spectrum of reduced $Pt_{4.24}Ag_{2.98}$ measured at 20 K**.**

The calculated spin concentrations for this sample are also shown in Table 6.1.

Table 6.1: Calculated spin concentrations and amounts of paramagnetic atoms in PtAg system.

sample	spins/ g	spins/ u.c.	total amount of Ag/Pt atoms/ g	percentage of paramagnetic atoms
$Ag_{0.31}$ (reduced)	3.6×10^{14}	9.7×10^{-6}	1.2×10^{19}	0.003%
$Pt_{3.81}$ (calcined)	1.0×10^{18}	5.7×10^{-2}	1.4×10^{20}	0.745%
$Pt_{3.81}$ (reduced)	2.1×10^{15}	5.7×10^{-5}	1.4×10^{20}	0.001%
$Pt_{3.81}$ (+CO)	3.1×10^{17}	8.4×10^{-3}	1.4×10^{20}	0.220%
$Pt_{4.24}Ag_{2.98}$ (reduced) Ag	2.3×10^{15}	6.3×10^{-5}	1.1×10^{20}	0.002%
$Pt_{4.24}Ag_{2.98}$ (reduced) Pt	6.0×10^{15}	1.7×10^{-4}	1.6×10^{20}	0.004%

6.3.3 Conclusions based on EPR spectra

The highest amount of the paramagnetic Pt^{+} cations was observed for the calcined monometallic sample, almost 1%. Hydrogen reduction, as expected, decreases this amount significantly, but CO adsorption, which leads to the cluster reconstruction and the formation of paramagnetic dinuclear Pt carbonyls with unpaired electrons, increases the spin concentration. However, most of the Pt is present in a diamagnetic/ unobservable form. Apparently, the stable and diamagnetic oxidation states Pt^{0} and Pt^{2+} are favorable.

In spite of the relatively high Ag loading in $Pt_{4.24}Ag_{2.98}$, the amount of paramagnetic Ag atoms remains very low, the same holds for paramagnetic Pt. The ESR signal with g = 2.44 should belong to some $Pt^{\delta+}$ species, which were observed by IR spectroscopy. Besides these species, the bimetallic AgPt sample seems to be almost completely diamagnetic. However, assuming that the EPR signal with g_{iso} = 2.07 belongs to Ag, the EPR spectrum shown in Figure 6.11 contains EPR signals from both Ag and Pt paramagnetic species at the same time (although with a very low intensity). Such a spectrum, concerning the bimetallic PtAg system, was not earlier reported.

If Pt forms 55-atom clusters, as it was confirmed by EXAFS results, the absence of the Pt_{13} multiplet is understandable.

7 Conclusions and comparison of PdAg and PtAg systems

7.1 Geometry of PdAg alloy

Summarizing all of the obtained results for the bimetallic PdAg sytems, the following can be stated:

(1) As confirmed by infrared spectra, Pd and Ag form a nanosized alloy, revealing both electronic and ensemble effects of alloying. From the comparison of two bimetallic samples with different loadings of Ag it was also concluded that only a fraction of Ag atoms alloys with Pd, the remaining Ag stays unalloyed as isolated Ag atoms or in small clusters. IR spectra confirmed the presence of Pd^{+}, Pd^{0}, $Pd^{\delta+}$ and Ag^{+} oxidation states. In the bimetallic sample with the lower loading of Ag, Pd^{0} is the majority species. In the sample with increased Ag loading, Pd^{+}/ $Pd^{\delta+}$ and Pd^{0} species were observed in similar amounts. Ag^{0} is IR silent, since CO does not adsorb on it. It was noticed that adding Ag stabilizes the Pd clusters.

(2) EXAFS results are in line with the assumption concerning isolated silver, since the coordination number for Ag is lower than that for Pd. It was also assumed that the bimetallic alloy has a size of 55 atoms and most likely an icosahedral structure. It should also have a strong interaction with the walls of a zeolite supercage.

(3) Results of electron paramagnetic resonance spectroscopy provided the information, that the metals are mostly present in the diamagnetic state, a minority amount of paramagnetic Ag and Pd species was detected in the bimetallic sample. The signals were amongst referred to Pd^{+}/ $Pd^{\delta+}$ ions and their complexes with hydrogen and carbon monoxide. The calculation of spin concentrations confirmed the information, obtained by the quantitative analysis of IR spectra: namely that adding Ag increases an amount of positively charged (and paramagnetic) Pd species by a factor of three. Pd cations should preserve the negative charge of the zeolite framework, whereas silver remains mostly neutral. The not alloyed fraction of Ag is probably present in form of Ag_2, Ag_4 or even Ag_6 neutral diamagnetic clusters.

The best fitting geometry of the bimetallic PdAg alloy, which is in line with all experimental data, is schematically shown in Figure 7.1. The surface is richer in Pd, but some of the Ag atoms are also present on the surface. These atoms dilute the number of adjacent Pd atoms,

decreasing the amount of Pd_3CO species (as it was confirmed by IR results). Ag atoms obviously also take part in the electron density transfer from Ag to Pd, leading to red shifts of the stretching frequency of CO, bonded to Pd both in linear and bridge modes. Such an alloy should fill the supercage of the NaY zeolite almost completely. The isolated small Ag particles apparently occupy the sodalite cages.

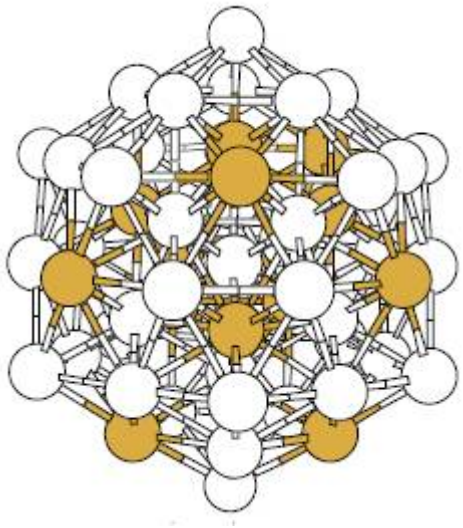

Figure 7.1: 55-atom bimetallic alloy with an icosahedral structure.[89] In this work, dark balls and light balls represent Ag and Pd, respectively.

Since Ag is well-mixed with Pd it explains the identical value for the strong red shifts in the IR spectra (–38 cm^{-1}) of Pd_2CO and Pd_3CO bands relative to the peaks of monometallic $Pd_{2.70}$. The presence of Ag atoms around the Pd atoms should lead to an increase of the electron density on Pd by an electron density transfer from Ag, resulting in a stronger M → 2π backdonation from Pd to the carbonyl C atom. It leads to a strengthening of the Pd–CO bond and a subsequent weakening of the C–O bond.

Obviously, the stronger multiple bonds are disfavored, since alloying with Ag is able to stabilize the bimetallic samples. At the same time it was noticed that the characteristic behavior of the Pd cluster does not change significantly on adding Ag. Carbon monoxide molecules adsorb preferentially on Pd atoms.

EPR and IR spectra confirmed that exchanging of Na^+ by Ag increases the amount of $Pd^+/Pd^{\delta+}$ species, whereas Ag remains mostly neutral in presence of Pd. The isolated neutral

Ag atoms form diamagnetic nanoparticles with even numbers of Ag. That fraction of Ag which is alloyed with Pd most likely loses its electron density due to the transfer towards Pd. Only a minority amount of paramagnetic Ag with the low hyperfine splitting constants and g-anisotropy was detected. Such $Ag^{+}/Ag^{\delta+}$ species are visible also in the IR spectra.

7.2 Geometry of PtAg alloy

The case of PtAg alloy is more complicated. There are some possible structures which are in line with experimental observations, and it is difficult to exclude the formation of one or another. Summarizing the experimental results:

(1) As confirmed by IR spectra, Pt and Ag form a nanosized alloy, since the spectrum of the bimetallic sample is not the arithmetical superposition of the two spectra from monometallic Ag and Pt. Red shifts of CO stretching frequencies in the linear region and the appearance of new peaks signify the electronic effect of alloying. Quantitative analysis provided that the amount of CO adsorbed on Pt decreases with adding Ag. Thus, the access for CO molecules to the Pt atoms is probably essentially suppressed by the presence of Ag (geometric effect of alloying). In contrast to the case of bimetallic PdAg there were no significant shifts of the CO stretching frequency in the bridge region, the latter was almost identical for the monometallic Pt and bimetallic PtAg samples. Apparently, Pt and Ag form an alloy which is different from the PdAg one.

IR spectra confirmed the presence of Pt^{0} and $Pt^{\delta+}$ oxidation states. Ag^{0} is IR silent, Ag^{+} is absent, which is expected in presence of Pt, since such a neighborhood often leads to the complete autoreduction of Ag.

(2) EXAFS results provided the information that the PtAg bimetallic alloy has a size of approximately 55 atoms, the same as the PdAg one. However, the coordination numbers for Ag and Pt are very close, indicating that none of the two elements has a preference for the surface or to the formation of separate small aggregates. A slightly lower coordination number for Pt can be due to the formation of a few $Pt_2(CO)_m$ (in line with IR observations), or that Ag has a slightly lower number of surface atoms.

(3) EPR results provided the information, similar to the AgPd case, that the metals are mostly present in the stable diamagnetic state, a minority amount of paramagnetic Ag and Pt species was detected.

Taking into account the literature database and the experience of other researchers who established that Ag and Pt have a preference to segregation and the formation of separate particles,[8,16,21,24,116] the probable structure of the AgPt nanoalloy is schematically shown in Figure 7.2.

In such a system, there is a large fraction of the surface with only Pt, which should give the same CO stretching frequencies as for the monometallic Pt. From the other side, there is the fraction of neutral Ag (IR inactive, CO does not adsorb on Ag^0). Thus, CO molecules have no access to Pt atoms, and the general amount of CO that is adsorbed on Pt decreases, as it was stated based on IR results. Actually, such a system should be called a microphase separated system, since the elements are not really alloying on an atomic level. But taking into account the nanosize of the system under investigation, it is often called a "nanoalloy".

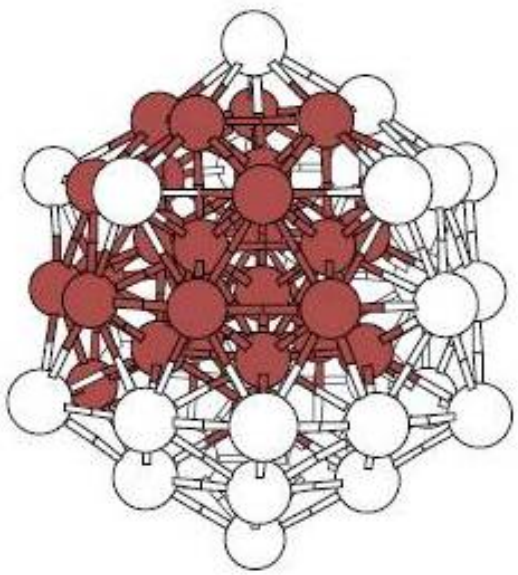

Figure 7.2: 55-atom bimetallic alloy with an icosahedral structure.[89] In this work, dark balls and light balls represent Ag and Pt, respectively.

Some of the Pt atoms have a neighboring Ag, which should lead to an electron density transfer from Ag to Pt, similar as it was described for AgPd, resulting in red shifts of the CO stretching frequency (a shift by 44 cm^{-1} was observed in the linear region). This structure is also in line with the preference of Ag and Pt to segregate and the general coordination numbers for both elements should be close (since Ag locates not only in a core, but have a large fraction of surface atoms).

Thus, two bimetallic nanoalloys with different structures were successfully synthesized. According to the theory of alloy formation one of the most important effects affecting an alloying structure is the effect of the component atom size. Oversized atoms implanted in an ideal crystal lattice cause compression, which results in higher strain energy than occurs with undersized atoms. Oversized atoms tend to segregate to the surface.[1] It was also reported, that in the bimetallic alloy smaller doping atoms have a strong tendency to be incorporated inside the cluster.[118] In case of PtAg and PdAg alloys, Pt and Pd have the same size (see Table 7.1), which is insignificantly lower than that of Ag.

Another important factor for the formation of a certain nanoalloyed structure is the preparation method and oxidation–reduction parameters.[20] In this work, both PdAg and PtAg samples were prepared first by an ion exchange with Pd/Pt solution, and then the silver salt was added. The oxidation–reduction parameters were also very close.

Table 7.1: Chemical properties of Ag/Pt/Pd.

metal	atom radius[119] (empirical), Å	electro-negativity,[120] Pauling units	electron affinity,[121] kJ mol^{-1}	electronic configuration	standard reduction potential,[122] V
Ag	1.44	1.93	125.6	[Kr]4d^{10}5s^{1}	0.799
Pt	1.38	2.28	205.3	[Xe]4f^{14}5d^{9}6s^{1}	1.188
Pd	1.38	2.20	53.7	[Kr]4d^{10}	0.915

It was also reported that the difference in the rates of reduction (or the reduction potential) often plays a deciding role. Each species has its own intrinsic reduction potential; the more positive the potential, the greater the species affinity for electrons (which also correlates with the electronegativity value) and tendency to be reduced. Since Ag and Pt have a relatively large difference in the reduction potential (see Table 7.1), these two elements reveal a preference to the formation of a segregated structure. Such an explanation was proposed for some bimetallic alloys with core-shell structure.[8,16,34]

Obviously, in this work Pt and Ag nanoparticles were not formed simultaneously, but on the different stages of the reduction process. Pd and Ag have a smaller difference, which should explain why they form a better mixed nanoalloy.

Summary

Over the last decade bimetallic or even multimetallic catalysts have replaced monometallic catalysts in industrial processes due to the beneficial activity, selectivity, and stability modifications that may be achieved by the inclusion of additional metals.[12] Bimetallic nanoalloys are very promising candidates for the investigation and development in catalysis, electronics and optics. They have attracted so many studies in order to accumulate the knowledge for the systematic design of better catalysts. Before one can control the nucleation of the two components, achieving the desired size, structure and composition distribution (which is quite challenging), a thorough study is needed to understand the complicated mechanisms of alloying at the nanoscale. For the successful particle design a detailed knowledge of the particle formation is needed.

The present work is composed of two main parts dedicated to the characterization of NaY supported AgPd and AgPt bimetallic alloys by FTIR and X-Band EPR spectroscopes, EXAFS and nitrogen sorption analysis techniques. A primary attention was devoted to the effects of alloying and the corresponding changes of electronic, structural, chemical and magnetic properties.

The bimetallic nanoclusters were synthesized in the pores of NaY zeolite support by chemical methods including the aqueous ion-exchange, oxidation and hydrogen reduction.

On the basis of acquired data it was possible to establish that in both PdAg and PtAg the two elements form a nanosize alloy. IR spectra of bimetallic samples are not the arithmetical superposition of monometallic Pd/Pt and Ag spectra. Two possible structures, which are in line with the experimental data, are suggested for the two systems.

For the PdAg case, as it was assumed, the obtained structure is most likely the 55-atom well-mixed alloy, with a small fraction of Ag atoms, which are alloyed with Pd. This structure does not change with adding further Ag. It locates most probably in the supercage of NaY, being stabilized by the zeolite walls, since such a size corresponds exactly to the supercage size. Two effects of alloying were recognized for the PdAg nanoalloy. First, the electronic effect of alloying due to the electron density transfer from Ag to Pd develops in strong red-shifts of the CO stretching frequency both in the linear and bridge regions of IR spectra. Probably also due to the electronic effect of alloying, the doping with Ag stabilizes the Pd cluster. Secondly, the geometric effect of alloying was characterized by the decrease of the

CO amount, adsorbed on Pd in a 3-fold mode, caused by the dilution of the number of adjacent Pd sites by Ag atoms.

A fraction of non-alloyed Ag remains most probably neutral, whereas Ag possibly occupies the sodalite cages, forming the diamagnetic Ag_2, Ag_4 or Ag_6 aggregates. Such particles could occupy adjacent sodalite cages, extending through the hexagonal prisms.

The presence of Pd^+, $Pd^{\delta+}$, Pd^0, Ag^+ oxidation states was confirmed by IR and EPR spectroscopy measurements, although the amount of paramagnetic Pd^+/ $Pd^{\delta+}$ is very low. Obviously, the NaY zeolite with its unique structure is not a suitable support for the stabilized paramagnetic species.

Pt and Ag also form a bimetallic alloy with a size similar to that of PdAg (approximately 55 atoms), locating in the supercage of NaY, but with a different structure. Possibly due to the disparity in the reduction potential, Ag and Pt have a tendency to segregate, forming a "layered" alloy, which is similar to the core-shell one, but without a closed core (some of the "core" atoms have an access to the surface). The formation of such a structure is possibly due to the high Ag loading of the sample: there are too many Ag atoms to be accommodated only in the nanocluster core. Such an alloy has strongly segregated monometallic parts. Two effects of alloying were also recognized for the PtAg nanoalloy. The electronic effect of alloying due to the electron density transfer from Ag to Pt develops in strong red-shifts of the CO stretching frequency in the linear region of IR spectra and also in the appearance of new peaks. The geometric effect of alloying was accompanied by the decrease of the amount of CO adsorbed on Pt, since the access to the Pt atoms was prevented by the Ag atoms. According to the coordination numbers, neither Pt nor Ag has a preference to form small aggregates.

The presence of $Pt^{\delta+}$ and Pt^0 oxidation states was confirmed by IR and EPR spectroscopic measurements; the amount of paramagnetic $Pt^{\delta+}$ is also very low. It was calculated that exchanging Na cations with Ag leads to the increase of positively charged Pt. Ag undergoes most likely the autoreduction process and stays in the neutral form. There is no evidence that Pt clusters are completely neutral. The partially charged Pt cations, visible in the IR and EPR spectra, could be isolated and/or belong to the Pt clusters.

In summary, new nanosystems of a great potential for heterogeneous catalysis and other application fields were successfully synthesized and characterized. NaY proved to be a great support for the stabilization of clusters with a size of 55 atoms and less. The fact that even a

small doping of Ag can stabilize a small Pd cluster can be very useful for a further research, the purpose of which is to improve the stability of Pd catalysts. It is also essential that only a small amount of Ag goes inside the Pd cluster, not significantly affecting its properties.

In case of the PtAg alloy, the importance of the difference in the reduction potential for the alloying process was demonstrated. It could be useful for the researchers who synthesize the core-shell/ layered structures on purpose. It is, for example, a very attractive direction in case of core-shell catalysts with very thin noble metal shells (Pt, Pd) on a proper nonnoble metals core. Such a structure greatly reduces the use of noble metals, which are expensive.

In general, it was also demonstrated that FTIR spectroscopy of adsorbed CO can be a very useful technique, giving the evidence of alloy formation.

Zusammenfassung

Im Laufe der letzten Jahre wurden auf dem Gebiet der industriellen Prozesse die monometallischen durch die bimetallischen und multimetallischen Katalysatoren ersetzt. Der Grund dafür liegt in den verbesserten Modifikationsmöglichkeiten, die durch das Beimengen unterschiedlicher Metalle zu einer verbesserten Aktivität, Selektivität und Stabilität der Katalysatoren führen können. Die bimetallischen Nanolegierungen weisen ein hohes Potential für die Forschung und Entwicklung in den Bereichen der Katalyse, Elektronik und Optik auf. Dies ist zurückzuführen auf die steigende Anzahl der Studienarbeiten zum Zweck der Sammlung von spezifischem Wissen, welches der systematischen Gestaltung dienen soll, um die Katalysatoren noch weiter zu verbessern. Eine große Herausforderung ist es die gewünschte Größe, Struktur und die optimale Zusammensetzung der Komponenten zu erstellen. Die komplizierte Funktionsweise der entstehenden Legierungen muss über weiterführende Forschungen im Nanobereich belegt und verstanden werden, bevor diese kontrolliert eingesetzt werden können und der zielführenden Partikelgestaltung dienen.

Diese Arbeit ist in zwei Systemdarstellungen gegliedert, die sich mit der Charakterisierung der PdAg und gleichermaßen der PtAg bimetallischen Nanolegierungen im NaY-Zeolith mit den analytischen Messtechniken FTIR, X-Band ESR, EXAFS und der Stickstoffsorption befassen. Der Schwerpunkt dieser Arbeit liegt auf der Untersuchung der Legierungseffekte und der folgenden Änderungen in den elektronischen, strukturellen, chemischen und magnetischen Eigenschaften. Durch chemische Verfahren wie dem Ionenaustausch, der Oxidation und der Wasserstoffreduktion wurden die bimetallischen Nanocluster in den Poren des NaY-Zeoliths erfolgreich synthetisiert.

Auf der Basis der abgeleiteten Datenreihen war es möglich zu ziehen, dass in den beiden Systemen Ag und Pd bzw. Pt eine Nanolegierung bilden. Die IR Spektren dieser bimetallischen Proben sind nicht die rechnerische Überlagerung der monometallischen Pd/Pt und Ag-Spektren. Der Übereinstimmung der experimentellen Daten folgend wurden zwei mögliche Strukturen für die beiden Systeme vorgeschlagen.

Für den Fall des PdAg ist mit hoher Wahrscheinlichkeit die 55-atomige gut vermischte Legierung einer kleinen Fraktion der Ag-Atome verbunden mit den Pd-Atomen gegeben. Sie befindet sich vermutlich in dem Super-Käfig des NaY-Zeolithes, durch die Zeolithwände

stabilisiert. Diese Struktur ändert sich mit dem weiteren Zusatz von Ag nicht; außerdem stabilisiert das Dotieren mit Ag den Pd-Cluster unter CO Atmosphäre.

Es wurden zwei Legierungseffekte der PdAg-Nanolegierung festgestellt. Als Erstes zeigt sich der elektronische Effekt der Legierung wegen der Elektronendichteübertragung vom Ag zum Pd unter starken Rotverschiebungen der C–O Bindungsvibrationsfrequenzen in den linear und verbrückt gebundenen Bereichen der IR Spektren. Zum Zweiten ist der geometrische Effekt der Legierung auf die Absenkung der CO Menge zurückzuführen, die von dem Pd in dem dreifachen Bindungsmodus adsorbiert wurde. Die Zahl der benachbarten Pd-Atome, die dafür nötig sind, wurde mit den Ag-Atomen vermindert.

Die unlegierten Ag-Atome bleiben neutral und besetzen vermutlich die Sodalith-Käfige, in denen sie die diamagnetischen neutralen Ag_2-, Ag_4- oder Ag_6-Aggregate bilden können. Verbunden durch die sechskantigen Prismen können solche Partikel auch zwei angrenzende Käfige besetzen.

Die Anwesenheit der Pd^+-, $Pd^{\delta+}$-, Pd^0-, Ag^+-Oxidationszustände wurde mit den IR- und ESR-spektroskopischen Messungen bestätigt, wobei der Anteil an paramagnetischen $Pd^+/Pd^{\delta+}$ sehr niedrig ist. Mit seiner einmaligen Struktur ist der NaY-Zeolith offenbar nicht der richtige Träger um die paramagnetischen Spezies zu stabilisieren.

Im Fall des PtAg Systems werden ebenfalls bimetallische Nanolegierungen ähnlich der Größe des PdAg (ca. 55 Atome) gebildet, jedoch mit einer anderen Struktur. Diese führt vermutlich aufgrund der Disparität der Reduktionspotentiale zu einem Segregieren der Ag- und Pt-Atome und zu der damit verbundenen Bildung einer „geschichteten“ Legierung. Eine solche Legierung ist der Kern-Schale-Struktur ähnlich, mit dem Unterschied, dass zum einen der Kern nicht komplett geschlossen ist und sich einige Atome dieser Art auf der Oberfläche befinden. Die Bildung solcher Strukturen wird möglicherweise durch die hohe Menge der Ag-Atome in der Probe ausgelöst, da es zu viele Ag-Atome gibt, um in dem Kern der Legierung einen Platz einzunehmen. Auf diese Art erhält die Struktur stark segregierte monometallische Bestandteile, die sich ebenfalls höchstwahrscheinlich in dem Super-Käfig des NaY-Zeoliths befinden.

Die beiden Legierungseffekte wurden bei PtAg ebenso festgestellt. Der elektronische Effekt der Legierung aufgrund der Elektronendichteübertragung vom Ag zu der Pt zeigt sich in den starken Rotverschiebungen der C–O Bindungsvibrationsfrequenz in den linearen Bereich und auch in das Auftreten neuer Peaks.

Der geometrische Effekt der Legierung war markant durch die niedrigere Menge an auf dem Pt adsorbierten CO, denn der Zugang zu den Pt-Atomen ist durch die Ag-Atome behindert.
Den Koordinationszahlen entsprechend haben weder Ag- noch Pt-Atome die Tendenz, kleinere Aggregate zu bilden.
Die Anwesenheit der $Pt^{\delta+}$- und Pt^{0}-Oxidationszustände wurde mit den IR- und ESR-spektroskopischen Messungen bestätigt, wobei der Anteil an paramagnetischem $Pt^{\delta+}$ ebenfalls sehr niedrig ist.
Es wurde berechnet, dass der Austausch der Na-Kationen mit dem Ag zu einer Erhöhung der Anzahl positiv geladener Pt-Teilchen führt. Ag geht vermutlich einen Autoreduktionsprozess ein und bleibt deswegen neutral. Zudem gibt es keine Beweise, dass die Pt-Cluster vollständig neutral sind. Die teilgeladenen Pt-Kationen, die in den IR- und ESR-Spektren sichtbar sind, können sowohl isoliert als auch Teil des Pt-Clusters sein.
Zusammengefasst sind neue Nanosysteme mit einem großen Potenzial für die heterogene Katalyse und andere Applikationsfelder erfolgreich synthetisiert und charakterisiert worden. Der NaY-Zeolith erwies sich als ein gut stabilisierender Träger für die kleinen Cluster, die aus 55 oder weniger Atomen bestehen. Die Tatsache, dass selbst eine kleine Dotierung mit Ag den Pd-Cluster stabilisieren kann, könnte für jene Forscher nützlich sein, die die Erhöhung der Stabilität der Pd-Cluster zum Ziel haben. Ein wesentlicher Punkt ist, dass nur ein kleiner Teil der Ag-Atome in den Pd-Cluster eindringt und deswegen seine Eigenschaften nicht bedeutend ändern kann.
Die Bedeutung des Unterschieds des Reduktionspotenzials für den Legierungsprozess wurde am Fall der AgPt-Legierung demonstriert. Es kann für die Forscher nützlich sein, welche die Legierungen mit einer Kern-Schale-Struktur zu herstellen beabsichtigen. Die Herstellung der Katalysatoren mit der Kern-Schale-Struktur, bei der eine sehr dünne Schicht des Edelmetalls (Pt, Pd) den Kern aus einem kostengünstigeren Metall bedeckt, ist nur ein Beispiel dafür.
Im Allgemeinen wurde auch demonstriert, dass die FTIR-Spektroskopie des adsorbierten CO eine sehr wertvolle Methode ist, mit deren Hilfe die Legierungsbildung untersucht werden kann.

List of Figures

List of Tables

Bibliography

(1) Guczi, L. *Catalysis Today* **2005**, *101*, 53.

(2) Babu, P. K.; Kim, H. S.; Oldfield, E.; Wieckowski, A. *Journal of Physical Chemistry B* **2003**, *107*, 7595.

(3) Bernardi, F.; Traverse, A.; Olivi, L.; Alves, M. C. M.; Morais, J. *Journal of Physical Chemistry C*, *115*, 12243.

(4) Huang, W.; Lobo, R. F.; Chen, J. G. *Journal of Molecular Catalysis A - Chemical* **2008**, *283*, 158.

(5) Rades, T.; Borovkov, V. Y.; Kazansky, V. B.; Polisset-Thfoin, M.; Fraissard, J. *Journal of Physical Chemistry* **1996**, *100*, 16238.

(6) Mazzone, G.; Rivalta, I.; Russo, N.; Sicilia, E. *Journal of Physical Chemistry C* **2008**, *112*, 6073.

(7) Srnova-Sloufova, I.; Lednicky, F.; Gemperle, A.; Gemperlova, J. *Langmuir* **2000**, *16*, 9928.

(8) Lahiri, D.; Chattopadhyay, S.; Bunker, B. A.; Doudna, C. M.; Bertino, M. F.; Blum, F.; Tokuhiro, A.; Terry, J. *Physica Scripta* **2005**, *T115*, 776.

(9) *Introduction to zeolite science and practice*; van Bekkum, H.; Flanigen, E. M.; Jacobs, P. A.; Jansen, J. C., Eds.; Elsevier Science B.V.: Amsterdam, the Netherlands, 2001.

(10) Sheu, L. L.; Knoezinger, H.; Sachtler, W. M. H. *Journal of the American Chemical Society* **1989**, *111*, 8125.

(11) Jiang, Y.; Weng, W.; Si, D.; Sun, S. *Journal of Physical Chemistry B* **2005**, *109*, 7637.

(12) Schaal, M. T.; Pickerel, A. C.; Williams, C. T.; Monnier, J. R. *Journal of Catalysis* **2008**, *254*, 131.

(13) Torigoe, K.; Esumi, K. *Langmuir* **1993**, *9*, 1664.

(14) Nishida, N.; Shiraishi, Y.; Kobayashi, S.; Toshima, N. *Journal of Physical Chemistry C* **2008**, *112*, 20284.

(15) Heinrichs, B.; Noville, F.; Schoebrechts, J. P.; Pirard, J. P. *Journal of Catalysis* **2000**, *192*, 108.

(16) Torigoe, K.; Nakajima, Y.; Esumi, K. *Journal of Physical Chemistry* **1993**, *97*, 8304.

(17) Michaelis, M.; Henglein, A.; Mulvaney, P. *Journal of Physical Chemistry* **1994**, *98*, 6212.

(18) Liz-Marzan, L. M.; Philipse, A. P. *Journal of Physical Chemistry* **1995**, *99*, 15120.

(19) Wu, M. L.; Lai, L. B. *Colloids and Surfaces A: Physicochemical and Engineering Aspects* **2004**, *244*, 149.

(20) Devarajan, S.; Bera, P.; Sampath, S. *Journal of Colloid and Interface Science* **2005**, *290*, 117.

(21) Khan, N. A.; Uhl, A.; Shaikhutdinov, S.; Freund, H. J. *Surface Science* **2006**, *600*, 1849.

(22) Feng, Y. Y.; Zhang, G. R.; Ma, J. H.; Liu, G.; Xu, B. Q. *Physical Chemistry Chemical Physics*, *13*, 3863.

(23) Du, H.; Klemt, R.; Schell, F.; Weitkamp, J.; Roduner, E. *Proceedings of the 12th International Zeolite Conference*; Material Research Society: Warrendale, PA, 1999; 2655.

(24) Grass, M. E.; Yue, Y.; Habas, S. E.; Rioux, R. M.; Teall, C. I.; Yang, P.; Somorjai, G. A. *Journal of Physical Chemistry C* **2008**, *112*, 4797.

(25) Ryoo, R.; Pak, C.; Cho, S. J. *Japanese Journal of Applied Physics Part 1 - Regular Papers Short Notes & Review Papers* **1993**, *32*, 475.

(26) *Catalysis and zeolites: fundamentals and applications*; Weitkamp, J.; Puppe, L., Eds.; Springer-Verlag: Berlin, Germany, 1999.

(27) Breck, D. W. *Zeolite molecular sieves: structure, chemistry, and use*; Robert E. Krieger Publishing Company, Inc.: Malabar, Florida, USA, 1984.

(28) Nagy, J. B.; Bodart, P.; Hannus, I.; Kirisci, I. *Synthesis, characterization and use of zeolitic microporous materials*; DecaGen Ltd.: Szeged, Hungary, 1998.

(29) Baerlocher, C.; McCusker, L. B.; Olson, D. H. *Atlas of zeolite framework types*; Elsevier: Amsterdam, The Netherlands, 2007.

(30) Ryoo, R.; Cho, S. J.; Pak, C.; Lee, J. Y. *Catalysis Letters* **1993**, *20*, 107.

(31) Archipov, T.; Santra, S.; Ene, A. B.; Stoll, H.; Rauhut, G.; Roduner, E. *Journal of Physical Chemistry C* **2009**, *113*, 4107.

(32) Gupta, B. D.; Elias, A. J. *Basic Organometallic Chemistry: Concepts, Syntheses, and Applications of Transition Metals*; CRC Press: Boca Raton, Florida, USA, 2010.

(33) Roduner, E. *Nanoscopic materials: size-dependent phenomena*; The Royal Society of Chemistry: Cambridge, UK, 2006.

(34) Chen, H. M.; Peng, H. C.; Liu, R. S.; Hu, S. F.; Jang, L. Y. *Chemical Physics Letters* **2006**, *420*, 484.

(35) Pal, S.; De, G. *Physical Chemistry Chemical Physics* **2008**, *10*, 4062.

(36) Roduner, E. *Chemical Society Reviews* **2006**, *35*, 583.

(37) Liu, X.; Dilger, H.; Eichel, R. A.; Kunstmann, J.; Roduner, E. *Journal of Physical Chemistry B* **2006**, *110*, 2013.

(38) Massen, C.; Mortimer-Jones, T. V.; Johnston, R. L. *Journal of the Chemical Society - Dalton Transactions* **2002**, 4375.

(39) Cheng, D. J.; Wang, W. C.; Huang, S. P. *Journal of Physical Chemistry C* **2007**, *111*, 8037.

(40) Abbott, H. L.; Aumer, A.; Lei, Y.; Asokan, C.; Meyer, R. J.; Sterrer, M.; Shaikhutdinov, S.; Freund, H. J. *Journal of Physical Chemistry C*, *114*, 17099.

(41) Pervan, P.; Milun, M. *Surface Science* **1992**, *264*, 135.

(42) Rodriguez, J. A.; Kuhn, M. *Journal of Physical Chemistry* **1994**, *98*, 11251.

(43) Choo, H.; Prakash, A. M.; Zhu, Z. D.; Kevan, L. *Journal of Physical Chemistry B* **2000**, *104*, 3608.

(44) Choo, H.; Hong, S. B.; Kevan, L. *Journal of Physical Chemistry B* **2001**, *105*, 7730.

(45) Wang, P.; Yang, S.; Kondo, J. N.; Domen, K.; Baba, T. *Bulletin of the Chemical Society of Japan* **2004**, *77*, 1627.

(46) Günzler, H.; Gremlich, H.-U. *IR spectroscopy: an introduction*; Wiley-VCH Verlag GmbH: Weinheim, Germany, 2002.

(47) Herzberg, G. *Molecular spectra and molecular structure. I. Spectra of diatomic molecules*; D. Van Nostrand Company, Ltd.: Toronto, Canada, 1950.

(48) *Spectroscopy of transition metal ions on surfaces*; Weckhuysen, B. M.; Van der Voort, P.; Catana, G., Eds.; Leuven University Press: Leuven, Belgium, 2000.

(49) Colthup, N. B.; Daly, L. H.; Wiberley, S. E. *Introduction to infrared and Raman spectroscopy*; Academic Press, Inc.: Boston, USA, 1990.

(50) Weil, J. A.; Bolton, J. R. *Electron paramagnetic resonance: elementary theory and practical applications*; John Wiley and Sons, Inc.: Hoboken, New Jersey, USA, 2007.

(51) Brustolon, M.; Giamello, E. *Electron paramagnetic resonance: a practitioner's toolkit*; John Wiley and Sons, Inc.: Hoboken, New Jersey, USA, 2009.

(52) Atherton, N. M. *Principles of electron spin resonance*; Ellis Horwood Limited: Chichester, UK, 1993.

(53) Brunauer, S.; Emmett, P. H.; Teller, E. *Journal of the American Chemical Society* **1938**, *60*, 309.

(54) Jelinek, L.; Kovats, E. S. *Langmuir* **1994**, *10*, 4225.

(55) Schneider, P.; Hudec, P.; Solcova, O. *Microporous and Mesoporous Materials* **2008**, *115*, 491.

(56) Lippens, B. C.; Deboer, J. H. *Journal of Catalysis* **1965**, *4*, 319.

(57) Deboer, J. H.; Lippens, B. C.; Linsen, B. G.; Broekhof.Jc; Vandenhe.A; Osinga, T. J. *Journal of Colloid and Interface Science* **1966**, *21*, 405.

(58) Harkins, W. D.; Jura, G. *Journal of the American Chemical Society* **1944**, *66*, 1366.

(59) Horvath, G.; Kawazoe, K. *Journal of Chemical Engineering of Japan* **1983**, *16*, 470.

(60) Ustinov, E. A.; Do, D. D. *Langmuir* **2002**, *18*, 4637.

(61) Beale, A. M.; Weckhuysen, B. M. *Physical Chemistry Chemical Physics*, *12*, 5562.

(62) Hollas, J. M. *Modern spectroscopy*; John Wiley: Chichester, UK, 1996.

(63) Wende, H. *Extended x-ray absorption fine structure spectroscopy of surfaces and thin films: local structure, dynamic and magnetic properties*; Koester: Berlin, Germany, 1999.

(64) Ahlers, D. *Magnetic EXAFS: an experimental and theoretical investigation*; Shaker: Aachen, Germany, 2000.

(65) Que, L. *Physical methods in bioinorganic chemistry: spectroscopy and magnetism*; University Science Books: Sausalito, California, USA, 2000.

(66) Akdogan, Y.; Vogt, C.; Bauer, M.; Bertagnolli, H.; Giurgiu, L.; Roduner, E. *Physical Chemistry Chemical Physics* **2008**, *10*, 2952.

(67) Sheu, L. L.; Knoezinger, H.; Sachtler, W. M. H. *Catalysis Letters* **1989**, *2*, 129.

(68) Emmett, P. H. *Journal of the American Chemical Society* **1946**, *68*, 1784.

(69) Xia, Q. H.; Su, K. X.; Ma, X. T.; Ge, H. Q.; Zhu, H. B. *Materials Letters* **2005**, *59*, 2110.

(70) Yuan, X.; Zhuo, S. P.; Xing, W.; Cui, H. Y.; Dai, X. D.; Liu, X. M.; Yan, Z. F. *Journal of Colloid and Interface Science* **2007**, *310*, 83.

(71) Terekhina, O.; Roduner, E. *Journal of Physical Chemistry C* **2012**, *116*, 6973.

(72) Hadjiivanov, K.; Knoezinger, H. *Chemical Physics Letters* **1999**, *303*, 513.

(73) Cairon, O.; Loustaunau, A. *Journal of Physical Chemistry C* **2008**, *112*, 18493.

(74) Bordiga, S.; Garrone, E.; Lamberti, C.; Zecchina, A.; Arean, C. O.; Kazansky, V. B.; Kustov, L. M. *Journal of the Chemical Society-Faraday Transactions* **1994**, *90*, 3367.

(75) Lynn, M. A.; Bursten, B. E. *Inorganica Chimica Acta* **1995**, *229*, 437.

(76) Agostini, G.; Usseglio, S.; Groppo, E.; Uddin, M. J.; Prestipino, C.; Bordiga, S.; Zecchina, A.; Solari, P. L.; Lamberti, C. *Chemistry of Materials* **2009**, *21*, 1343.

(77) Hurlburt, P. K.; Rack, J. J.; Luck, J. S.; Dec, S. F.; Webb, J. D.; Anderson, O. P.; Strauss, S. H. *Journal of the American Chemical Society* **1994**, *116*, 10003.

(78) Narayana, N.; Kevan, L. *Journal of Chemical Physics* **1982**, *76*, 3999.

(79) Baker, M. D.; Ozin, G. A.; Godber, J. *Journal of Physical Chemistry* **1985**, *89*, 305.

(80) Sun, T.; Seff, K. *Chemical Reviews* **1994**, *94*, 857.

(81) Bertarione, S.; Scarano, D.; Zecchina, A.; Johanek, V.; Hoffmann, J.; Schauermann, S.; Frank, M. M.; Libuda, J.; Rupprechter, G.; Freund, H. J. *Journal of Physical Chemistry B* **2004**, *108*, 3603.

(82) Grill, C. M.; Gonzalez, R. D. *Journal of Physical Chemistry* **1980**, *84*, 878.

(83) Yudanov, I. V.; Sahnoun, R.; Neyman, K. M.; Rosch, N.; Hoffmann, J.; Schauermann, S.; Johanek, V.; Unterhalt, H.; Rupprechter, G.; Libuda, J.; Freund, H. J. *Journal of Physical Chemistry B* **2003**, *107*, 255.

(84) Vannice, M. A.; Wang, S. Y. *Journal of Physical Chemistry* **1981**, *85*, 2543.

(85) Guerrero-Ruiz, A.; Yang, S. W.; Xin, Q.; Maroto-Valiente, A.; Benito-Gonzalez, M.; Rodriguez-Ramos, I. *Langmuir* **2000**, *16*, 8100.

(86) Gallezot, P. *Catalytic Reviews: Science and Engineering* **1979**, *20*, 121.

(87) Akdogan, Y.; Anantharaman, S.; Liu, X.; Lahiri, G. K.; Bertagnolli, H.; Roduner, E. *Journal of Physical Chemistry C* **2009**, *113*, 2352.

(88) Cheng, D. J.; Wang, W. C.; Huang, S. P. *Physical Chemistry Chemical Physics* **2008**, *10*, 2513.

(89) Zhang, M.; Fournier, R. *Journal of Molecular Structure - Theochem* **2006**, *762*, 49.

(90) Schmauke, T.; Moeller, E.; Roduner, E. *Chemical Communications* **1998**, 2589.

(91) Goldfarb, D.; Bernardo, M.; Strohmaier, K. G.; Vaughan, D. E. W.; Thomann, H. *Journal of the American Chemical Society* **1994**, *116*, 6344.

(92) Baldansuren, A.; Roduner, E. *Chemical Physics Letters* **2009**, *473*, 135.

(93) Morton, J. R.; Preston, K. F. *Journal of Magnetic Resonance* **1986**, *68*, 121.

(94) Kubo, R. *Journal of the Physical Society of Japan* **1962**, *17*, 975.

(95) Michalik, J.; Kevan, L. *Journal of the American Chemical Society* **1986**, *108*, 4247.

(96) Gellens, L. R.; Mortier, W. J.; Schoonheydt, R. A.; Uytterhoeven, J. B. *Journal of Physical Chemistry* **1981**, *85*, 2783.

(97) Baldansuren, A.; Eichel, R. A.; Roduner, E. *Physical Chemistry Chemical Physics* **2009**, *11*, 6664.

(98) Baldansuren, A.; Dilger, H.; Eichel, R.-A.; van Bokhoven, J. A.; Roduner, E. *Journal of Physical Chemistry C* **2009**, *113*, 19623.

(99) Aboukais, A.; Vedrine, J. C.; Naccache, C. *Journal of the Chemical Society-Faraday Transactions 2: Molecular and Chemical Physics* **1978**, *74*, 959.

(100) Brown, D. R.; Kevan, L. *Journal of Physical Chemistry* **1986**, *90*, 1129.

(101) Jacobs, P. A. *Zeolite chemistry and catalysis: proceedings of an international symposium, Prague, Czechoslovakia, September 8-13, 1991*; Elsevier: Amsterdam, the Netherlands, 1991.

(102) Dyrek, K.; Che, M. *Chemical Reviews* **1997**, *97*, 305.

(103) Kellerman, R.; Texter, J. *Journal of Chemical Physics* **1979**, *70*, 1562.

(104) Beyer, H.; Jacobs, P. A.; Uytterhoeven, J. B. *Journal of the Chemical Society-Faraday Transactions I* **1976**, *72*, 674.

(105) Narayana, M.; Michalik, J.; Contarini, S.; Kevan, L. *Journal of Physical Chemistry* **1985**, *89*, 3895.

(106) Prakash, A. M.; Wasowicz, T.; Kevan, L. *Journal of Physical Chemistry B* **1997**, *101*, 1985.

(107) Michalik, J.; Heming, M.; Kevan, L. *Journal of Physical Chemistry* **1986**, *90*, 2132.

(108) Stokes, L. S.; Murphy, D. M.; Farley, R. D.; Rowlands, C. C.; Bailey, S. *Physical Chemistry Chemical Physics* **1999**, *1*, 621.

(109) Kucherov, A. V.; Shelef, M. *Catalysis Letters* **2001**, *75*, 19.

(110) Mojet, B. L.; Miller, J. T.; Koningsberger, D. C. *Journal of Physical Chemistry B* **1999**, *103*, 2724.

(111) Kustov, L. M.; Ostgard, D.; Sachtler, W. M. H. *Catalysis Letters* **1991**, *9*, 121.

(112) Stakheev, A. Y.; Shpiro, E. S.; Jaeger, N. I.; Schulz Ekloff, G. *Catalysis Letters* **1995**, *34*, 293.

(113) Martins, R. L.; Baldanza, M. A. S.; Schmal, M. *Journal of Physical Chemistry B* **2001**, *105*, 10303.

(114) Dejong, K. P.; Meima, G. R.; Geus, J. W. *Applied Surface Science* **1982**, *14*, 73.

(115) Rodriguez, J. A.; Truong, C. M.; Goodman, D. W. *Surface Science* **1992**, *271*, L331.

(116) Lima, F. H. B.; Sanches, C. D.; Ticianelli, E. A. *Journal of the Electrochemical Society* **2005**, *152*, A1466.

(117) Schmauke, T.; Eichel, R.-A.; Schweiger, A.; Roduner, E. *Physical Chemistry Chemical Physics* **2003**, *5*, 3076.

(118) Chen, F.; Curley, B. C.; Rossi, G.; Johnston, R. L. *Journal of Physical Chemistry C* **2007**, *111*, 9157.

(119) Christen, H. R. *Grundlagen der allgemeinen und anorganischen Chemie*; Verlag Sauerlaender: Aarau, Switzerland, 1969.

(120) Dickerson, R. E.; Gray, H. B.; Darensbourg, M. Y.; Darensbourg, D. J. *Chemical Principles*; The Benjamin/Cummings Publishing Company, Inc.: Menlo Park, California, USA, 1984.

(121) James, A. M.; Lord, M. P. *Macmillan's Chemical and Physical Data*; Macmillan: London, UK, 1992.

(122) *Standard Potentials in Aqueous Solutions*; Bard, A. J.; Parsons, R.; Jordan, J., Eds.; IUPAC (Marcel Dekker): New York, USA, 1985.